UNIVERSITY OF CALIFORNIA,
IRVINE

Experimental and Theoretical Investigation of the Emission and Diffraction of Discrete Tone Noise Generated from the Exhaust of a Ducted Fan

DISSERTATION

submitted in partial satisfaction of the requirements
for the degree of

DOCTOR OF PHILOSOPHY

in Mechanical and Aerospace Engineering

by

Alexander Truong

Dissertation Committee:
Professor Dimitri Papamoschou, Chair
Professor Feng Liu
Professor Haithem Taha

2018

DEDICATION

To Newton's third law.
You have to leave something behind
to go forward.

TABLE OF CONTENTS

LIST OF FIGURES

LIST OF TABLES

NOMENCLATURE

Abbreviations

ANOPP	Aircraft Noise Prediction Program
BEC	Battery Eliminator Circuit
BEM	Boundary Element Method
BPF	Blade Passage Frequency
BWB	Blended Wing Body
CAD	Computer-Aided Design
CFD	Computational Fluid Dynamics
DC	Direct Current
FPR	Fan Pressure Ratio
EPNL	Effective Perceived Noise Level
ESC	Electronic Speed Control
FAA	Federal Aviation Administration
FAR	Federal Aviation Regulation
FFT	Fast Fourier Transform
FW-H	Ffowcs-Williams and Hawking
GRC	Glenn Research Center
LiPo	Lithium-ion Polymer Battery
NASA	National Aeronautics and Space Administration
OASPL	Overall Sound Pressure Level
PWM	Pulse Width Modulation
RANS	Reynolds Average Navier-Stokes
RC	Radio Control
RPM	Revolution Per Minute
SDT	Source Diagnostic Test
SLA	Sterolithography Apparatus
SNA	John Wayne Airport, Orange County
SPL	Sound Pressure Level
UCI	University of California, Irvine
VK	Vold-Kalman

Roman Symbols

a	Speed of sound
A	Structural equation matrix
A_k	Wavepacket parameter vector
b	Asymmetric Gaussian width
B	Blade count
c	Chord length of wing
c_{group}	Group velocity: speed at which envelope propagate through space
C	Flow velocity in the absolute frame of reference

C_k	Complex phasor matrix
C_u	Absolute tangential velocity
C_z	Axial component of velocity
dB	Decibel
D_0	Nozzle exit diameter
f	Frequency
$f(t)$	Instantaneous frequency
$\mathscr{F}$	Fourier Transform
G	3D free-space Green's function
h	Harmonic number
$H_m^{(1)}(z)$	Hankel function of the first kind of order m, $H_m^{(1)}(z) = J_m(z) + iY_m(z)$
$H_m^{(2)}(z)$	Hankel function of the second kind of order m, $H_m^{(2)}(z) = J_m(z) - iY_m(z)$
Hz	Hertz
i	imaginary unit $= \sqrt{-1}$
I	Identity matrix
$J(x)$	Cost function
$J_m(z)$	Bessel Function of the first kind of order m
k	Wavenumber or integer in Tyler-Sofrin Rule
k_0	Acoustic wavenumber, $k_0 = \omega/a_\infty$
k_r	Radial wavenumber
k_z	Axial wavenumber
M	Mach number
m	Azimuthal mode number
$\dot{m}$	Mass flow rate
p	Acoustic pressure
P	Spatial Fourier transform of acoustic pressure
$\mathscr{P}$	Frequency/Wavenumber Fourier Transform of Pressure
$p_0(z)$	Wavepacket envelope
P_0	Total pressure
r	Weighting factor in VK filter or radial position
r_0	Radius of cylindrical surface on which wavepacket is prescribed on
S	Wingspan
t	Time
t/c	Airfoil thickness to chord ratio in percent
T_0	Total temperature
U	Velocity
V	Vane count
v_p	Phase velocity: rate at which the phase of the wave propagates in space
W	Flow velocity in the relative frame of reference
$W(z)$	Faddeva function
W_u	Relative tangential velocity
x, y, z	Cartesian coordinate system position
$x_k(t)$	Time-varying (complex) envelope of order k
$y(t)$	Total measured acoustic signal
$Y_m(z)$	Bessel Function of the second kind of order m
z_0	Peak noise location of wavepacket relative to nozzle exit

Greek Symbols

α	Flow angle in the *absolute* frame of reference as measured from the axial direction
β	Flow angle in the *relative* frame of reference as measured from the axial direction
δ	Delta function
$\Delta\varphi$	Angle between stator blades
Δt	Time for rotor blade to rotate between stator blades
$\varepsilon(t)$	Error in structural equation fit
$\eta(t)$	Broadband or shaft-uncorrelated noise
$\eta(z)$	Radial displacement of the vortex sheet
θ	Polar angle relative to downstream axis (degrees)
λ	Wavelength
μ_{mn}	Separation eigenvalue constant for m harmonic and n^{th} zero crossing
π	Mathematical constant, $\pi = 3.14159..$
ρ	Density
ϕ	Velocity potential
φ	Azimuthal angle
ω_0	Angular acoustic frequency
Ω	Shaft angular frequency (rad/s)
$\nabla^p x_k[n]$	Structural equation of order p
∇^2	Laplace operator
()	Round brackets denote continuous signals
[]	Square brackets denote discrete signals

Subscripts and Superscripts

$exit$	exit of nozzle
exp	experiment
far	far-field
H	Hermitian
i	incident
k	harmonic or order of signal
max	maximum value
$model$	modeled
m	reference microphone number for cross-spectra or azimuthal mode number
$stator$	stator
T	Transpose
TE	Trailing edge
z	Axial
∞	Ambient or freestream

CURRICULUM VITAE

Alexander Truong

2018 Ph.D, Mechanical and Aerospace Engineering
University of California, Irvine

2012 Master of Science in Mechanical and Aerospace Engineering
University of California, Irvine

2010 Bachelor of Science in Aerospace Engineering
University of California, Irvine

Publications

Truong, A., and Papamoschou, D.,"Harmonic and Broadband Separation of Noise from a Small Ducted Fan," AIAA paper 2015-3282, 21st Aeroacoustics Conference, 22-26 June 2015, Dallas, Texas.

Truong, A., and Papamoschou, D., "Experimental Simulation of Ducted Fan Acoustics at Very Small Scale," AIAA paper 2014-0718, 52nd Aerospace Sciences Meeting, 13-17 January 2014, National Harbor, Maryland.

Truong, A., and Papamoschou, D., "Aeroacoustic Testing of Open Rotors at Very Small Scale, " AIAA paper 2013-0217, 51st Aerospace Sciences Meeting, 07-10 January 2013, Ft. Worth, Texas.

ABSTRACT OF THE DISSERTATION

Experimental and Theoretical Investigation of the Emission and Diffraction of Discrete Tone Noise Generated from the Exhaust of a Ducted Fan

By

Alexander Truong

Doctor of Philosophy in Mechanical and Aerospace Engineering

University of California, Irvine, 2018

Professor Dimitri Papamoschou, Chair

In modern turbofan engines powering commercial aircraft, the fan is becoming the dominant source of noise at takeoff and landing. Understanding and modeling of the fan noise source, and the interaction of the emitted sound with the airframe, are critical for the design of quiet aircraft. Of particular importance is discrete tone noise radiating from the fan exhaust whose propagation can be shielded by the airframe in advanced aircraft configurations. Current prediction methods for fan noise and its propagation require tremendous amount of computational resources and time. Experiments in large-scale facilities are extremely expensive. There is a need for efficient approaches to experimentally investigate and model fan noise, thus enabling parametric studies that can identify optimal configurations. This study combines novel small-scale experiments with low-order, physics-based modeling of the fan noise source towards achieving the aforementioned goal.

The experimental effort entailed the design and construction of a subscale ducted fan rig that includes all the relevant components of the turbofan engine and simulates accurately the sound emission generated by the fan of such engines. The ducted fan includes a nacelle, rotor, and stators, all fabricated using advanced stereolithographic or metal casting methods. It is powered by a high-performance DC motor and achieves rotor tip Mach number of around 0.61 and fan pressure ratio of 1.157, values compatible with the operation of high-bypass tur-

bofan engines. Acoustic diagnostic was conducted inside an anechoic chamber using far-field and near-field phased arrays consisting of 23 microphones. Installation of a rectangular flat plate representing the airframe below the ducted fan recreates complex phenomenon such as scattering off the obstacle, and diffraction around the shield. Addition of the rectangular plate shield generated complex trends in the tonal content and demonstrates the large potential to reduce noise through shielding by the airframe. Tones below the shielding surface were well attenuated, while tones emitted in the aft direction were unchanged. Acquired acoustic data were used to formulate the wavepacket noise model and shielding simulations.

The theoretical effort comprises the following steps: (a) extraction of the harmonic content of the measured noise through use of the Vold-Kalman filter; (b) modeling of the aft-emitted fan noise source as a cylindrical wavepacket with azimuthal modes inferred from the Tyler-Sofrin theory; (c) determination of wavepacket shape parameters through least-squares matching of the measured cross-spectral density in the near field and the far field at a given frequency; and (d) propagation and diffraction of the sound from the modeled source using the Boundary Element Method (BEM), with comparisons to measured data.

Far-field source parameterization shows that the wavepacket can be modeled as a short cylindrical disturbance surrounding the exit of the nozzle. The resulting modeled sound field captures the most prominent experimental far-field and near-field magnitude and phase relations across numerous microphones. Near-field parameterization expressed similar values to the far-field parameter optimization. This consistency of the cross-spectra in the near and far-field justifies the wavepacket's applicability as an equivalent discrete tone noise source for sound generated by the exhaust of a ducted fan. Numerical shielding predictions using Boundary Element Method (BEM) exhibit complicated changes in far-field noise radiation. Reasonable agreement in average noise reductions is found with experimental data.

Chapter 1

Background and Motivation

It has been over 50 years since the Boeing 707 ushered in both the jet age and the era of federal mandates requiring minimum noise standards for aircraft entering service. Takeoff and landing noise in the immediate vicinity of an airport is regulated, cruise is not. Lack of visible noise abatement technology has been a recognized barrier to unhindered airport operations. Airports such as John Wayne in Orange County, California (SNA) enforce some of the most stringent noise regulations in the United States. Orginally founded as a rural flight school, the orginal landing strip once surronded by celery fields is now surronded by permanent noise monitoring stations dispersed amidst suburbia, as portrayed in Fig. 1.1. For every decibel over the noise limit, approximately twenty passengers must be offloaded to get inside the limit [8]. Aircraft incapable of meeting noise limitations are not permitted to land, take-off, or be based at the airport. Such trade-offs and financial liabilities have motivated considerable research effort in the past to suppress jet noise and understand the physical process of sound generation of the jet [9]. However, jet noise is no longer the dominant noise source in modern turbofan powered commercial aircraft [10]. With every new set of regulations, the airline industry requires upgrades to its jet aircraft, if not new designs. The combined reality of continued growth in air traffic, increasingly more stringent environmental goals, and the supplementary limitations imposed by airports- such as curfews, still results in continued strong demand for aircraft noise reduction technology.

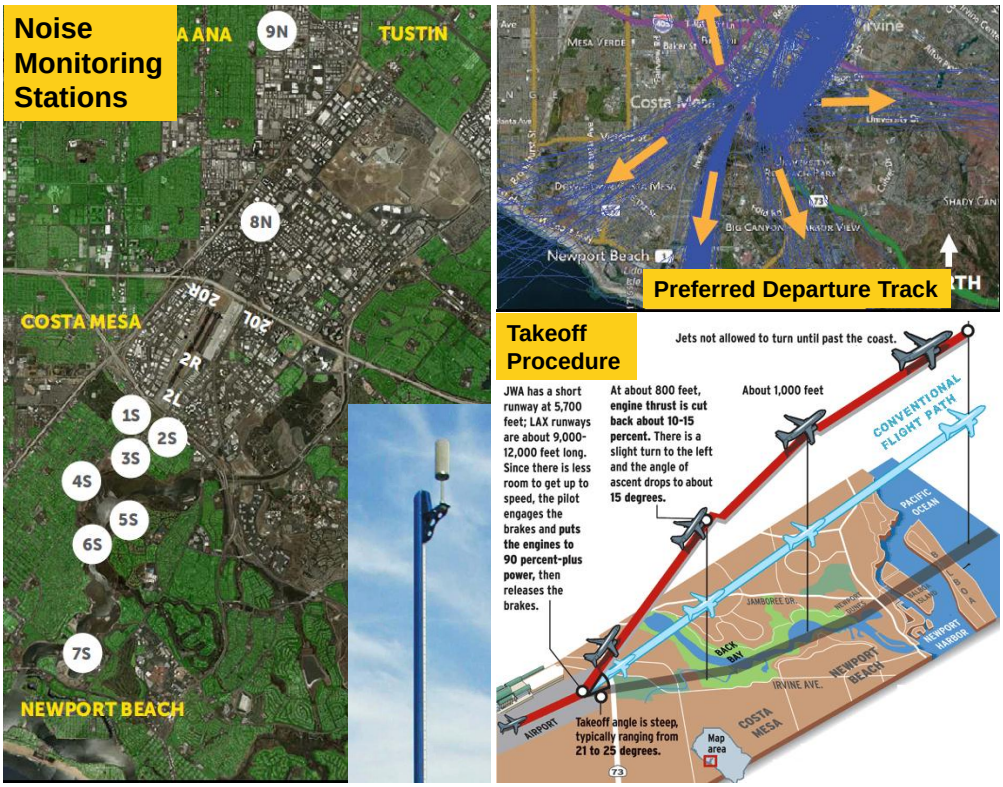

Figure 1.1: Noise measurement locations for John Wayne Airport. Notice that microphone locations are heavily concentrated in the city of Newport Beach. Image from SNA Access & Noise Office.

Attainment of the noise goals requires not only improvements at the component level, but also a systems integration approach for the design of the propulsor and the airframe. The blended wing body (BWB) airplane concept has been central to these efforts because its layout is amenable to innovative integration concepts and its aerodynamic efficiency is superior to that of conventional airplane designs [11]. Effective shielding of the fan noise requires knowledge of the source characteristics. This impacts the entire aircraft design because decisions such as the placement of the engines, geometry of the elevon, and positioning of the vertical fins are driven not only by aerodynamics-but also acoustic considerations. The latest flight tested subscale blended wing body aircraft illustrated in Fig. 1.2, the X-48C, reflects recent research in shielding of jet [12, 13] noise by the airframe. Alterations to the initial design, so called the "low noise" configuration, includes extension of the aft deck, and relocation of the winglets inboard to optimize jet noise shielding.

Figure 1.2: The X-48C Hybrid Wing Body research aircraft banks right over NASA's Dryden Flight Research Center at Edwards Air Force Base during one of the sub-scale aircraft's final test flights on Feb. 28, 2013. Credits: NASA Carla Thomas.

A Blended Wing body aircraft with an open rotors [14, 15] or geared turbofans represents prospective propulsion options. Of particular importance is aft-emitted tonal noise whose propagation can be shielded by the airframe in advanced aircraft configurations. Acoustic shielding predictions for realistic problems are challenging due to the existence of a wide range of length and frequency scales which requires tremendous computational resources. There is need for efficient approaches to experimentally investigate and model fan noise, thus enabling parametric studies that can identify optimal configurations.

This study combines novel experiments with low-order, physics-based modeling of the fan noise source towards achieving the aforementioned goal. Here we use a deterministic tonal noise source model based on the wavepacket ansatz. Previous studies have applied this framework successfully to jet noise [16–18]. Re-framing this schema for fan noise provides a deterministic model that captures the salient physics of the source, and enables predictions of the radiated sound and its scattering around objects without inordinate computational resources. Its formulation exploits the behavior of the acoustic solution inside the duct of a turbofan. This sound is forced to propagate along the duct until it reaches the end, the fan nozzle, at which point it is free to radiate into the surrounding. When viewed

from the outside the nacelle, the footprint of these modal structures is approximated as a amplitude modulated traveling wave on a imaginary control surface surrounding the exit of the nozzle. The fan noise source model shape are described by parameters and azimuthal modes inferred from Tyler and Sofrin's rule [19, 20]. The superposition of wavepackets at various BPF frequencies will reproduce the far-field sound intensity distribution.

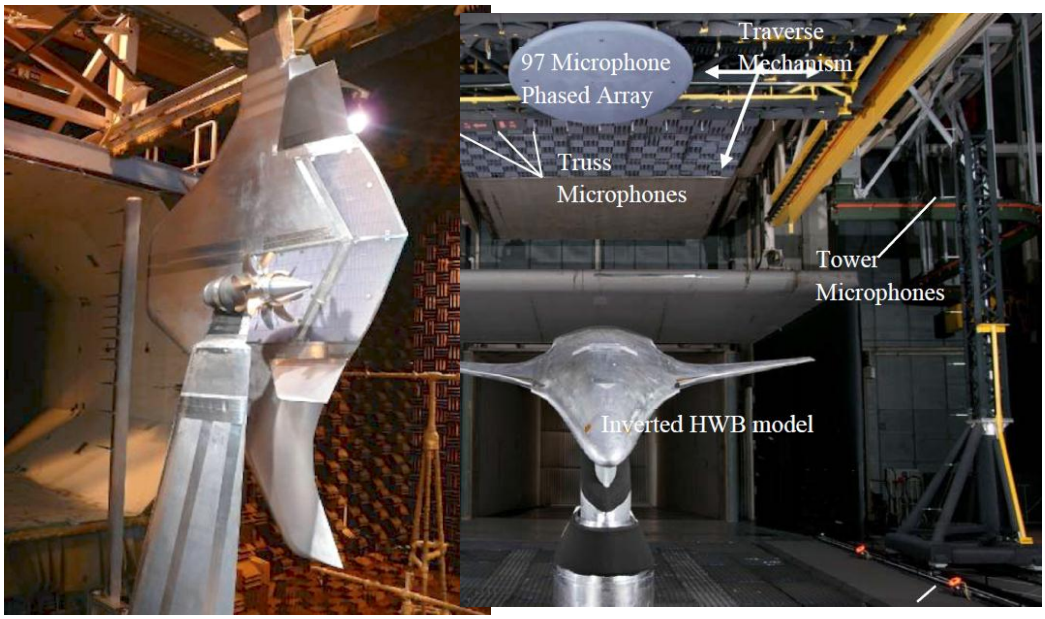

Figure 1.3: Boeing Low Speed Aeroacoustics Facility configured for Hybrid Wind Body installation effects testing from Boeing (left). NASA Langley HWB test section configuration from NASA George Holmich.

Optimization of the wavepacket parameters are determined through matching of the measured cross-spectral density obtained from near and far-field microphone arrays. These highly sophisticated microphone arrays such as those depicted in Fig 1.3, have proven to be invaluable diagnostic tools to pinpoint the dominant noise producing components. In particular, NASA Glenn Research Center (GRC) has conducted numerous large scale experimental investigations, such as the fan source diagnostic test (SDT) [21–28]. These experiments are obviously very expensive. The small scale paradigm enables significant cost and time savings in the acoustic evaluation of noise-reducing concepts. Additive manufacturing enables the three-dimensional "printing" or metal casting of the complex geometry of fan blades,

and the nacelle structure that are nearly impossible to fabricate using conventional machining. The rapid-prototyping approach has been used successfully with jet noise testing of realistic nozzle configurations and open-rotor spinning at full-scale tip speed powered by high-performance DC motors [12, 15]. More recently, assessments of the relevance of UCI's small scale ducted fan indicate that small-scale models reproduce with good fidelity the main acoustic features [29] . This simulator generates tonal, broadband, and jet noise components simultaneously.

Noise assessment requires the determination of the tonal and broadband components to properly assess the efficacy of noise mitigation strategies and for validating prediction codes. Fan harmonic components occurs at integer multiples of the fundamental frequency (the so-called orders), i.e., engine rotational speed. On the other hand, broadband noise is random in nature and is generated from an array of source mechanisms such as turbulence interaction noise, rotor-stator interaction noise, and trailing edge noise [8]. Each noise component, tonal or broadband, can have different directivity. The level of shielding will depend not only on the source location, but also the directivity and radiation patterns. Thus, knowledge of the tonal and broadband noise content is essential for predicting and optimizing propulsion-airframe integration. Even when tones strongly protrude from the background, the decomposition of the tonal and broadband noise components establishes the importance of broadband noise [30].

Since propulsion noise sources have different characteristics, thus different acoustic propagation effects, the data must be decomposed into its tonal and broadband components. Tonal isolation techniques include the peak-finding algorithm, moving medium curve, phase averaging, and Sree's Method [14,30–32]. However, frequency domain methods cannot easily localize information in the time domain, nor compensate for fluctuations intrinsic to real world experiments. A recent NASA SDT investigation employed a Vold-Kalman (VK) signal processing technique to filter out the harmonic noise sources [6,33]. This tool performs a time-domain decomposition of a measured signal into phase-accurate time history of fan harmonic

and broadband constituents. The output from the filter has a much higher resolution and dynamic range than a Fast Fourier Transform (FFT) or phase averaging procedure. In a similar fashion, this study applies the Vold-Kalman order tracking to acoustics measurements of a small ducted fan.

The experimental effort entailed the design and construction of a small-scaled ducted fan rig that includes all the relevant components of the turbofan engine and simulates accurately the sound emission generated by the fan of such engines. The ducted fan includes a nacelle, rotor, and stators, all fabricated using advanced stereolithographic methods. It is powered by a high performance brushless motor and achieves rotor tip Mach number of around 0.61 and fan pressure ratio of 1.157, values comparable with operation of high-bypass turbofan engines. This one-of-a-kind experimental rig produces radiation patterns comparable with those measured in large-scale NASA experiments at similar conditions. Installation of a surface representing the airframe enables experimental studies on the diffraction of the sound generated by a ducted fan.

The theoretical effort comprises the following steps: (a) extraction of the harmonic content of the measured noise through use of the Vold-Kalman filter; (b) modeling of the aft-emitted fan noise source as a cylindrical wavepacket with azimuthal modes inferred from the Tyler-Sofrin theory; (c) determination of wavepacket shape parameters through least-squares matching of the measured cross-spectral density in the near and far field at a given frequency; and (d) propagation and diffraction of the sound from the modeled source using the Boundary Element Method (BEM), with comparisons to measured data. The intent is to develop predictive methodologies that will be integrated in the next generation Aircraft Noise Prediction Program (ANOPP) tool to provide better prediction of future aircraft technology. Thus, we aim to provide the capability and framework to integrate acoustic approaches for aircraft noise component prediction, and quantifying propulsion system installation effects. This new framework provides more general methods for the effects related to propulsion airframe aeroacoustic interaction, and allows for low-noise optimization of the BWB aircraft

with geared turbofans. In addition, such improvements strengthen insight and understanding into controlling noise physics.

1.1 Objectives

The major goals of the study are:

- Development of small-scale ducted fan with realistic noise emission pattern.
- Acoustic far-field and near-field phased array investigation of the sound generated from the exhaust of a ducted fan.
- Extraction of tonal and broadband components from a small-scale simulator that captures the physics of fan noise generation using a Vold-Kalman filter.
- Development of a novel exhaust fan noise source model based on the wavepacket ansatz that captures the salient physics of the source and reproduces faithfully the acoustic field.
- Source parameterization and application of minimization methods to match the cross-spectral density of the near and far-field sound at a given BPF frequency.
- Computation of the scattered acoustic field from the wavepacket noise source model using boundary element method (BEM).

1.2 Thesis Overview

- **Chapter 1** : Discusses the historical background and the objective of the research.
- **Chapter 2**: Literature review of the concepts and equations vital to the study of ducted fan noise.

- **Chapter 3:** Wavepacket noise source model, wavepacket shape reconstruction from experimental data, and numerical scattering predictions.
- **Chapter 4:** Details the facilities used in the experiments and signal processing techniques.
- **Chapter 5:** Presents and discusses the acoustic results.
- **Chapter 6:** Conclusion and future work.

Chapter 2

Discrete Turbomachinery Noise Sources

This section introduces the concepts and equations that are central to the study of discrete turbofan noise. The aim is to understand the characteristics and mechanisms of aft-emitted tonal sound from a turbofan engine to effectively formulate the noise source representation. To begin, fan noise is caused by periodic motion of the rotor blades. In high bypass ratio turbofans, the fan is enclosed within a duct system which contain stators. This duct confines the propagation of noise downstream until it is radiated from the exhaust of the ducted fan. Thus, the acoustic system consist of the fan noise source, the duct, the stators, and the exterior of the engine to which the acoustic field is radiated. It is intuitive to isolate these constituents. Specifically, the development of concepts is broken down into four distinct segments. First, the characteristics and mechanism of rotor noise are described, and then extended to duct transmission. Next, we tackle rotor-stator interaction. Lastly, the emission from the exhaust of the ducted fan is reviewed. This chapter is based on the synthesis of literature from Magliozzi and Smith and many others [1, 8, 20, 34–36]. It is assumed no coupling between other source term exists. This simplification allows the source contribution of each element to be considered independently and is foundation to many fan noise models [1, 37]. That is, the coupling between the rotor and stators is only acoustical.

These findings enable the development of a physics-based noise source model. Knowledge of the mode pattern and propagating characteristics will help configure a accurate noise source model. A road-map of this literature review is shown schematically in Fig 2.1.

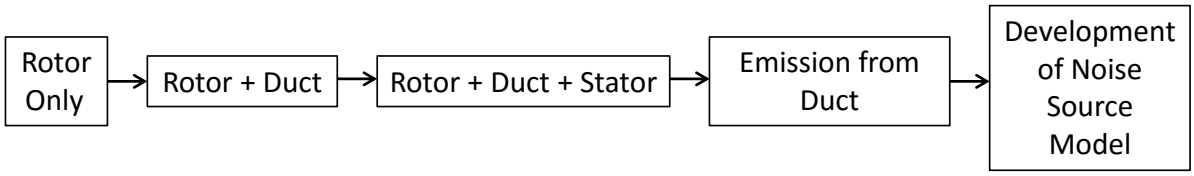

Figure 2.1: Organization of literature review chapter.

2.1 Generation and Transmission of Acoustic Duct Modes

Harmonic noise is caused by sources that are periodic. In other words, harmonic noise is produced by sources that repeat themselves exactly during each revolution of the rotor. Each time a rotor blade passes a stationary point it generates pressure disturbances which propagate into the far-field as sound. For instance, given a propeller with B blades rotating at an angular frequency of Ω radians per second, the rotor will produce a sound occurring at a frequency of $B\Omega$. This frequency is known as the blade passage frequency (BPF), an alternative name is the fundamental frequency. The BPF is the rate at which the blades of the rotor pass when viewed from a fixed location. One may think the BPF as being analogous to the rate of a flashing LED, where each blink corresponds to the passage of the blade. However, a propeller blade does not just generate sound at the BPF, other frequencies are present that occur at integer multiples of the BPF, i.e $1\times$ BPF, $2\times$ BPF, $3\times$ BPF, etc.

Harmonic noise arises from the thickness, and steady loading of the rotor blade. Thickness noise is generated due to the thickness of the blade. As the blade moves, the motion of the blade displaces a given volume of air that is equal to the volume of the blade. An observer standing on the blade sees the volume displacement of air as steady. However, when viewed from a fixed frame, this volume displacement is seen as time-varying, giving rise to a time-varying pressure that propagates as noise. Intuitively, a larger volume blade section

generates more thickness noise. Hence, one should use a thinner section to reduce thickness noise.

Steady loading noise is the sound that is created by the steady aerodynamic forces acting on the blade surfaces. In the case of steady loading, the lift and drag on the blade are constant when the observer is attached to the moving blade. Transformation to a fixed reference frame, gives a different perspective where the observer sees the direction of the aerodynamic force vector change in time. This phenomenon gives rise to a time-varying pressure field that propagates as sound.

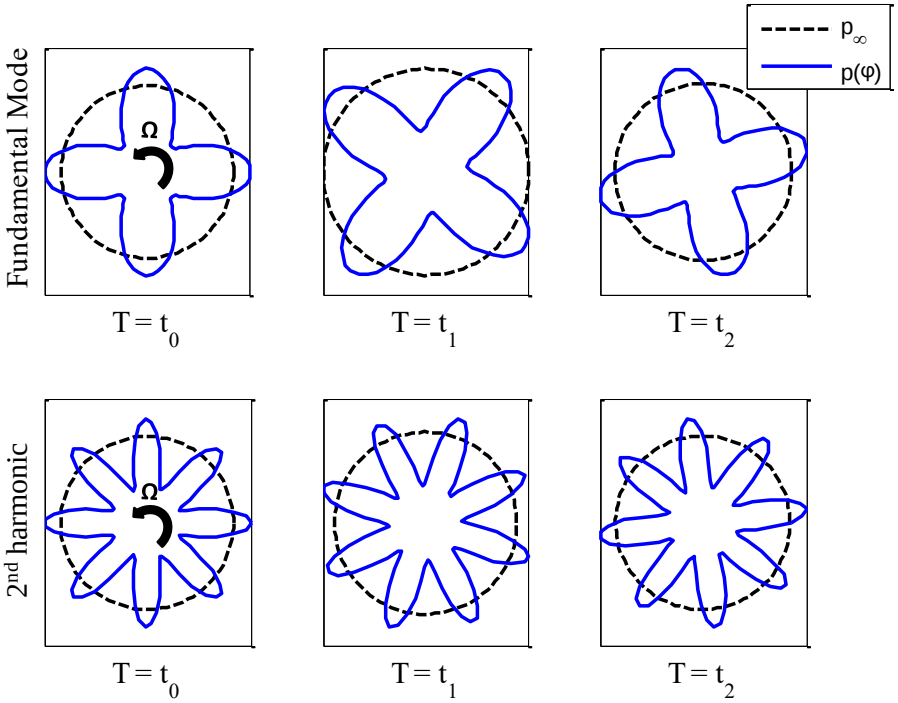

Figure 2.2: Display of pressure field components and phase relationship at a fixed instant of time.

Let's consider the pressure field associated with steady aerodynamic and thickness effects for a 4 bladed fan. The blades act as airfoils with high pressure on one side and low pressure on the other. Observing the pressure field on the back of the rotor (i.e. pressure side), the pressure is maximum near the blades and troughs in between. Because the blades are spaced 90 degrees apart, the pressure distribution must be separated out with the same

angular division, as illustrated in the upper left image of Fig 2.2 [38]. As time advances, the pressure distribution spins with the angular velocity of the fan, Ω with respect to a fixed observer on the ground. The form of the pressure field, $p(\varphi, t)$ is a spinning wave with 4 lobe pattern rotating at the shaft speed. The spinning pressure patterns generated by the rotating fan blades are called acoustic modes. The total rotor pressure field consists of a superposition of lobed patterns all turning with the shaft speed. These pressure pattern are like spokes on a wheel. The fundamental is associated with a 4 lobe pattern, while the second harmonic have patterns twice this number of lobes as depicted in the lower panel of Fig 2.2. The fluctuating pressure field is defined by its circumferential order m, and represented as a Fourier series specified at some reference plane near the rotor by [39]:

$$p(r, \varphi, t) = \sum_{m=-\infty}^{\infty} F_m(r) \exp\Big[i(mB\Omega t - mB\varphi)\Big] \tag{2.1}$$

Where the $F(r)$ represents the radial distribution, B is the number of blades, and m is the harmonic.

When the fan is enclosed in a duct, the pressure perturbations must propagate through the channel before emanating to an observer outside the duct. The dynamics of the propagation are governed by the Naiver-Stokes equations, or the Euler equations- if viscosity can be neglected. For small disturbances, the governing dynamics are linearized [40]. Reduction to the canonical wave equation is possible when the flow is uniform (exact) or a potential (low-Mach number approximation). For a uniform axial flow ($\vec{U} = U\hat{z} + 0\hat{e_r} + 0\hat{e_\varphi}$) the pressure field satisfies the convective wave equation:

$$\frac{1}{a_\infty^2}(\frac{\partial}{\partial t} + U\frac{\partial}{\partial z})^2 p = \nabla^2 p \quad \xrightarrow{Expand} \quad \frac{1}{a_\infty^2}(\frac{\partial^2 p}{\partial t^2} + 2U\frac{\partial p}{\partial t \partial z} + U^2\frac{\partial^2 p}{\partial z^2}) = \nabla^2 p \tag{2.2}$$

where p is the acoustic pressure, and ∇^2 is the three-dimensional Laplace operator. A pressure is prescribed on a reference plane normal to the axial axis in the form of a spinning lobed pattern [20]. This condition is represented in blue at $z = 0$ in Fig 2.3. A solid hard

wall surrounds the acoustic domain. This implies the radial velocity is zero on the cylinder or the Neumann boundary condition.

$$\frac{\partial p}{\partial r} = 0 \qquad at \qquad r = r_0 \tag{2.3}$$

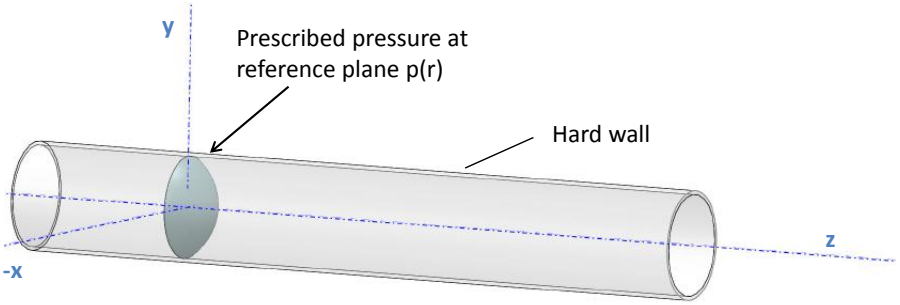

Figure 2.3: Input pressure distribution and boundary condition of the 3-dimensional wave guide problem.

The geometry is axis-symmetric with linear homogeneous boundary conditions- one can readily use separation of variables to solve this partial differential equation. The solution consists of a infinite linear combination of orthogonal basis functions, i.e. modes [41]. For a harmonic field where the time dependence is sinusoidal, the pressure perturbation is expressed as, $p(z, r, \varphi, t) = R(r)e^{im\varphi + ik_z z - iwt}$, and the convective wave equation simplifies to

$$-\underbrace{\left(\frac{\omega^2}{a_\infty^2} + 2Mk_z\frac{\omega}{a_\infty} + (M^2-1)k_z^2\right)}_{\mu^2} = \frac{R''}{R} + \frac{1}{r}\frac{R'}{R} - \frac{1}{r^2}m^2 \tag{2.4}$$

The left side of the equation depends only on the angular frequency, ω, and the right side only on radius, R. As ω and R are independent of each other, each side must be a fixed constant μ. If we divide each side of this equation by r^2R, the radial equation reduces to the Bessel equation:

$$r^2\frac{d^2R}{dr^2} + r\frac{dR}{dr} + (\mu^2 r^2 - m^2)R = 0 \tag{2.5}$$

This well known ODE has a general solution consisting of two linearly independent functions, $J_m(\mu_{mn}r), Y_m(\mu_{mn}r)$. Using the boundness condition $|R(0)| < \infty$, eliminates $Y_m(r)$. In addition, in order for $R(r)$ to be zero on the boundary of the pipe (no-slip), we must pick the separation constant μ to be one of the roots of $J'_m(\mu r_0) = 0$. That is, the radial wave number, $k_{r,mn}$ are the position of the n^{th} zero crossing of the derivative of the Bessel function of the first kind ($d/dzJ_m(z)$) of order m.

$$\mu_{mn} = \frac{k_{r,mn}}{r_0} \tag{2.6}$$

These roots are obtained numerically or from tables. Recalling the expression for the separation constant, μ and denoting the acoustic wave number as $k_0 = \omega/a_\infty$, the axial wavenumber, $k_{z,mn}$ of the (m, n) acoustic mode is given by [42]

$$k^{\pm}_{z,mn} = \frac{Mk_0 \pm \sqrt{k_0^2 - \mu_{mn}^2(1-M^2)}}{1-M^2} = \frac{k_0}{1-M^2}\left[M \pm \sqrt{1 - \frac{\mu_{mn}^2(1-M^2)}{k_0^2}}\right] \tag{2.7}$$

The above equation gives the axial wavenumber k_z in terms of the acoustic wavenumber k_0. This expression is called the dispersion relation. Note that the dispersion equation is not linear, i.e k_z depends on the square of the acoustic wavenumber k_0 and the combined radial-circumferential wave number μ_{mn}. Waves with different frequencies have different phase speeds and as a result the waves disperse as they propagate through the waveguide.

We have just solved the eigenvalue problem. The solution is the product of each spatial component in the r, φ, and z directions. The solution for the acoustic field is:

$$p(z, r, \varphi, \omega) = \sum_{m=-\infty}^{\infty}\sum_{n=1}^{\infty} A^{\pm}_{mn} J_m(k_{r,mn}\frac{r}{r_0}) \exp(i[m\varphi + k^{\pm}_{z,mn}z - \omega t]) \tag{2.8}$$

Three key findings can be inferred from the above expression. Firstly, the acoustic

pressure consist of a counter-clockwise and clockwise spiral motions which depend on Mach number. When the exponential is set to a constant, i.e. $m\varphi - k^{\pm}_{z,mn}z =$ constant, this grouping embodies a isosurface of constant phase, say a crest or troughs- that travel at the phase velocity and forms a helical pattern as shown in Fig. 2.4. The energy of the waves component does not propagate at the axial phase velocity (velocity of wave crest), but at the axial group velocity (signal velocity) defined as $c_{group} = d\omega/dk$ [42].

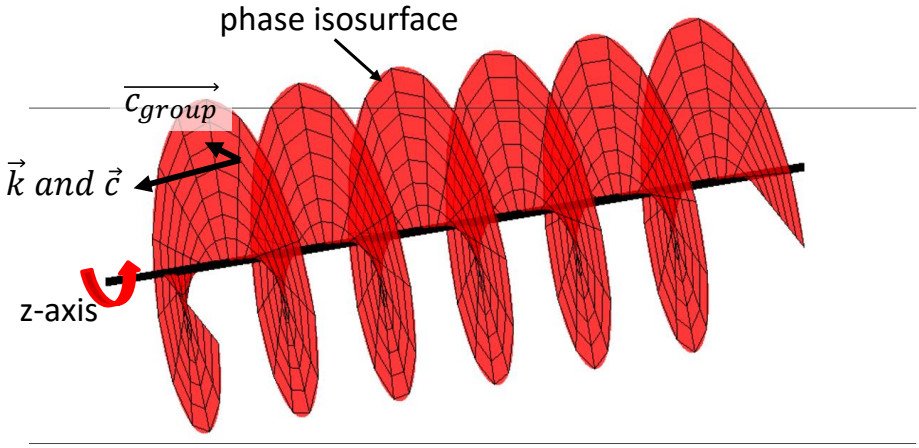

Figure 2.4: Surface of constant phase for acoustic transmission through a cylindrical duct with harmonic forcing.

Pictorially, the group velocity is along the surface of constant phase. Accordingly, the axial group velocity is slower than the speed of sound because the wave fronts do not propagate along the z-axis. Rather the path of waves are circuitous, following a longer path, spiraling around z-axis counter-clockwise or clockwise depending on the sign the mode m.

Secondly, the axial wave number k_z determines the behavior of the waves traveling along the duct, depending upon whether the square root term of the axial wavenumber is negative or positive. In other words, waves can only propagate in the z-direction if $k^{\pm}_{z,mn}$ is real, and are called *cut-on*. Highly cut-on modes approximate a plane wave (wave fronts perpendicular to duct axis). Conversely, when the square root term is purely imaginary the mode decays exponentially along the duct and is called *cut-off*. Cut-off modes are evanescent and do not radiate to the far field. Therefore, in order that the pressure field of a spinning

lobed pattern pattern to propagate, the circumferential Mach number, M_φ at which it sweeps the annuls walls, must be supersonic. So, if the helical blade tip Mach number is smaller than the speed of sound, the rotor does not emit sound into the far field. This quantization of discrete modes is equivalent to the radiating and evanescent modes of the classical wavy wall problem.

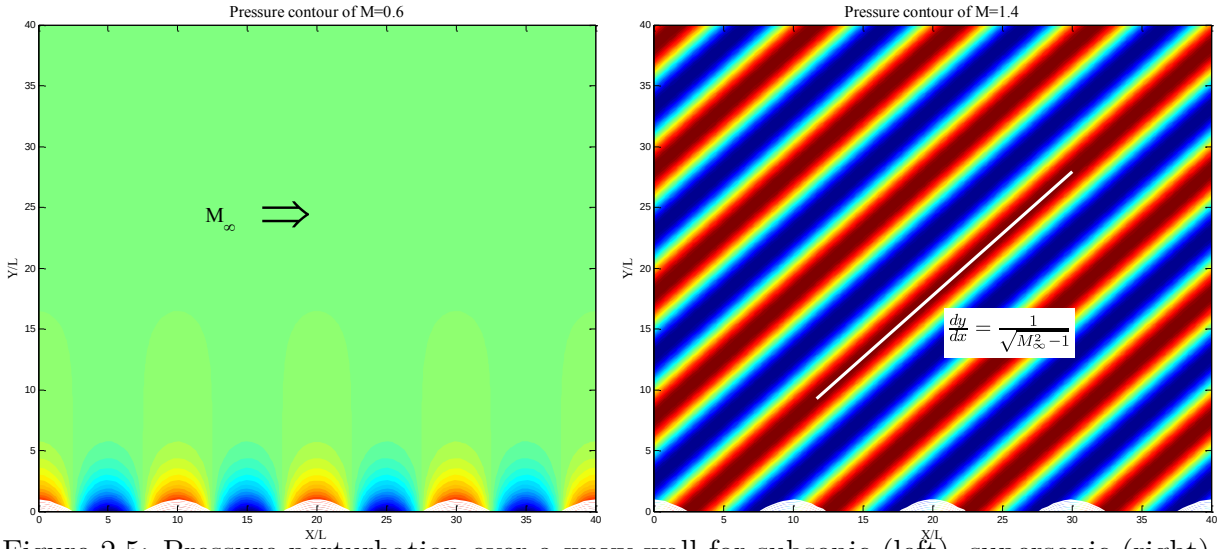

Figure 2.5: Pressure perturbation over a wavy wall for subsonic (left), supersonic (right).

Figure 2.5 presents pressure contours for the canonical wavy wall problem. A upstream flow moves over a wavy wall with small height variations. For any velocity that is below the speed of sound, the pressure waves decay exponentially with distance from the wall [40]. This phenomenon is illustrated in the contour plot to the left in Fig. 2.5. As the freestream velocity increases to a speed that is sonic or greater (right image in Fig 2.5), the pressure waves reach out from the wall to infinity (theoretically) along straight lines. Theses lines are inclined at the Mach angle with respect to the flow.

A similar phenomenon occurs for duct modes. For a given mode, m, having m circumferential variations, or lobes (i.e. number of blades), the modes can radiate or decay like the wavy wall problem. If the spin rate is supersonic, the sound pattern propagates in a spiral fashion through the duct from right to left as featured in bottom left image of Fig. 2.6. A slice of the $r - z$ plane is exhibited for the supersonic tip speed. Transverse acoustic field

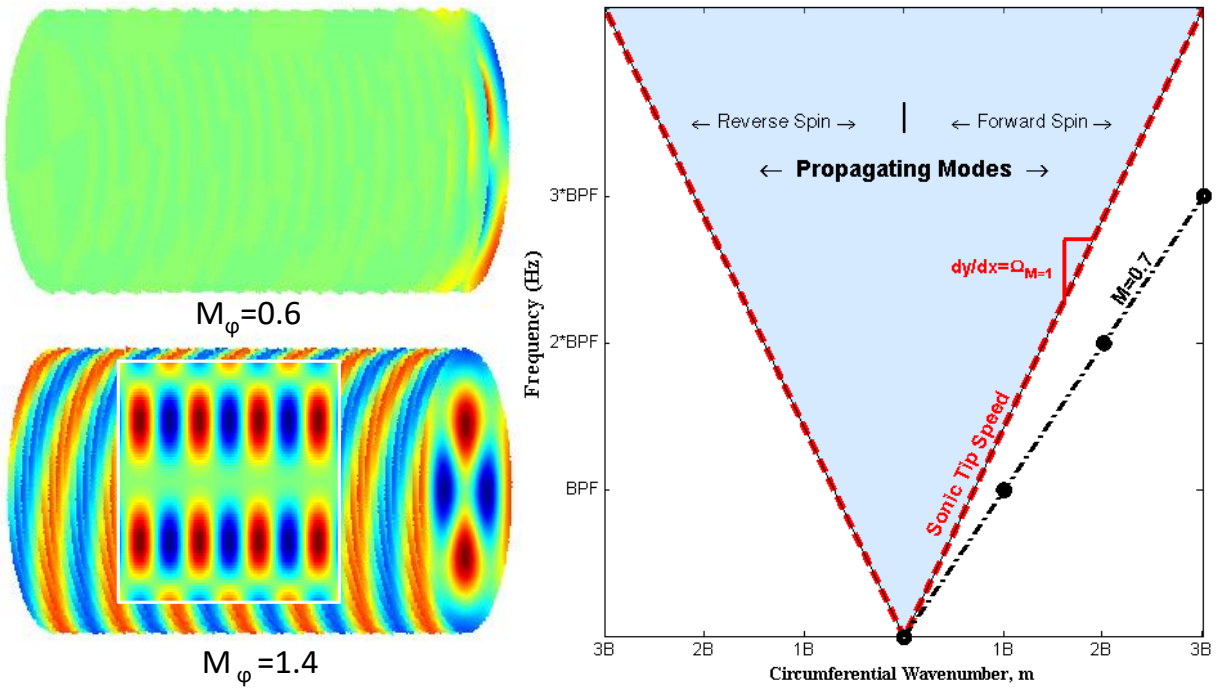

Figure 2.6: Pressure perturbation from a wave guide for a subsonic (top), and supersonic rotor (bottom) for the circumferential and radial mode $m = 2$, $n = 2$. Right image depicts modal-frequency spectrum of ducted fan noise.

.

patterns are observed. This is because the acoustic field must have zero tangential velocity at the walls of the waveguide, so the transverse pattern of the acoustic field is restricted to those that fit between the walls. On the other hand, if the rotor mode velocity is subsonic, the wave equation gives a solution where the amplitude decays exponentially with distance from the source according to upper left image of Fig. 2.6. This attenuation is large in practice, so that all modes that spin less than this critical mode have negligible far field noise effect. No pattern will propagate unless its outer wall sweep speed is supersonic. Application of the double Fourier transform (at the rotor tip) in angular location and time generate a spectral function with respect to circumferential wave number and frequency [19]. This leads to the so-called modal-frequency spectrum shown in Fig. 2.6. When the phase speed of the fluctuations becomes supersonic, they produce a radiating wave field as emphasized by the light blue region. For the rotor tones, the amplitude of the spectral components is represented by spikes (or δ-functions), and are designated by circular symbols either filled

or unfilled for cut-off (•) and cut-on (∘) modes, respectively. The differences between the radiating and evanescent waves, like the cut-off or cut-on modes, lies in the term $\sqrt{1-M^2}$ which determine the elliptical or hyperbolic nature of the governing dynamics.

To summarize, to generate far field noise the rotor tip must be *supersonic*. However, the next section will introduce a important mechanism that allows radiation for fan spinning with subsonic tip speeds.

2.2 Rotor-Stator Interaction

Downstream of the fan are stators. One factor leading to loss of efficiency in the engine is the induced tangential velocity or swirl to the wake. The generation of swirl consumes energy but does not contribute to thrust. To recover the swirl losses, stationary blades called stators are added behind the rotor [43]. However, significant distortion in the flow field occurs since each stator modifies the flow field generated by the previous blade row as depicted in Fig. 2.6. Typical fan applications have rotor-stator spacing of more than one rotor chord. This allows the viscous wakes and trailing vortex to disperse before interacting with the stator [35]. When compared to the mean flow, the wake velocity deficits at the stator rows are small. These small disturbances allow for the governing equations of the rotor wake influence to be linearized. Thus, to reduce noise, its is not the wake velocity deficit itself that must be reduced, but the acoustic coupling between the two blades rows.

Consider a two-dimensional cascade, shown in the left panel of Fig. 2.7. Approaching this problem using two-dimensional approximations gives insight into the basic interaction mechanism. A drawing of the interaction is shown in the right cartoon of Fig. 2.7. The fan blades and wakes are moving to the left at velocity Ωr, where r and Ω are the radial distance and angular frequency, respectively. The wakes are convected by the mean flow before colliding and interacting with the stationary stator blades. Since the stator pressure field depends on the rotor disturbance, the pressure on the stator may be expanded in terms

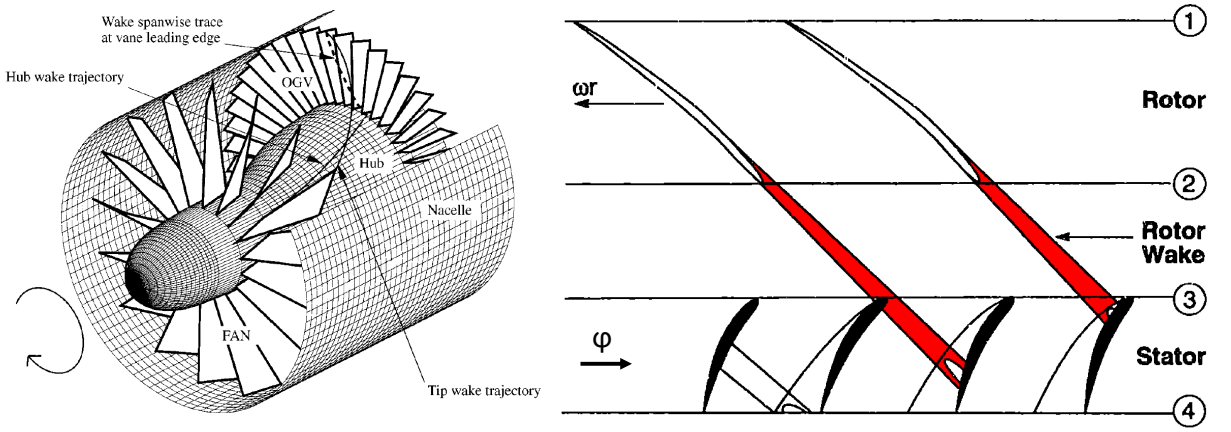

Figure 2.7: Depiction of the rotor wakes interaction with the stator (left). Schematic of rotor wake interaction (right). Image courtesy of Ed Envia of NASA Glenn Research Center [1].

of harmonics of the rotor.

$$p_{stator}(\varphi, t) = \sum_{h=-\infty}^{\infty} P_h(\varphi) e^{ihB\Omega t} \tag{2.9}$$

where h, B, Ω are the h^{th} BPF mode, the number of blades, and the angular speed, respectively. Description of the radial pressure distribution is intentionally avoided since it would unnecessarily complicate the analysis. Since the coefficient is only a function of azimuthal position, φ, it in may be expanded in Fourier Series over m-lobe azimuthal patterns

$$p_{stator}(\varphi, t) = \sum_{h=-\infty}^{\infty} \sum_{m=-\infty}^{\infty} P_{hm} e^{i(hB\Omega t - m\varphi)} \tag{2.10}$$

P_{hm} is the $(h, m)^{th}$ space-time component of the fluctuating pressure distribution due to the recurring blade events at a single vane. The form given is for a circumferential traveling wave. Consider an array of V identical vanes, equally spaced $\Delta\varphi = 2\pi/V$ radians apart. If the rotor is turning at Ω radians per second, the time required for a particular blade to turn from one vane position to the next is given by $\Delta t = \Delta\varphi/\Omega$ seconds. For a stator located

$\varphi - \Delta\varphi$ and time $t - \Delta t$ the pressure fluctuation is

$$p_{stator}(\varphi - \Delta\varphi, t - \Delta t) = \sum_{n=-\infty}^{\infty} \sum_{h=-\infty}^{\infty} P_{nm}(r) e^{i(hB\Omega(t-\Delta t) - m(\varphi - \Delta\varphi))} \tag{2.11}$$

For periodicity of the pressure field, the pressure fluctuation must be identical for every passing of a vane. In other words $p_{stator}(\varphi - \Delta\varphi, t - \Delta t) = p_{stator}(\varphi, t)$. Equating equation 2.10 and 2.11 yields:

$$2\pi k = m\Delta\varphi - hB\Omega\Delta t \tag{2.12}$$

where k is any integer. Replacing $\Delta\varphi = 2\pi/V$, and $\Delta t = \Delta\varphi/\Omega$ simplifies the above expression to the notorious Tyler-Sofrin expression [19]:

$$m = kV + hB \tag{2.13}$$

where h is the hth BPF tone of interest, and k is any integer. Through thoughtful selection of the rotor-to-stator ratio (B/V) it is possible to cut-off the fundamental mode. In practice, to cut-off the fundamental frequency the stator must be at least twice the number of blades.

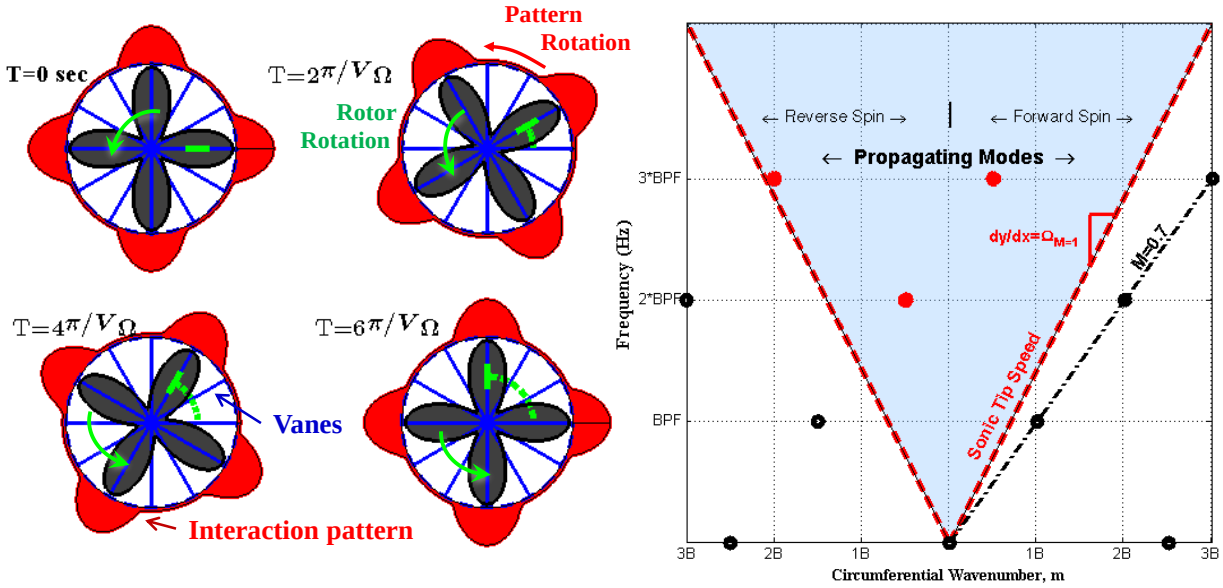

Figure 2.8: Rotor-stator interaction modal-frequency spectra for a subsonic rotor.

Consider the case of an 4 blade rotor interacting with a 12 vane stator drawn in Fig. 2.8. When V =12, B =3, the Tyler-Sofrin relationship $m = hB + kV$ predicts the existence of an $m = 4 - 0 = 4$ lobe pattern, at the first harmonic ($h = 1$ and $k = 0$). The rotor has been colored gray. In particular, one rotor blade is marked with a green line to differentiate it. The stator vanes are identified as blue rays radiating from the center. The red lobes mark the acoustic pulses when a blade passes the stator vane, generating a circumferential rotor-stator interaction mode. Lastly, the arrows indicates the direction of the rotor and of the interaction pattern. Successive snapshots show subsequent interactions as the rotor advances $1/V$ of a whole revolution. In order for the circumferential pattern to complete one full revolution, V frames are required. Therefore, the 4 lobe interaction pattern turns at $hB\Omega/m = \Omega$ radians per second, or at the blade passage frequency (BPF). One full rotation will produce not only this particular circumferential mode, but a superposition of modes occurring at higher circumferential wave numbers as depicted in the right image of Fig. 2.8. More circles are drawn in the modal-frequency spectrum along with an increase in propagating modes (red circles). Even if the rotor is moving subsonically at the tip, the angular velocity of an interaction mode can be supersonic. In this situation the mode will propagate in the duct and radiate to the far-field.

2.3 Sound Radiation from a Duct

So far we determined the solution for the propagation of noise in an infinite duct. Our major insight was the transfer of the pressure disturbances generated from the rotor through an rotating helical structure similar to that of the motion of stripes on a rotating barber pole. Only when the rotor tip speed was supersonic does sound radiate. However, rotor-stator interaction generates additional azimuthal modes that facilitate far-field radiation. Our endeavor now is to relate the internal fan noise to the radiation of sound from a duct. To address this problem, consider a cylindrical duct with annular cross section as sketched in

Fig 2.9. An accurate model of propagation of tonal noise is challenging owing to the presence of the shear layer which separates the bypass stream from the free field. However, certain aspects of the noise propagation and radiation process can be modeled by linearized equations [44]. Idealized solutions are useful to understand the essential elements of more realistic configurations. A further understanding of the modal behavior is therefore important for both interpretation and understanding of more complex sound fields.

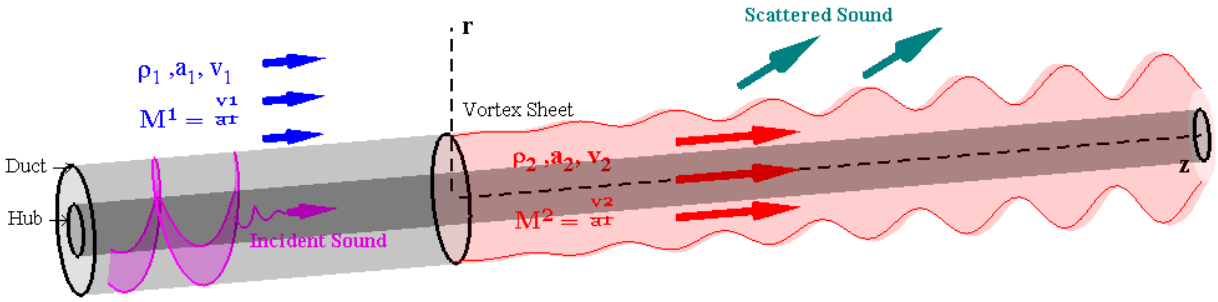

Figure 2.9: A sketch of the semi-infinite annular duct geometry.

The semi-infinite rigid circular duct is specified in cylindrical polar coordinates by $r = a$, and terminates at $z = 0$, i.e. $z < 0$. The duct carries a jet, which issues into an ambient mean flow while an inner cylindrical center body of radius $r = h$ extend infinitely axially. A vortex sheet of zero thickness separates the interface between two fluids which extends semi-infinitely into the region $r = a$, $z > 0$. The flow is perturbed by sound coming from inside the pipe due to the fan. By Kelvin's circulation theorem, the perturbed flow must be irrotational in each layer because the motion developed from an basic irrotational flow in each layer. The flow can therefore be described by a velocity potential $\phi(r, \varphi, z)$ that satisfies the non-dimensional convective wave equation [2, 3, 45]. For the ambient and jet flow, respectively:

$$\left(\frac{\partial}{\partial t} + M_1 \frac{\partial}{\partial z}\right)^2 \phi_1 = \nabla^2 \phi_1 \qquad r > a \tag{2.14}$$

$$C_1^2\left(\frac{\partial}{\partial t}+M_2\frac{\partial}{\partial z}\right)^2\phi_2=\nabla^2\phi_2 \qquad h<r<a \tag{2.15}$$

Note that the non-dimensional quantities M_1, M_2 are the Mach number in terms of the sound speed in the free stream, c_1. That is, M_2 is not the local Mach number. The ratio of the speed of sound is denoted $C_1 = c_1/c_2$. The hard wall, kinematic, dynamic, far field , and Kutta boundary conditions are:

$$\frac{\partial\phi}{\partial r}(a,\varphi,z)=0, \qquad z\leq 0 \tag{2.16}$$

$$\left(\frac{\partial}{\partial t}+M_1\frac{\partial}{\partial z}\right)\eta(z)=\left(\frac{\partial}{\partial t}+M_2\frac{\partial}{\partial z}\right)\eta(z)=\frac{\partial\phi}{\partial r}(a^{\pm},z) \qquad z\geq 0 \tag{2.17}$$

$$\left(\frac{\partial}{\partial t}+M_1\frac{\partial}{\partial z}\right)\phi_1(a^{+},z)=D_1\left(\frac{\partial}{\partial t}+M_2\frac{\partial}{\partial z}\right)\phi_2(a^{-},z) \qquad z\geq 0 \tag{2.18}$$

$$\phi\to 0 \; as \; |z|\to\infty \qquad\qquad \phi=O(|z|^{\frac{3}{2}}) \; as \; |z|\to 0 \tag{2.19}$$

where $D_1 = \rho_2/\rho_1$ is the ratio of the jet and ambient densities and $\eta(z)$ is the radial displacement of the vortex sheet. We split the total acoustic field as the sum of the incident wave ϕ and diffracted field ψ. The solution includes K, the Wiener-Hopf Kernel which encapsulate the physical behavior of the scattered acoustic field [46].

Let's inspect of the locations of its poles and zeros of the Wiener-Hopf kernel. The zeros are the root of the numerator when it is zeros. As depicted in Fig. 2.10 a group of zeros and poles is located close to the dash line defined by the angle $\pi/2-\epsilon$. Conversely, the poles are the found when the first term of K is zero. These poles are precisely the characteristic equations of the infinite annular duct. Hence, the poles of the Wiener-Hopf kernel equate to the acoustic modes of the duct. This means, the barber pole acoustic pattern persist in the flow region inside the shear layer. These acoustic modes travel upstream and downstream at $c_2 \pm U_2$. Due to the dispersive nature of the duct modes, waves with a higher frequency have larger group velocity (slope of dispersion curve) and thus will arrive at the far field

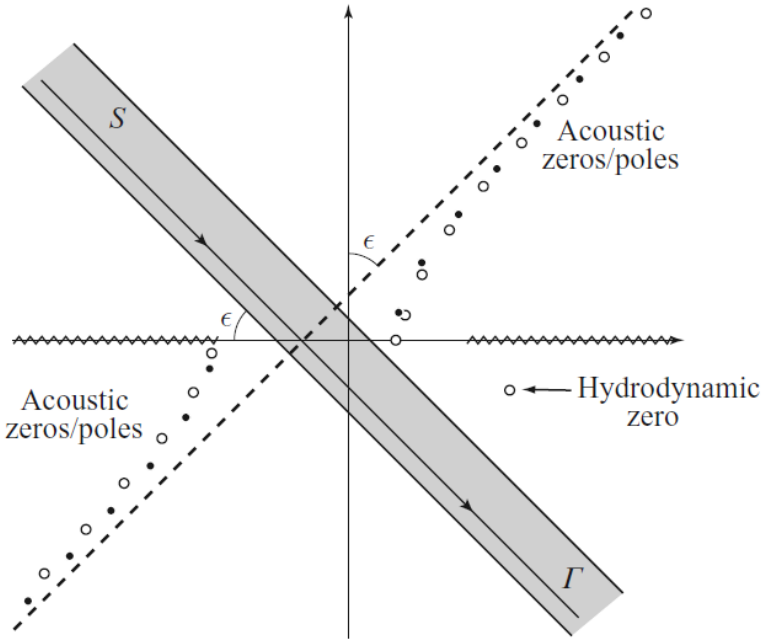

Figure 2.10: Location of zeros (∘), and poles (•) of the Wiener-Hopf kernel for annular jet operating with $\omega = 4$, M_2=5, $M_1 = 0.25$, $D_1 = C_1$ =1, h=0 . Image from Rienstra [2].

.

sooner than waves with a lower frequency. Another set of zeros exist that are related to the instability of the vortex sheet. In the case of a cold jet, the phase velocity according to high frequency approximation is found as:

$$v_p = \frac{M_1 + M_2}{2} \pm \frac{i}{2}\sqrt{1 - (\sqrt{1 + (M_2 - M_1)^2} - 2)^2} \tag{2.20}$$

Vortical modes convective velocities are similar to those predicted from Kelvin-Helmholtz instability. When the jet is subsonic, i.e. $M < 1$ the second term is always imaginary and represent the amplification of the instability which is driven by the difference of velocity between the two streams. The real part correspond to waves moving at the average speed of the two streams. This field is non-decaying in the downstream direction, and therefore contributes to the far field. However, it is purely hydrodynamic (involves no pressure variations) and is only significant near the vortex sheet. Such growth cannot continue indefinitely since at some stage the finite thickness of the shear layer will become important.

An interaction between acoustic and non acoustic modes takes place. Figure 2.11

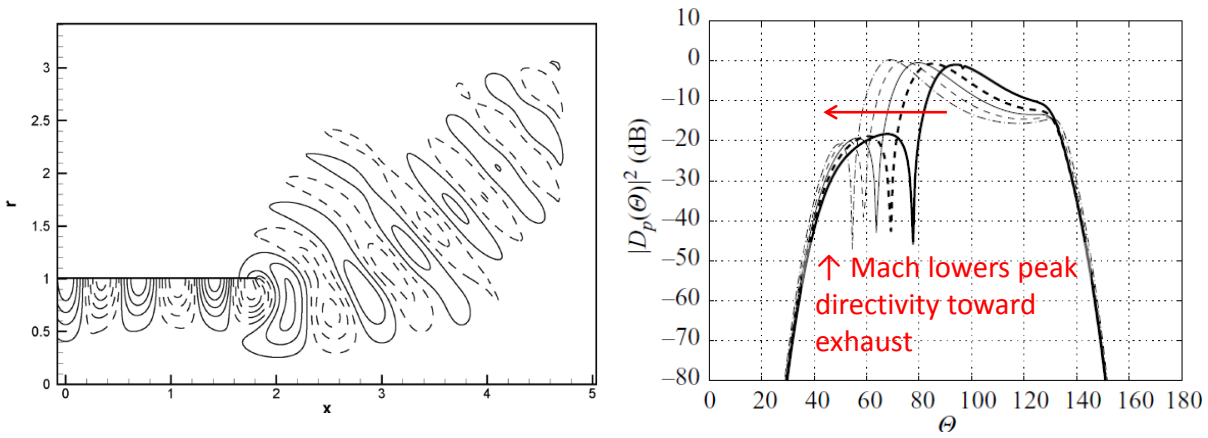

Figure 2.11: Pressure contours of semi-infinite duct (left), pressure directivity patterns in the far field for various freestream velocities from Huang [3] (right).

displays the pressure contours and pressure directivity patterns with varying external flow velocity while holding other parameters constant. The sound pressure perturbation contours demonstrates the modal solution of the duct persist outside. As the sound reaches the end, its radiates, convect, and refracts into the surrounding air. Furthermore, as the Mach number of the ambient increases from 0 to 0.45, the peak directuvity pattern shift toward the jet axis. A cone of cone of silence appears as the mean flow transport the acoustic disturbances. Computational experiments using more realistic configurations show good agreement with analytical results, and provides an understanding of the influence of the mean flow convection/refraction effects. Fig. 2.12 displays instantaneous pressure field associated for takeoff (left) and quiescent (right) conditions. Comparison of the images revels the acoustic waves exiting the nozzle with a lower angle with respect to the exhaust [4]. This deflection phenomenon confirms the interaction of the acoustic disturbance and shear flow.

2.4 Connecting Analytic Solutions to Noise Model

The development a model of radiating tonal noise from an exhaust requires an theoretical understanding of characteristics of duct modes. Key findings are:

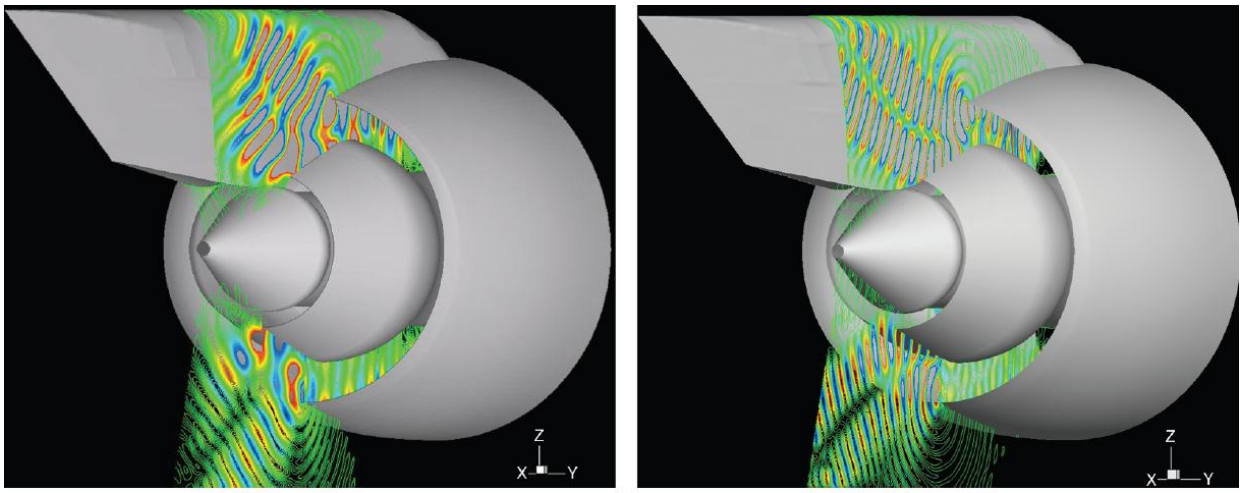

Figure 2.12: Instantaneous perturbed aft pressure field radiated by the exhaust under takeoff $M_\infty = 0.26$, and into a quiescent free stream $M_\infty = 0$ from Redonnet [4].

1. Tonal noise is generated due to the thickness and loading of the rotor blades. The rotor acoustic effect is represented as a Fourier series of the pressure field with circumferential order, m.

2. Radiating rotor-only duct modes demand a supersonic tip speed. Acoustic fluctuations induced by the rotor are transferred through a rotating helical structure similar to that of the motion of stripes on a rotating barber pole.

3. The rotor-stator interaction phenomenon allows the radiation of modes corresponding to a subsonic rotor tip speed. Furthermore, Tyler and Sofrin's rule dictates the dominant azimuthal modes which has supersonic circumferential tip velocity.

4. Sound is forced to propagate along the duct until it reaches the end, the fan nozzle, at which point it is free to radiate into the surrounding. The shear layer refracts the acoustic pressure altering the direction of peak radiation.

5. Radiation of duct noise is encapsulated by the Wiener-Hopf kernel. Convective velocities of the acoustic waves are govern by the duct propagation. Vortical modes convective velocities are similar to those predicted from Kelvin-Helmholtz instability.

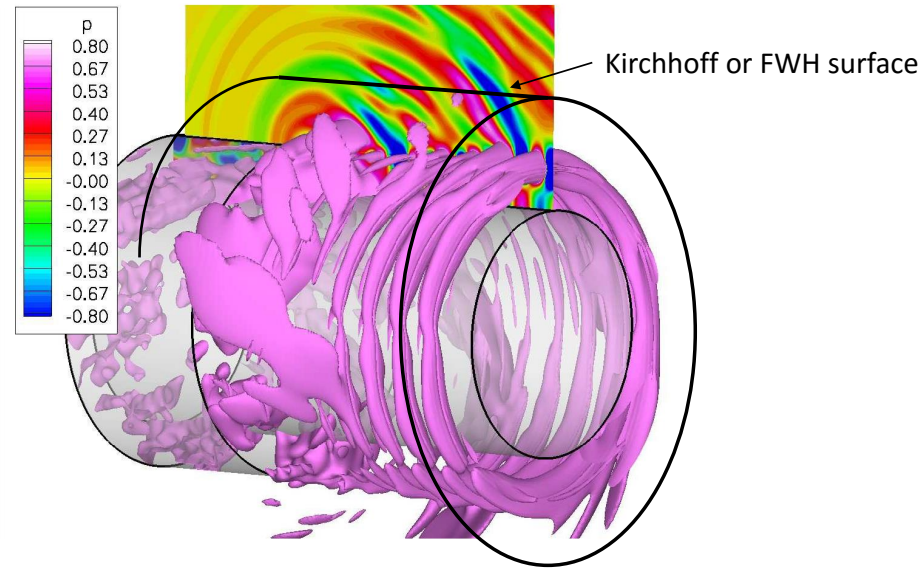

Figure 2.13: Pressure perturbation fields from Reboul [5].

Prediction of the acoustic far field is implemented by a cylindrical Kirchhoff surface enclosing the exhaust of the turbofan. The surface is sufficiently close to the exhaust and feels the footprint of the modal pressure disturbance generated by the rotor and rotor-stator interaction as illustrated in Fig 2.13. The blade passage frequencies are known. Furthermore, numerous azimuthal microphone array surveys, have found the dominate radiating (supersonic circumferential tip velocity) azimuthal modes as those predicted by Tyler and Sorfin [47, 48]. Thus, we assume that the azimuthal mode is determined by the Tyler-Sofrin relation [19]

$$m = hB + kV \tag{2.21}$$

where B is the number of blades on the fan and V is the number of stator vanes. On the other hand, h and k is the harmonic, and a arbitrary integer, respectively. Observation of spiral structure highlighted in finding 2, motivated prescribing the pressure perturbation on the Kichhoff surface as helical traveling wave. Written mathematically,

$$p_w \propto e^{i(m\varphi - \omega t + k_z z)} \tag{2.22}$$

where m, ω, k_z are the azimutal mode, angular frequency, and axial wavenumber, respectively. Estimates of the wavenumber, k_z (or more importantly the convective velocity) may be obtained from the knowledge of the property of the Wiener-Hopf kernel. By assuming a locally constant cross section the dispersion relation for azimuth mode m and h harmonic is estimated by:

$$k_{z,mn}^{\pm} = \frac{-M_2 C_1^2 \pm \sqrt{C_1^2 - (1 - M_2^2 C_1^2)(\frac{\mu_{mn}}{\omega})^2}}{1 - M_2^2 C_1^2} \tag{2.23}$$

where k_0 is the acoustic frequency, M is the mean flow Mach number, $k_{z,mn}$ is the wave number of the right $(+)$ and left $(-)$ traveling modes. Due to the dispersive nature of the duct modes, waves with a higher frequency will propagate faster to the far field than longer wavelength waves. μ_{mn} are the roots of the wall boundary condition.

$$\frac{d}{dz}[Y_m(zh)]J_m(z) - \frac{d}{dz}[J_m(zh)]Y_m(z) = 0 \tag{2.24}$$

in which $J_m(z)$ and $Y_m(z)$ are the Bessel function of the first and second kind of order m, and h is the hub-to-tip ratio of the duct. Realistic wavenumber will deviate depending on the area variation of the nozzle. Numerical optimization will provide the actual convective velocity, but these analytical expressions provides an good start and sanity check of our computational methods. Lastly, the amplification and decay of the acoustic waves due to the duct geometry and shear layer influence are reproduced by an envelope function, $p_o(z)$. Combining these findings, the pressure prescribed on the surface is:

$$p(m, r_0, z, \varphi, t) = p_0(z) e^{i(m\varphi - \omega t)} \tag{2.25}$$

Chapter 3

Noise Source Modeling, Parametrization, and Scattering Prediction

So far, we discussed the principal sources of fan noise and their respective generating mechanics. This chapter will propose a low-order, physics-based model of the aft fan noise source. Here we start with a deterministic noise source model based on the wavepacket ansatz. This model contain a finite set parameters that must be determined experimentally. In the second half, we will discuss the reconstruction of the parameters of the wavepacket model from measurements and computational scattering predictions.

3.1 Wavepacket Model Formulation

In a infinite annular duct with uniform flow, any acoustic field can be decomposed as a sum of rotating mode patterns with circumferential and radial (order m and n) pressure distributions. These are elementary solutions to the convective Helmholtz's equation. The sound is forced to propagate along the duct until it reaches the end, the fan nozzle, at

which point it is free to radiate into the surrounding. We aim to mimic on a cylindrical surface the footprint of these modal structure generated by the fan. When viewed from the outside the nacelle, the influence of these modal structure are approximated by a amplitude modulated traveling wave on a control surface surrounding the exit of the nozzle. The spatiotemporal amplification and decay behavior reflects the influence of the complex nozzle geometry, rotor/stator interaction, and shear layer. For the sake of simplification, pylon/ bifurcation interaction, and non-symmertic effects are not considered. Low-order modeling enables predictions of the radiated sound and its scattering around objects without inordinate computational resources. This wavepacket model is based on the foundational work by Tam and Burton [49], Cirghton and Huerre [50], Avital et al [51], and Papamoschou et al [16].

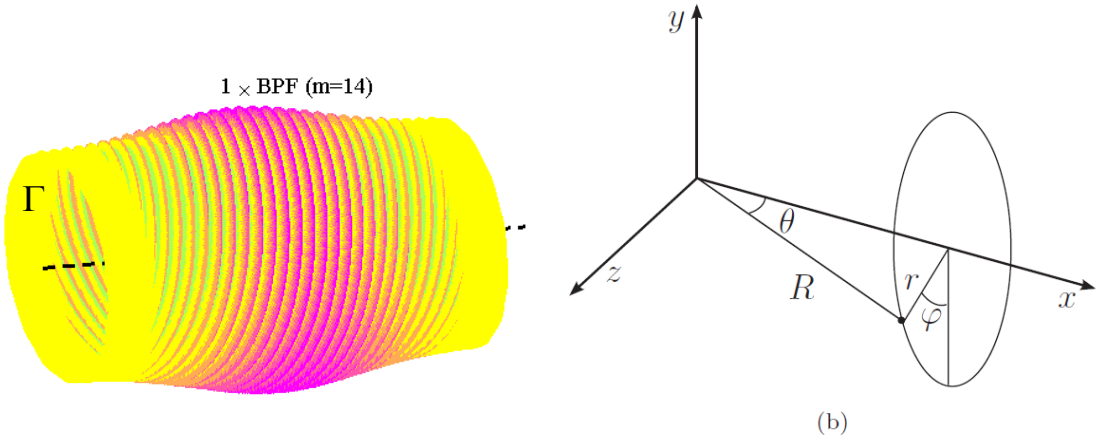

Figure 3.1: Fan noise source model with corresponding coordinate system, adapted from Salvador Mayoral.

Consider a cylindrical surface Γ of radius r_o that surrounds the fan whose axis is aligned with the ducted fan center-line as sketch in Fig. 3.1. The fan exhaust is replaced by a cylinder of radius $r = r_0$ on which we prescribe the pressure pertubation [52]:

$$p(m, r_0, z, \varphi, t) = p_0(z)e^{i(m\varphi - \omega t)} \tag{3.1}$$

where r, φ, and z correspond to the cylindrical polar coordinates for radial position, azimuthal angle, and axial position, relative to the downstream axis, respectively. In addition,

m is the azimuthal mode, t represents time, and ω is the angular frequency. Lastly, $p_0(z)$ describes the shape or modulation envelope of the wavepacket. This amplification-decay envelope represent the refraction phenomenon of the shear layer on the acoustic waveform, and duct effects. A number of such partial field on the radiator surface is necessary to replicate the characteristics of the pressure field at a given frequency. Specifically, the noise source will be represented as an aggregation of deterministic partial fields that, overall, sum up to capture the complex, extended and directional aft soundscape of the ducted fan. The propagation of the pressure fluctuations away from the source is governed by the wave equation. In three-dimensional cylindrical polar coordinates the mathematical statement for a stationary medium is:

$$\frac{1}{a_\infty^2}\frac{\partial^2 p}{\partial t^2} - \left[\frac{1}{r}\frac{\partial}{\partial r}(r\frac{\partial p}{\partial r}) + \frac{1}{r^2}\frac{\partial^2 p}{\partial \varphi^2} + \frac{\partial^2 p}{\partial z^2}\right] = 0 \tag{3.2}$$

To guarantee that the far field solution for p represents an outgoing wave (i.e. no reflections), the *Sommerfeld radiation condition* at $r \to \infty$ is imposed

$$\lim_{r\to\infty}\left(\frac{\partial p}{\partial r} - ikp\right) = 0 \tag{3.3}$$

where k is the spatial frequency of a wave (acoustic wavenumber). The wave equation (3.2) with the prescribed pressure boundary condition on the surface (3.1), along with the Sommerfeld condition (3.3) may be solved using Fourier transform. Converting the acoustic pressure from a time/space domain (φ, z, t) representation to the frequency/wave number domain (m, k_z, ω) can be accomplished using the multidimensional transform pair:

$$\mathscr{P}_m(m, k_z, \omega) = \int_{-\infty}^{\infty}\int_{-\infty}^{\infty}\int_{-\pi}^{\pi} p(\varphi, z, t)e^{[i(\omega t - k_z z - m\varphi)]}d\varphi dt dz$$

$$p(\varphi, z, t) = \frac{1}{(2\pi)^3}\sum_{m=-\infty}^{\infty}\int_{-\infty}^{\infty}\int_{-\infty}^{\infty} \mathscr{P}_m(m, k_z, \omega)e^{[-i(\omega t - k_z z - m\varphi)]}d\omega dk_z \tag{3.4}$$

where m, k_z, ω are the azimuthal mode, axial wavenumber, and angular frequency. Summa-

tion over the azimuthal mode occurred since the wavenumber m is discrete. Transformation of the wave equation to the frequency domain and simplification yield a second-order linear differential equation with variable coefficient known as Bessel's differential equation.

$$r^2\frac{\partial^2 \mathscr{P}_m}{\partial r^2} + r\frac{\partial \mathscr{P}_m}{\partial r} + (r^2 {k_r}^2 - m^2)\mathscr{P}_m = 0 \tag{3.5}$$

where k_r is the radial wave number, $k_r = \sqrt{k^2 - k_z^2}$. The general solution is given by:

$$\mathscr{P}_m(r, m, k_z, \omega) = C_{m1}(k, \omega)H_m^{(1)}(k_r r) + C_{m2}(k, \omega)H_m^{(2)}(k_r r) \tag{3.6}$$

with C_{m1}, C_{m2} as constants and $\mathscr{P}$ denotes the spatial Fourier transform of $p(z)$. The Hankel function of the first and second kind, $H_m^{(1)}$ and $H_m^{(2)}$ are a linear combination of Bessel functions of the first and second kind defined as

$$H_m^{(1)}(z) = J_m(z) + iY_m(z) \qquad H_m^{(2)}(z) = J_m(z) - iY_m(z) \tag{3.7}$$

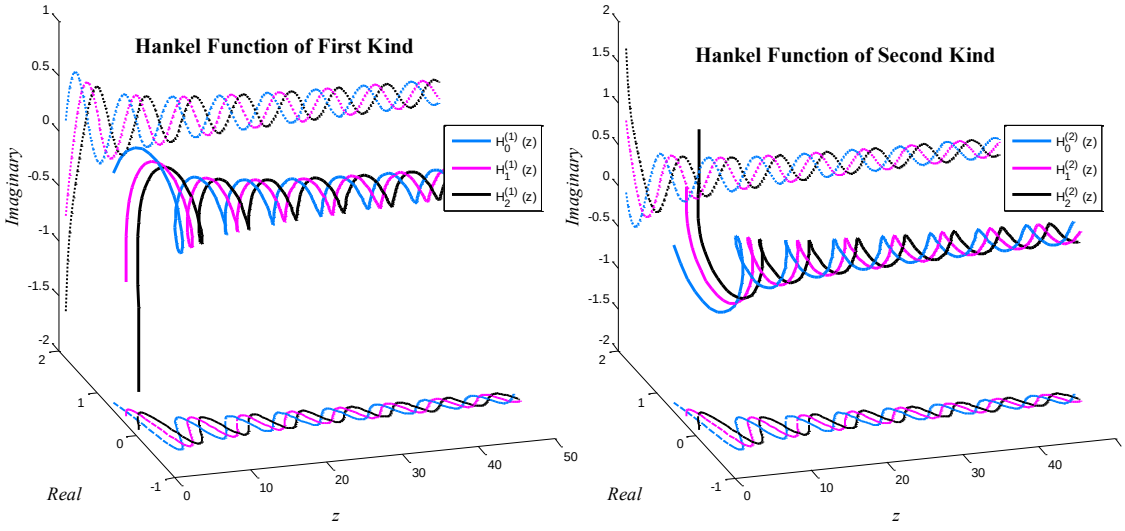

Figure 3.2: Graph of the Hankel function of the first and second kind in the complex plane.

Fig 3.2 plots the general behavior of the complex value function. The Hankel functions form spirals, spinning around in the complex plane. Spirals can be either left-handed or

right-handed (rotating clockwise or counterclockwise). Thus, Hankel functions are used to express outward- and inward-propagating cylindrical wave solutions of the cylindrical wave equation, respectively. Imposing the *Sommerfeld conditions*, eliminates inwards moving waves, or $C_{m2} = 0$. This correspond to ignoring clockwise modes as depicted in the right image of fig. 3.2. The variation of C_{m1} is determined by the prescribed variation of the pressure on the cylindrical surface, $p_0(z)$. In Fourier space the boundary condition imposed on the cylindrical surface becomes:

$$\begin{aligned}\mathscr{F}(p_0(z)e^{i(m\varphi-\omega_0 t)}) &= \int_{-\infty}^{\infty}\int_{-\infty}^{\infty}\int_{-\pi}^{\pi} p_0(z)e^{i(m\varphi-\omega_0 t)}e^{[i(\omega t-k_z z-n\varphi)]}d\varphi dt dz \\ &= \int_{-\pi}^{\pi} e^{-in\varphi}e^{im\varphi}d\varphi \int_{-\infty}^{\infty} e^{-it\omega_0}e^{it\omega}dt \int_{-\infty}^{\infty} p_0(z)e^{-ik_z z}dz \\ &= (2\pi)(2\pi\delta(\omega-\omega_0))(\mathscr{P}_{0m}(k_z)) \\ &= (2\pi)^2\delta(\omega-\omega_0)\mathscr{P}_{0m}(k_z)\end{aligned} \tag{3.8}$$

where orthogonality of the azimuthal wavenumber, m, was utilized. Applying the prescribed pressure boundary conditions to determine the coefficient gives the Fourier transformed pressure as:

$$\mathscr{P}_m(r,m,k_z,\omega) = \frac{(2\pi)^2\delta(\omega-\omega_0)\mathscr{P}_{0_m}(k_z)}{H_m^{(1)}(k_r r_0)}H_m^{(1)}(k_r r) \tag{3.9}$$

Taking the inverse Fourier transform,

$$p(m,r_0,z,\varphi,t) = \frac{1}{(2\pi)^3}\int_{-\infty}^{\infty}\int_{-\infty}^{\infty}\frac{(2\pi)^2\delta(\omega-\omega_0)\mathscr{P}_0(k_z)}{H_m^{(1)}(k_r r_0)}H_m^{(1)}(k_r r)e^{[-i(\omega t-k_z z-m\varphi)]}d\omega dk_z \tag{3.10}$$

Using the definition of $\delta(\omega-\omega_0)$ to simplify the acoustic pressure in the time/space domain as [49]:

$$\begin{aligned}p(m,r,\varphi,t) &= \frac{1}{2\pi}e^{-i[w_o t+m\varphi]}\int_{-\infty}^{\infty}\mathscr{P}_0(k_z)\frac{H_m^{(1)}(k_r r)}{H_m^{(1)}(k_r r_0)}e^{ik_z z}dk_z \\ k_r &= \sqrt{k^2-k_z^2}, \qquad \frac{-\pi}{2} < arg(k_r) < \frac{\pi}{2}\end{aligned} \tag{3.11}$$

where the argument (or phase) of the radial eigenvalue k_r is bounded to ensure the behavior of $H_m^{(1)}(k_r r)$ forms a radially outward spiral in the far field- i.e. satisfies Sommerfeld condition. The formulation recreates the radiative and nonradiative behavior typical of helical waves. A wavepacket moving with a phase speed that is subsonic generates an evanescent acoustic field. Conversely, a wave moving with a supersonic phase speed radiates. Equation 3.11 is the exact solution to the linearized acoustic problem, valid everywhere for $r \geq r_0$. Once the wavepacket shape $p_0(z)$ is determined, Eq. 3.11 yields the incident field p_i on the object surface and at the field points.

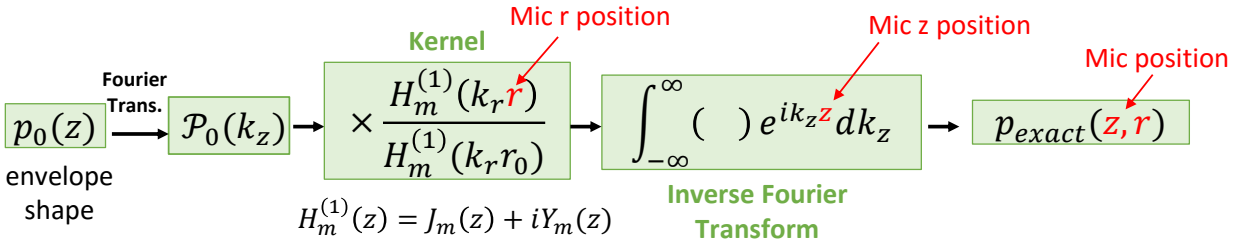

Figure 3.3: Flowchart for calculation of near-field pressure.

Equation 3.11 can be viewed as an integral operator converting the prescribed surface shape, $p_0(z)$ into pressure readings at the field points, $p(r, z)$. Steps for the calculation of the near-field pressure are depicted in Fig. 3.3. To compute the pressure field generated by the wavepacket shape $p_0(z)$, $z \in (-\infty, \infty)$ (or limits that are sufficiently far from wavepacket center), first involves taking the forward FFT of $p_0(z)$ to obtain $\mathscr{P}_0(k_z)$. The Fourier transformed boundary condition imposed on the cylindrical surface $\mathscr{P}_0(k_z)$ is then multiplied by the Hankel kernel. This kernel defines the influence of the prescribed pressure $\mathscr{P}(k_z)$ on the acoustic pressure field outside the cylinder at field point located with radial distance r. To obtain the pressure at a field point z, we sum (integrate) influences of all wavenumber k_z through convolution with the inverse Fourier kernel function $e^{ik_z z}$. It was found that direct evaluation of the integral at a field point z, is more efficient than taking the inverse FFT of product of $\mathscr{P}_0(k_z)$ and the Hankel kernel and interpolating to the field point z.

The near field cross-spectral density is the acoustic pressure (Eq. 3.11) times its com-

plex conjugate. For a reference microphone located at cylindrical coordinate (r_m, z_m), and a 2nd field point at (r_n, z_n) the cross-spectral density is:

$$S_{model,near}((r_m, z_m), (r_n, z_n)) = \frac{1}{(2\pi)^2}\left(\int_{-\infty}^{\infty} \mathscr{P}_0(k_z) \frac{H_m^{(1)}(k_r r_m)}{H_m^{(1)}(k_r r_0)} e^{ik_z z_m} dk_z \right)\left(\int_{-\infty}^{\infty} \mathscr{P}_0(k_z) \frac{H_m^{(1)}(k_r r_n)}{H_m^{(1)}(k_r r_0)} e^{ik_z z_n} dk_z \right)^* \quad (3.12)$$

3.1.1 Far Field Approximation

Most acoustic measurements are preformed in the far-field. To obtain an expression for the acoustic pressure in the far field, Fig. 3.2 illustrates Hankel functions of the first and second kind look like decaying oscillations. In fact for large z, $H_m^{(1)}$ and $H_m^{(2)}$ may be accurately approximated by the pure complex exponential behavior:

$$H_m^{(1)}(z) \sim \sqrt{\frac{2}{\pi z}} e^{[i(z - \frac{\pi}{4} - \frac{m\pi}{4})]} \qquad as \qquad z \to \infty \quad (3.13)$$

Imposing the asymptotic form of the Hankel function with argument $z = k_r r$ to the acoustic pressure gives

$$p(m, r, \varphi, t) = \frac{1}{\sqrt{2\pi^3}} e^{i[-\omega t + m(\varphi - \frac{\pi}{2}) - \frac{\pi}{4}]} \int_{-\infty}^{\infty} \frac{\mathscr{P}_0(k_z)}{\sqrt{k_r r} H_m^{(1)}(k_r r_0)} e^{i[k_z z + k_r r]} dk_z \quad (3.14)$$

Denoting the terms in the envelope and phase in the oscillatory integrand as $F(k_z)$, $\psi(k_z)$, respectively.

$$F(k_z) = \frac{\mathscr{P}_0(k_z)}{\sqrt{2k_r r_0} H_m^{(1)}(k_r r_0)} = \frac{\mathscr{P}_0(k_z)}{\sqrt{2k_r R \sin\theta}\ H_m^{(1)}(k_r r_0)}$$

$$\psi(k_z) = k_z z + k_r r = R(k_z \cos\theta + k_r \sin\theta) \quad (3.15)$$

where we converted to spherical polar coordinates, using $r = R\sin(\theta)$ and $z = R\cos(\theta)$, with R as the radial position and θ is the polar angle [53]. The integral above may be simplified using the method of stationary phase. This method provides an asymptotic expansion of

integrals with an rapidly oscillating integrand. Rapid oscillations of the exponential term mean that the generalized Fourier integral is approximately zero over those regions. Thus, the only non-zero contributions to the integral occur in regions of the integration range where the phase is flat. The method of stationary phase gives the following result for the pressure in the far field

$$p(m,r,\varphi,t) \approx -\frac{i}{\pi R}\frac{\mathscr{P}_0\left(\frac{\omega}{a_\infty}\cos\theta\right)}{H_m^{(1)}\left(\frac{\omega}{a_\infty}r_0\sin\theta\right)}e^{i(\frac{\omega}{a_\infty}R-\omega t+m\varphi)} \tag{3.16}$$

where R is the distance of the observer from the origin, and θ is the polar angle from the downstream duct axis. Using 3.16, the modulus square of the acoustic pressure yeilds the auto-spectral density of the far field pressure [54].

$$S_{model,far}(\theta) = \frac{1}{(\pi R)^2}\left|\frac{\mathscr{P}_0\left(\frac{\omega}{a_\infty}\cos\theta\right)}{H_m^{(1)}\left(\frac{\omega}{a_\infty}r_0\sin\theta\right)}\right|^2 \tag{3.17}$$

The far field cross-spectral density is the acoustic pressure (Eq. 3.16) times its complex conjugate.

$$S_{model,far}(\theta_m,\theta_n) = \frac{1}{(\pi R)^2}\frac{\mathscr{P}_0\left(\frac{\omega}{a_\infty}\cos\theta_m\right)}{H_m^{(1)}\left(\frac{\omega}{a_\infty}r_0\sin\theta_m\right)}\frac{\mathscr{P}_0^*\left(\frac{\omega}{a_\infty}\cos\theta_n\right)}{H_m^{(2)}\left(\frac{\omega}{a_\infty}r_0\sin\theta_n\right)} \tag{3.18}$$

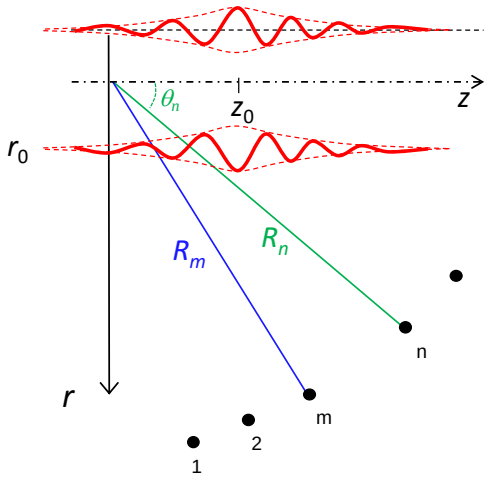

Figure 3.4: Schematic of cross-spectra between two microphones.

Eq. 3.18 was simplified using the complex conjugate property of the Hankel function of the 1st kind. In addition Fig. 3.4 illustratse the microphone layout used in the cross-spectral density calculation between microphone m, and n with polar angle, θ_m, θ_n, respectively.

3.2 Wavepacket Parameterization

Here we focus on the problem of recovering the object information from the acquired near and far-field microphone signals. Inferring the characteristics of a sound source based on its radiated sound alone is an ill-posed problem. There exist a infinite set of parameters A_k that defines the wavepacket shape. Suppose a axis-symmetric jet (no azimuthal variation) with an asymetric Gaussian amplitude modulated wave along the axial direction on a cylindrical surface $r = r_0$

$$p(r_0, z, t) = \epsilon B(z) e^{i(k_z z + m\varphi - \omega t)}$$

where

$$B(z) = \begin{cases} \exp\left(-(\frac{z-z_0}{b_1})^2\right) & \text{if } z \leq z_0 \\ \exp\left(-(\frac{z-z_0}{b_2})^2\right) & \text{if } z > z_0 \end{cases} \tag{3.19}$$

for a given harmonic with angular velocity ω, the wavepacket is defined by the parameter vector A_k:

$$A_k = \begin{pmatrix} \epsilon \\ k_z/a_\infty \\ b_1/D_o \\ b_2/D_o \\ z_o/D_o \end{pmatrix} \tag{3.20}$$

where $k_z = \omega/U_c$ is the wavepacket axial wavenumber, D_0 is the exit diameter of the nozzle, U_c is the convective velocity, and b_1, b_2, ϵ are parameters that serve as "knobs" to tune the wavepacket shape. The parameterization process is faster when the wavepacket envelope

function has a analytical Fourier transform. In this case, the Fourier transform has the exact form:

$$\mathscr{P}_0(k) = \frac{\epsilon\sqrt{\pi}}{2} e^{iz_0(k-k_z)}[b_2 W(\beta_2) + b_1 W^*(\beta_1)] \tag{3.21}$$

where

$$\beta_1 = b_1(k - k_z) \qquad \beta_2 = b_2(k - k_z) \tag{3.22}$$

$$W(z) = e^{-x^2} erfc(iz) \qquad (Faddeeva function) \tag{3.23}$$

3.2.1 Parameterization based on Cross-spectra

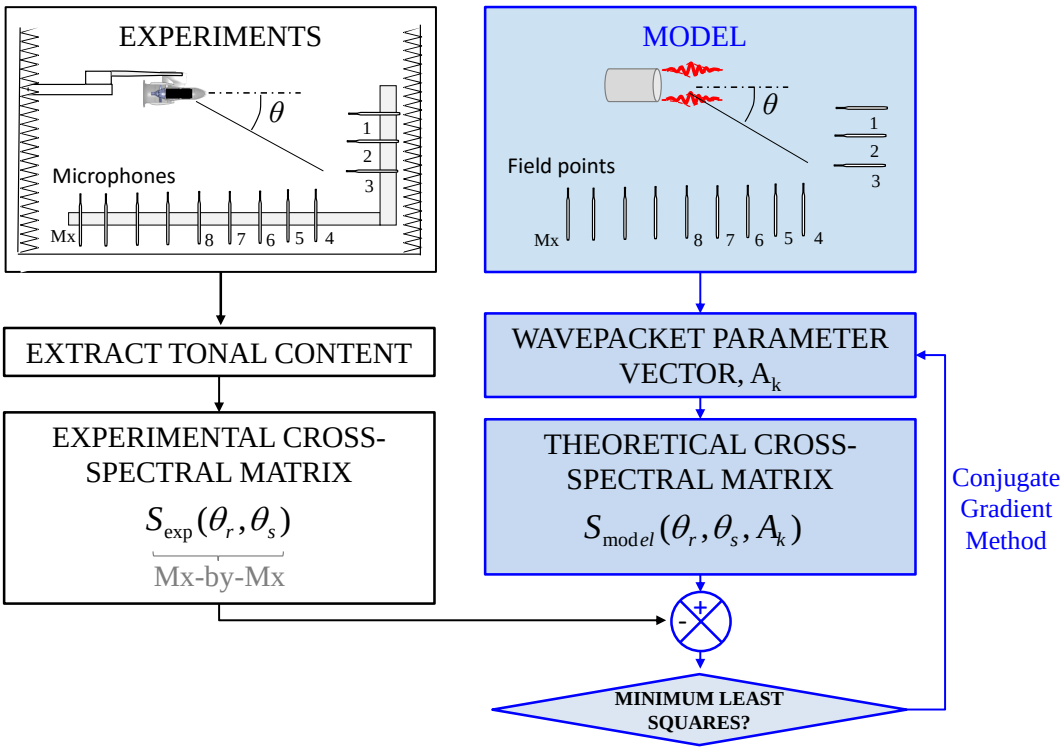

Figure 3.5: Source Parameterization Procedure

Parameterization refers to the methodological process used to determine the best parameters needed to express the wavepacket model. The parameterization model is based on experimental measurement of the cross-spectra density, see Fig. 3.5. Following aeroacoustic testing of our ducted fan, the experimental cross-spectrum S_{exp} is known for a given blade passage frequency (BPF) and at discrete radial, R_m, and polar positions, θ_m, along the array

consisting of Mx microphones ($m = 1, \ldots, Mx$). For a given BPF, the azimutal mode m is given by Tyler and Sofrin's rule. A starting value of the wavenumber k_z is estimated from the analytical dispersion relation. The minimization process aims to select the optimal parameter vector A_k in a way that minimizes the difference between the modeled $S_{model}(f)$ and the experimental cross-spectral density $S_{exp}(f)$ at all the measurement polar angles. The parameter vector A_k is obtained through the least-square minimization of:

$$F(A_k) = \frac{1}{M} \sum_{m,n=1}^{M} \left| \frac{S^*_{exp}(\theta_m, \theta_n) - S^*_{model}(\theta_m, \theta_n, A_k)}{S^*_{exp}(\theta_m, \theta_n)} \right|^2 \tag{3.24}$$

where the function sums over the unique values of the cross-spectra matrix consisting of entries on and above the main diagonal. For a experiment with Mx microphones, the upper limit is $M = Mx\ (Mx+1)/2$. The superscript, * represent the *normalized* distribution. This minimization scheme aims to match the *normalized* modeled intensity distribution S^*_{model} to the experimental intensity distribution S^*_{exp}. We are only interested in matching the shape (directivity) of the polar intensity distribution, and not so much its absolute value. Thus, the modeled and experimental intensities are normalized by their corresponding maximum value

$$S^*_{model}(\theta_m, \theta_n, A_k) = \frac{S_{model}(\theta_m, \theta_n, A_k)}{S_{model,\,max}} \qquad S^*_{exp} = \frac{S_{exp}(\theta_m, \theta_n)}{S_{exp,\,max}} \tag{3.25}$$

where $S_{exp,\,max}$ and $S_{model,\,max}$ denotes the maximum real-part of the cross spectra matrix for the experimental and model, respectively. A FORTRAN code was developed to postprocess the Vold-Kalman filtered tonal noise data. A schematic of the code is shown in Fig. 3.7. The minimization process of the above equation uses the Restarted Conjugate Gradient method of Shanno and Phua [55]. The Hankel Functions were determined from TOM algorithm 644 [56]. Once the wavepacket shaped is matched, the absolute levels are scaled to the appropriate amplitude.

3.3 Integration into Boundary Element Method (BEM)

The Boundary Element Method (BEM) solves the linearized acoustic problem with uniform inflow or non-uniform but potential free stream (low-Mach number approximation) [36]. A advantage of boundary elements method is that it often requires less computational resources than finite elements. This is because the method is a surface-described situation. Here, the source on a surface of a vibrating or radiating body is specified, and then the response of how the information is propagated out into the space is determined. Fig. 3.6 illustrates the classical setup of the boundary element method [57].

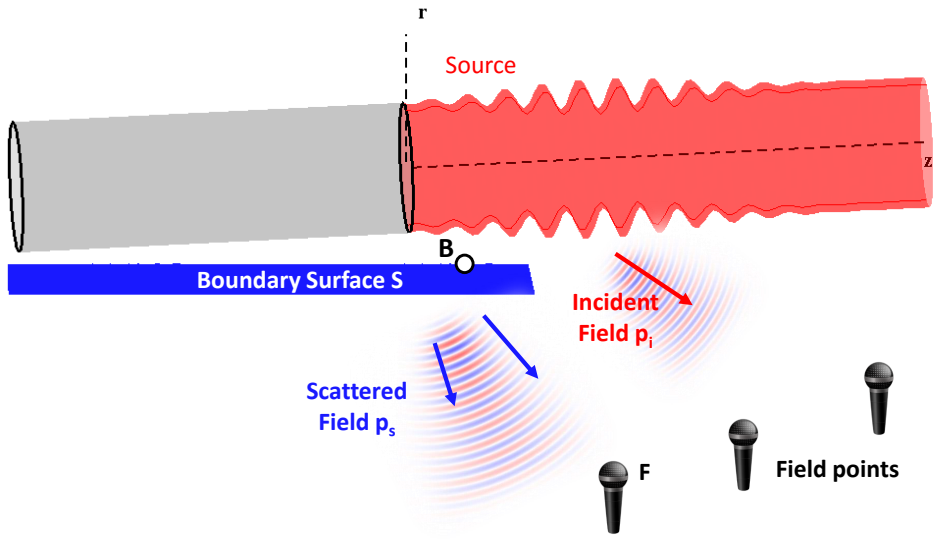

Figure 3.6: Setup of wavepacket as a radiating body with a boundary

The incident field comes from the modeled wavepacket source. A body is mathematically modeled by a collection of point sources on the surface. The coordinate of the boundary is B. We seek the solution of the scattered field, p_s, at the field point F were the sound is measured. Assuming a uniform flow, the boundary element method solves the Helmholtz's equation [58]. The pressure field in free space due to a point source is found from Helmholtz's equation with a Dirac delta function as the source on the surface B.

$$\nabla^2 p + k^2 p = -\delta(F - B) \tag{3.26}$$

where $k = \omega/a_\infty$ is the wave number, and p is the complex pressure in the frequency domain. We introduce the Green's function $G(F|B)$ as a solution due to a concentrated source at B. This function forms a fundamental solution to the partial differential equation such that

$$\nabla^2 G + k^2 = -\delta(F - B) \tag{3.27}$$

where

$$G = \frac{1}{4\pi r} e^{-ikr} \tag{3.28}$$

where r denotes the the distance from the field point F to the surface point B. Multiplying the fundamental solution by $\nabla^2 p$ or $k^2 p$ gives the symmetric form:

$$G(F|B)\nabla^2 p(F) - p(F)\nabla^2 G(F|B) = \delta(F - B)p(F) \tag{3.29}$$

Integrating over the the entire acoustic domain and using Green theorem to convert the volume integral into a surface integral

$$c(F)p(F) = \int_S \left[\frac{\partial p(B)}{\partial n} G(F|B) - p(B) \frac{\partial G(F|B)}{\partial n} \right] d^2 B + p_i \tag{3.30}$$

where p_i is the incident field, n are surface normal, S is the boundary of the surface, and integration of the far field boundary is zero (i.e. they don't reflect). Thus, the integral is only over the bounded surface. The variable $c(F)$ is a coefficient that scales the equation based on whether the observer is outside, on, or inside the boundary.

$$c(F) = \begin{cases} 1 & F \text{ in acoustic domain} \\ 1 - \int_S \frac{\partial}{\partial n}(\frac{1}{4\pi R}) dS & F \text{ on object surface} \\ 0 & F \text{ in object interior} \end{cases} \tag{3.31}$$

One of the most truly remarkable aspects of BEM is that the surface integral requires a mesh

of a surface rather than a solid volume. Thus, this formulation simplifies the labor required to mesh complex geometries. Typically, the boundary surface is discretize using triangular meshes with a resolution of 8 nodes per wavelength. Boundary element formulation give rise to dense matrices. This means that the storage requirements grows according to $O(N^2)$ for a system of N nodes. The BEM code developed by T.W. Wu was used for scattering predictions [59].

Program structure

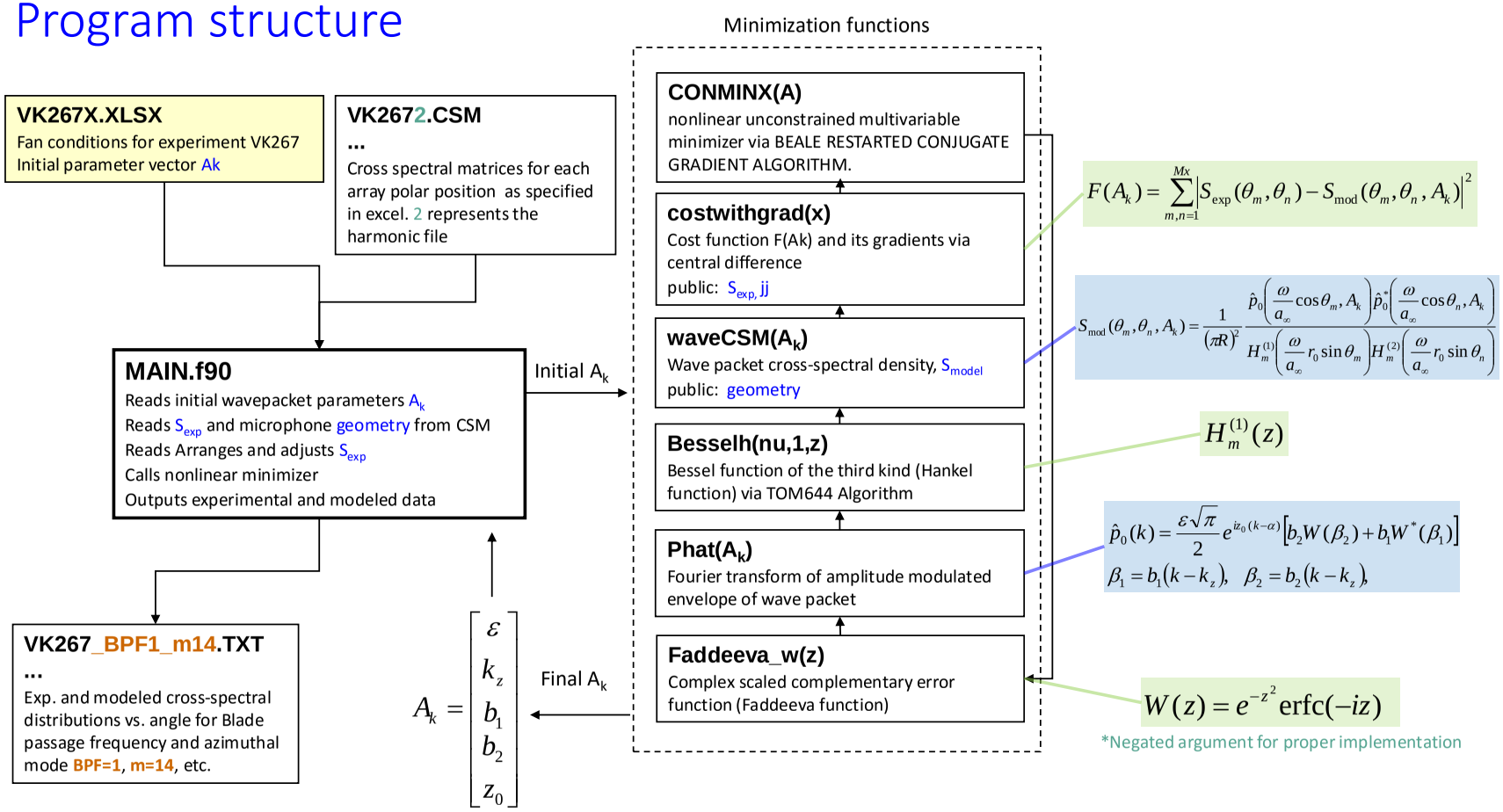

Figure 3.7: Program layout of wavepacket optimization routine

Chapter 4

Experimental Details

4.1 Ducted Fan Rig

The experimental effort entailed the design and construction of a small-scaled ducted fan rig that includes all the relevant components of the turbofan engine and simulates accurately the sound emission by the fan of such engines. The scale of the fan is approximately 1:38, based on a full-scale inlet diameter of 2.67 m (105 in.) [29]. The fan was designed to simulate the low fan pressure ratio (high bypass ratio) operation of a geared turbofan engine. Various design elements of the rotor and stators were extracted from published reports based on NASA/GE Source Diagnostic Test (SDT), particularly Refs. [22, 24, 25]. The rotor and stator counts were 14 and 24, respectively, giving a rotor-stator ratio of 0.58. The relatively low counts was selected for manufacturing considerations; however, having gained experience with the manufacturing process, higher counts will be possible in the future. The aerodynamic design process begins with non-negotiable characteristics that the compressor must meet as documented in Table 4.1. These specifications are constrained by the power capacity of the brushless motors.

Preliminary design and layout of the engine involves working first with simple one-dimensional mean-line analysis. A schematic for the mean line (one-dimensional) calculation stations is illustrated in Fig 4.1. Corresponding velocity triangles are drawn in the lower

Table 4.1: Design Point Specifications

Total Pressure ratio	FPR=1.15
Inlet Total Pressure	P_0=101325 Pa
Inlet Total Temperature	T_0= 273 K
Corrected Mass Flow	$\dot{m}_c$ = .3307 kg/s
Physical speed	Ω =57,000 rpm
Rotor casing diameter	70 mm
Blade count	14
Rotor count	24
Exit Mach number	M_{exit} = 0.3

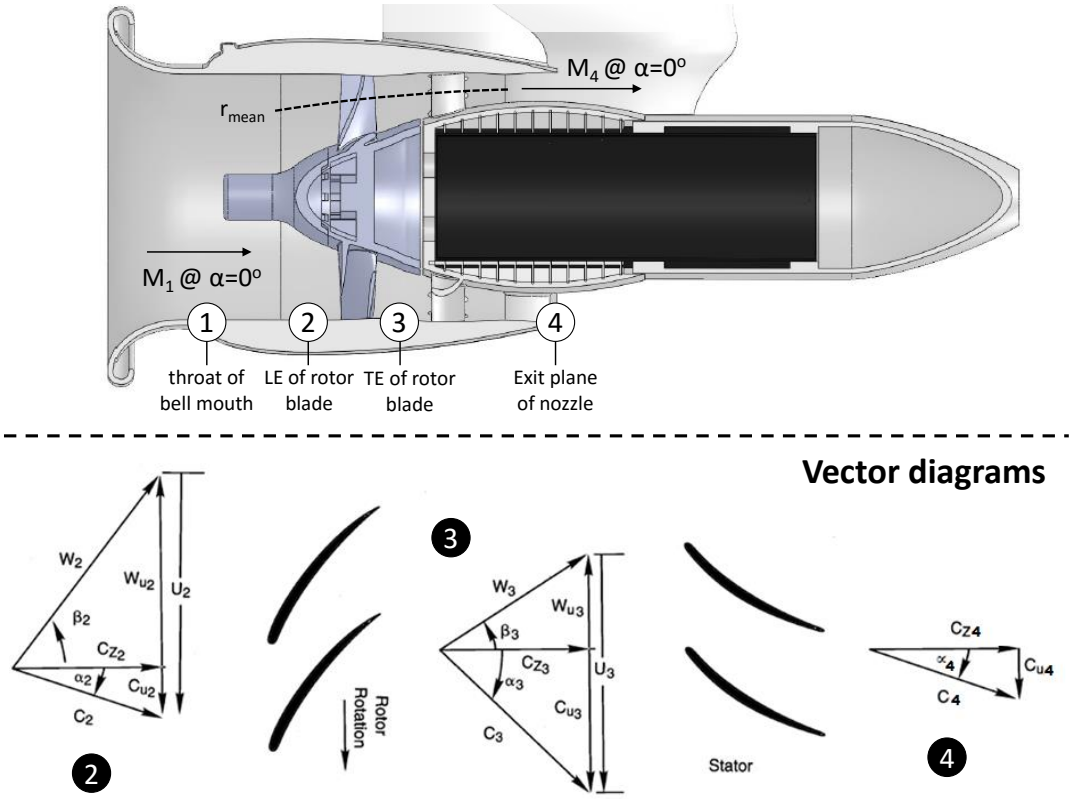

Figure 4.1: Stations locations of a ducted fan.

image of Fig. 4.1. Before the calculations can begin, the inlet and exit conditions of the engine are determined. This inflow and outflow conditions will contain the properties and overall design of the compressor. The mean radius (the average radius between the hub and casing) is used in the calculations to determine the tangential blade speed. MATLAB, in conjunction with mean line relations assisted in the determination of the velocity triangles,

thermodynamic and aerodynamics properties along the flow path of the engine. Loss coefficients are included in the calculation to relate the fluid turning angles to the stagnation pressure loss due to friction.

The meanline methodology neglected radial variations in the flow through the fan and determined flow properties only at the pitchline. However, to design a efficient fan, the determination of the various air velocities and flow angles from hub to tip at the inlet and outlet of the fan are required. The determination of the casing and hub quantities is obtained from force balance of the radial acceleration of the fluid and the radial pressure force (radial equilibrium). Here a constant reaction design was utilized.

Following the determination of the velocity triangles along the fan span, the design process proceeded to the design of the blade geometry. An airfoil camber line is established using NACA-65 series correlations [60]. The airfoil is optimized so that the flow enters and exits the blade passage smoothly. A schematic of the velocity triangle and stacking procedure is depicted in Fig. 4.2.

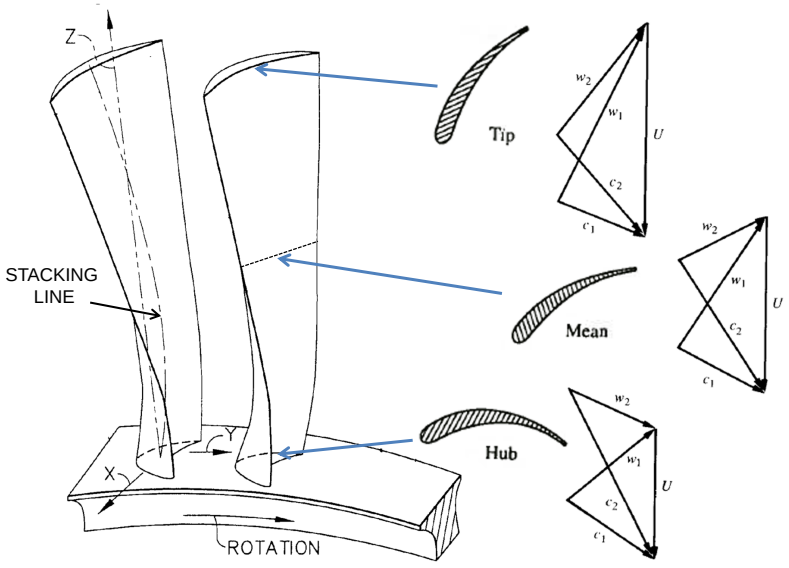

Figure 4.2: Vector diagram and blade profiles at hub, meanline, and tip. The axial velocity, c_z is independent of radius. Figure adapted from Mechanics and Thermodynamics of Propulsion (pg. 334).

Lastly, ANSYS FLUENT was used to verify and refine the mean line analysis model. A flow field simulation was performed using a steady (relative to rotor) Reynolds-averaged Navier-Stokes (RANS) unstructured grid solver. Turbulence was represented by a two equation SST k-omega model. At the inlet, the total pressure, total temperature and flow angles were prescribed. The static pressure is specified at the mid-span of the exit of the domain, and the pressure values at all other radial locations were obtained by integrating the radial equilibrium equation. Periodicity is enforced along the outer boundaries. No-slip boundary conditions are implemented at the hub and tip end walls and along the airfoil surfaces. Simulation results are illustrated in Fig. 4.3. These computations substantiate efficient flow turning free of separation or stall, and proper blade stacking.

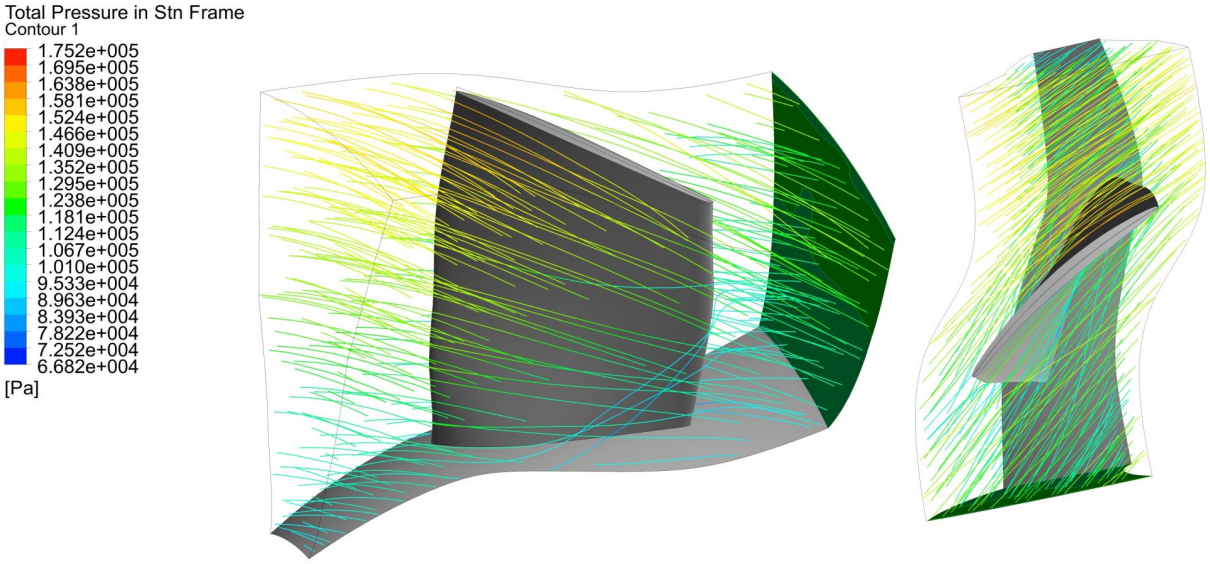

Figure 4.3: Fluent CFD simulation of the rotor blade row.

The final rotor design is illustrated in Fig. 4.4. The rotor were manufactured by ProtoCAM using lost wax casting. Investment casting, also called "lost wax casting", uses a 3D printed wax pattern with $\pm$ 0.127 mm tolerance, and a ceramic cast wax pattern. The wax is then burnout for casting. The prototype is made using Aluminum 356. Several days of precision work are needed to mirror-polish the surfaces of the rotor. Using progressively finer diamond pastes, the part is manually polished and edges chamfered. The nacelle (including

the stators) were manufactured from plastic material using stereolithography. A bell-mouth entry for the nacelle was chosen to prevent flow separation in the static test environment. The nacelle features pressure ports for measuring the inlet static pressure and the outlet total pressure. The aerodynamic performance was assessed by these pressure measurements.

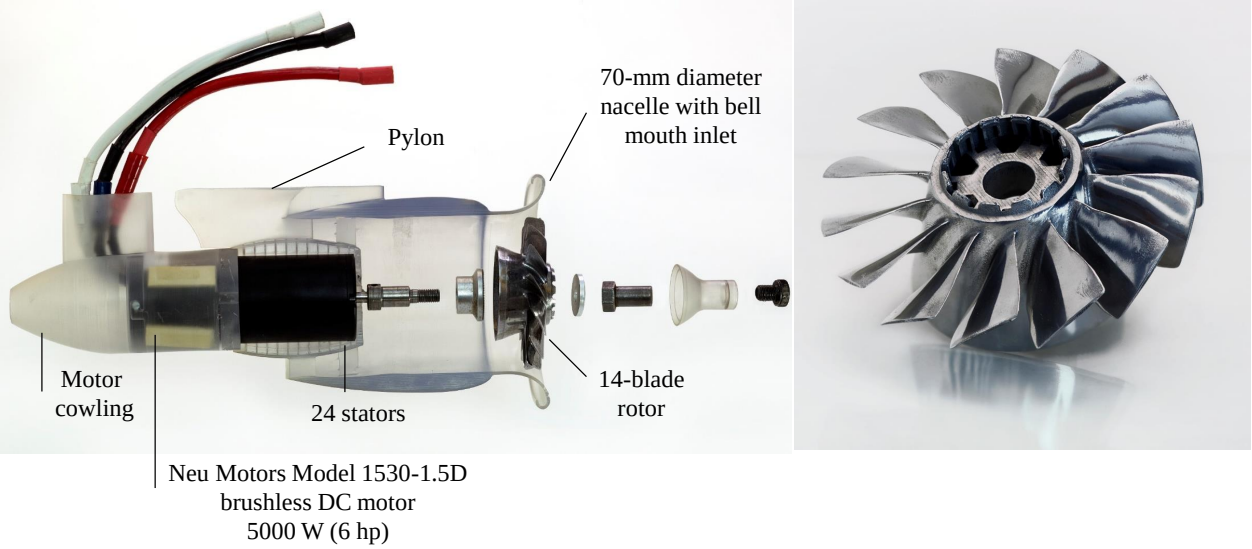

Figure 4.4: Overview of the ducted fan design. a) cross-sectional view; b) picture of the 3D printed rotor.

The rotor was powered by a high-performance brushless DC motor (Neu Motors, Model 1530-1.5D) which can attain a surge power of 5.0 kW. The motor has an RPM/Volt (Kv) rating of 1350, meaning that it can spin at an RPM of 60,000 at the maximum rated voltage of 44 V. The motor was controlled using Castle Creations Phoenix 160 Amp electronic speed controller (ESC). Power to the speed controller was supplied by two 6S (22.2 V) lithium-ion polymer (Lipo) batteries connected in series with a discharge rate of 30c and a capacity of 8300 mAh. The speed controller was controlled by a Spektrum AR6200 DSM2 six-channel receiver connected wirelessly to a Spektrum DX7 2.4 GHz seven-channel radio. The receiver was powered by a Castle Creations battery eliminator circuit (BEC PRO). The power components and their installation are depicted in Fig. 4.5.

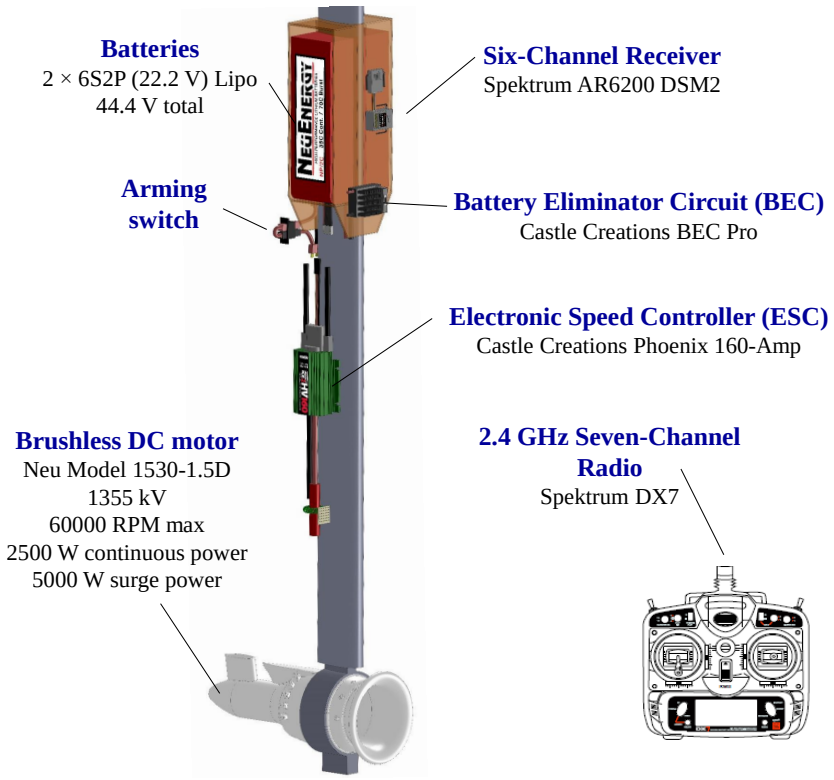

Figure 4.5: Principal power components and their installation.

4.1.1 Shield Apparatus

The airframe shielding surface is approximated as a flat plate. The shield consists of a 1.5 mm thick by 610 mm (24 inches) wide rectangular plate made out of carbon fiber. The nominal chord of the shield is 102 mm (4 inches), but the total axial length of the shielding surface can be changed in 25.4 mm increments via the addition of carbon fiber strips. In addition, the distance between the trailing edge of the shield and the rotor axis is adjustable. The shield was mounted horizontally, and a transverse mechanism permits changes in the distance of the rotor from the surface. Table 4.2 summarizes the salient parameters of the shield.

During experimentation, the insertion of a strips to lengthen the shield chord corresponded to a shift downstream of the shield trailing edge by 1 inch. This procedure ensures that the shielding surface starts at the same upstream location. The shield trailing edge

Table 4.2: Rectangular Shield Specifications

Height of nozzle centerline above shield	65 mm
Nominal Shielding length	101.6 mm
Shielding span	610 mm
Fan Axis (from shield plane of symmetry)	0 mm
X_{TE} (25.4 mm increments)	$0 - 78$ mm

started at the nozzle exit plane and moved downstream. The left image in Fig. 4.6 presents the dimensions of shield with insert-able strips and the right picture shows the shield apparatus used in the experiments.

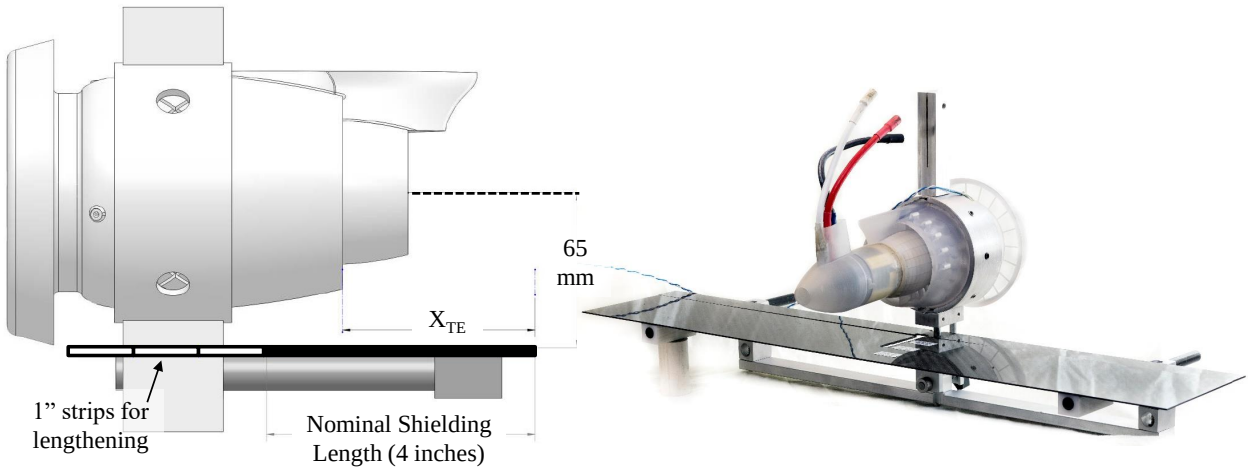

Figure 4.6: Schematic (left) and picture (right) of airframe shielding rig with insert-able strips for lengthening of the chord.

4.2 Test Facility

Acoustic measurements were conducted inside an anechoic chamber at UC Irvine's Aeroacoustics Facility, depicted in Figs. 4.7. Twenty-three 3.2-mm condenser microphones (Brüel & Kjaer, Model 4138) with a frequency response of 140 kHz were used to survey the near and far-field acoustics. For the far-field surveys, the microphones were all arranged on the downward arm (azimuth angle $\phi = 0°$). The polar angle θ is defined from the center of the fan exit plane relative to the downstream rotor axis, as shown in Fig. 4.7. Its approximate

range was 48° to 84°. This setup emphasizes aft-emitted turbofan noise. The minimum microphone-to-nacelle distance was 0.8 m, or 11.4 fan diameters. This places the microphones in the acoustic far field for the frequency range relevant to aircraft noise (i.e., higher than 50 Hz at full scale).

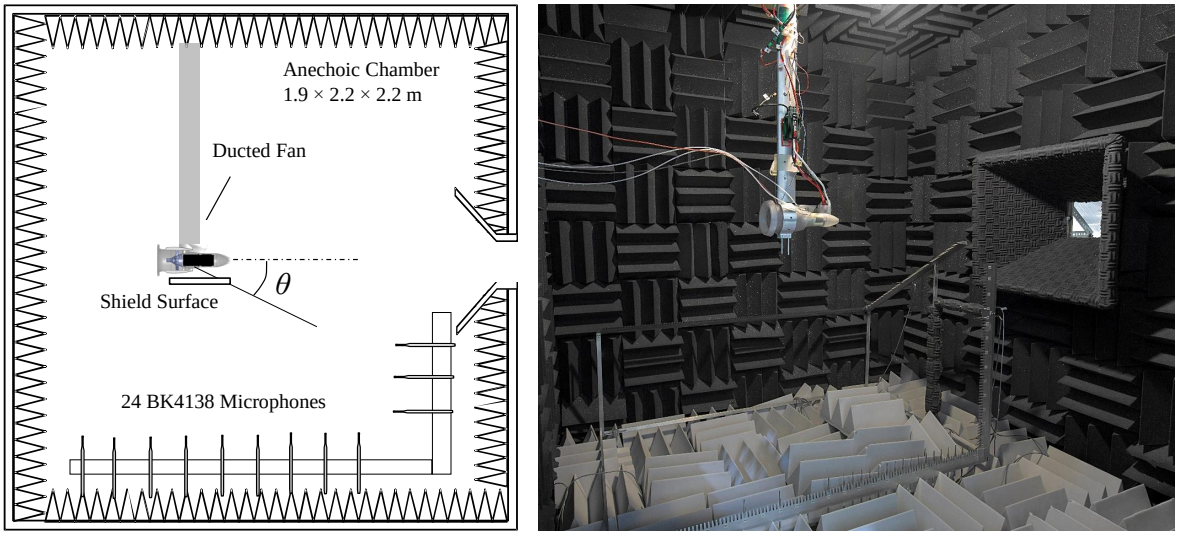

Figure 4.7: Schematic of anechoic chamber and microphone array (left). Picture inside anechoic showing downward arm holding 24 microphones (right).

The microphones were connected, in groups of four, to six conditioning amplifiers (Brüel & Kjaer, Model 2690-A-0S4). The 23 outputs of the amplifiers were sampled simultaneously, at 250 kHz per channel, by three eight-channel multi-function data acquisition boards (National Instruments PCI-6143). The 24th output channel was assigned to the RPM sensor. National Instruments LabView software was used to acquire the signals. Nominal microphone sensitivity was 100 mV/Pa. The temperature and humidity inside the anechoic chamber were recorded to enable computation of the atmospheric absorption.

The sampling rate for each microphone was 250000 samples/second, and the number of samples for each test run was 262144 per microphone. The narrowband sound pressure level spectra were computed with a 8192-point Fast Fourier Transform, giving a frequency resolution of 30.5 Hz. The SPL narrowband spectra were corrected for actuator response, free-field correction, and atmospheric absorption, resulting into lossless spectra. The full-scale, 1/3-

octave spectrum was calculated from the lossless narrowband spectrum after dividing the frequency vector by the scale factor of 38. In addition, the overall sound pressure level (OASPL) was calculated from the lossless SPL spectrum. The lab-scale SPL narrowband spectrum, lab-scale OASPL, and full-scale 1/3-octave spectrum, are referenced to a distance of 305 mm (12 in.) from the exit of the ducted fan. Time series analysis did not include frequency-based corrections.

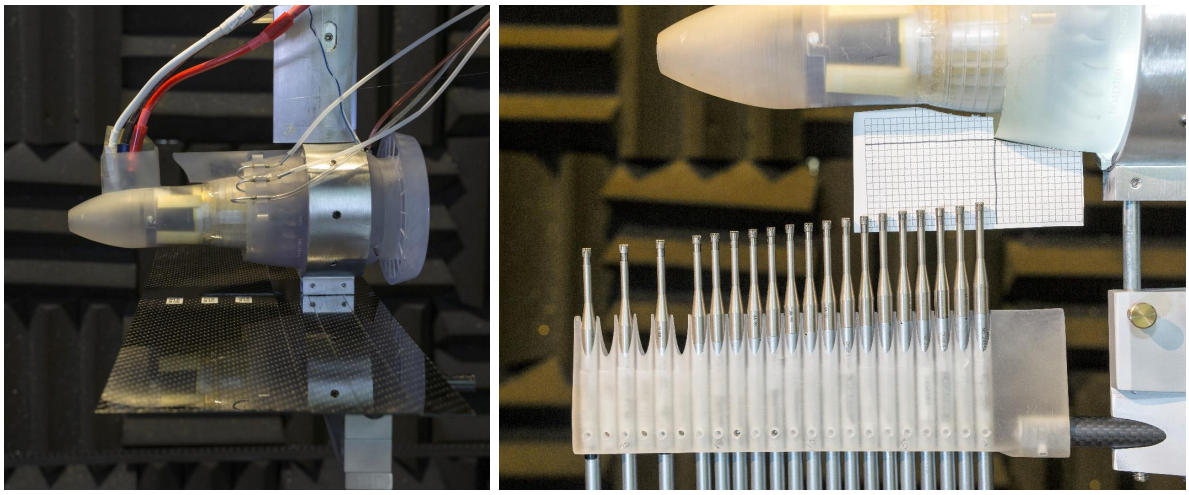

Figure 4.8: Installation of fully extended (addition of all strips) shielding surface in anechoic chamber (left). Attachment of nearfield microphone array to fan rig (right).

To properly model oscillations of the form of "wavepackets" on cylindrical radiator surface surrounding the engine requires surveys in the acoustic near-field. This is because a lot of information is lost when measurements are taken far away from the source. Acquiring pressure signals just outside the mixing layer captures the evanescent (exponentially decaying) pressure field associated with wavepackets. This allows us to accurately infer properties of the source, and propagate sound to the far-field to determine whether the pressure field is consistent with a wavepacket. This observation is essential to establish quantitative cause-and-effect relationships between the dynamics of modal structures and far field sound.

Near-field pressure measurements were acquired using 19 microphones mounted to a horizontal linear array arm printed using Stereolithography. The arm was supported by a carbon fiber rod which allow adjustment of the axial position and is secured to the underside

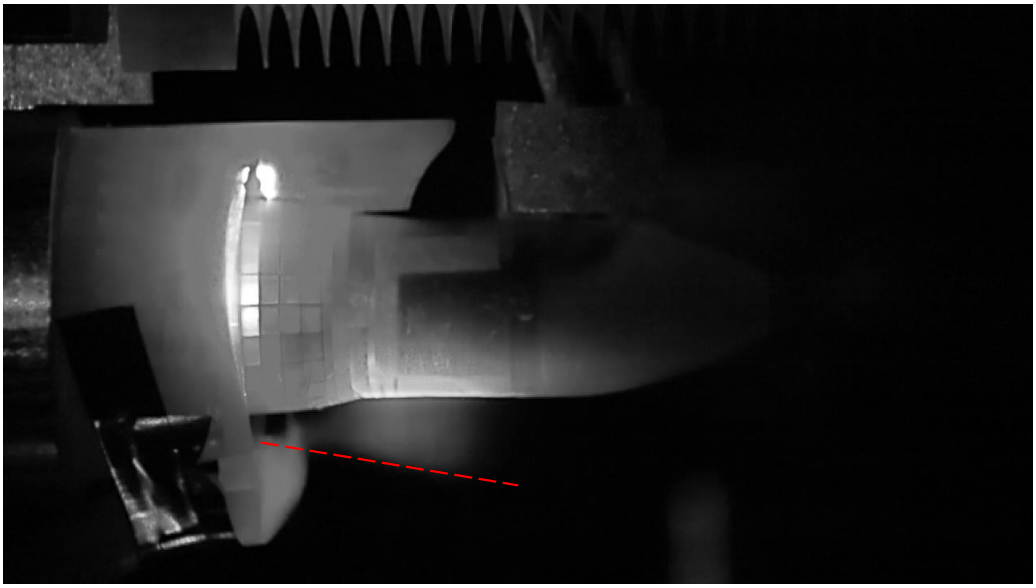

Figure 4.9: Frame grab of video of flow visualization using smoke and a HeNe laser sheet for illumination.

of the ducted fan rig. A photo of the installed inside the anechoic chamber is shown in Fig. 4.8. Microphones are positioned directly along the axis of the jet in the downward azimuthal direction with a microphone spreading angle (the half-angle of the cone) of 7 deg. This angle was determined so that it was slightly steeper than the visual jet spreading angle obtained from laser sheet flow-visualization experiments, see Fig. 4.9. Minimum microphone spacing is 7.5 mm, which corresponds to theoretically resolving two wavelengths of the 2× BPF mode. The whole array can be shifted in the axial direction, with the first microphone spaced 6.35 mm to 25.4 mm axially from the nozzle exit. Microphone positions were determined from photogrammetry. The radius from the nozzle centerline to microphone tip varied in the range of $.86 \leq r/D \leq 1.14$.

Instantaneous rotor speed was determined by detection of the pulsation of the electrical load from the electronic speed controller (ESC) to the motor, using a ferrite toroid induction sensor as shown in Fig. 4.10. The ESC sends a pulse-width modulated (PWM) waveform to the motor. The pulses are emitted at the commutation frequency, f_c , which is the rate of switching of the polarity of the magnets to maintain the motor rotation. The pulse width

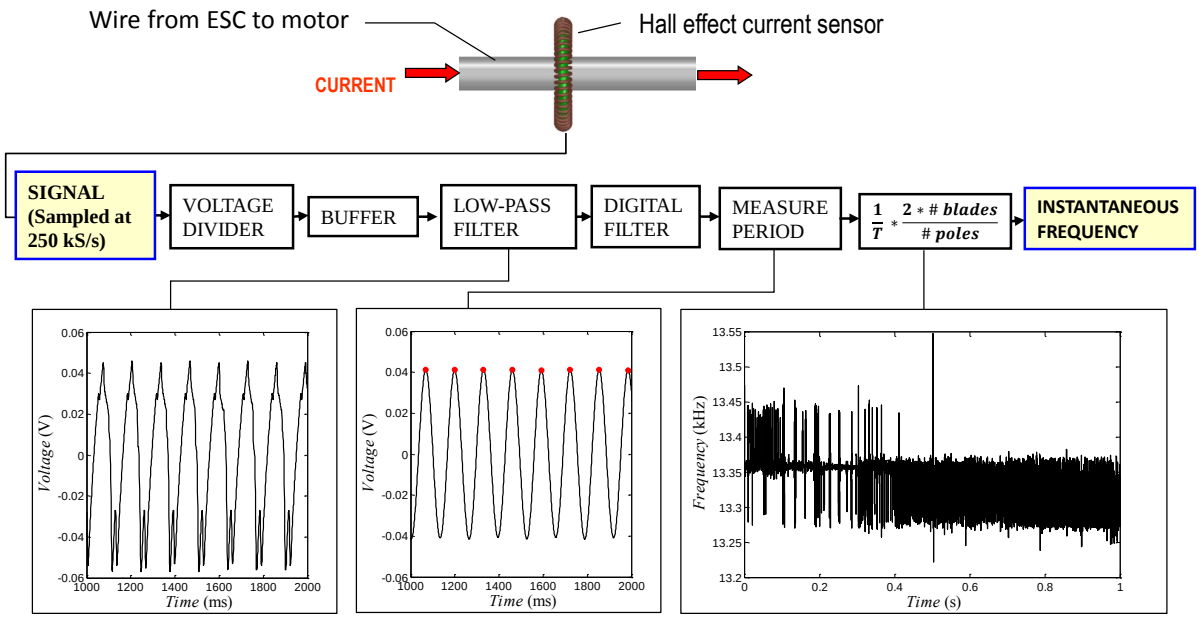

Figure 4.10: Flowchart of RPM measurement and phasor frequency determination process.

controls the power to the motor. The raw signal voltage from the current sensor is reduced to levels tolerated by the data acquisition system using a voltage divider circuit, and is then fed to a low-pass filter and through a buffer. The low-pass filter attenuates the fast switching PWM component of the signal, while the buffer prevents unacceptable loading of the voltage divider circuit by the low-pass filter circuit. Once digitized, a more aggressive high order low-pass Chebyshev filter is applied to cutoff frequency higher than the commutation frequency. The period of the signal is then computed using the time lag between the peaks as shown in the middle image in Fig. 4.10. Conversion from the commutation period T to instantaneous frequency (BPF) is given by the formula $f(t) = 2N_b/(TN_p)$, where N_p is the number of magnetic poles in the motor and N_b is the number of blades. The Neu 1530 motor has four poles, and the rotor has 14 blades. This method enabled the determination of a precise phase accurate frequency for each acoustic test run (the RPM signal was collected simultaneously with the microphone signals).

A representative time history of the motor frequency is plotted in Fig. 4.11. The low-pass filtered signal of the instantaneous frequency is depicted by the red line. It is observed

that the shaft frequency fluctuates at a high frequency over a slowly varying RPM value that slows during the experiment. A key to the successful implementation of the Vold-Kalman filter is the precise knowledge of the structure to be tracked. The non-filtered (black) signal serves as a very accurate RPM input to the Vold-Kalman filter, such that the tracking filter will follow the peaks of the tones (orders) instead of tracking the wrong frequency.

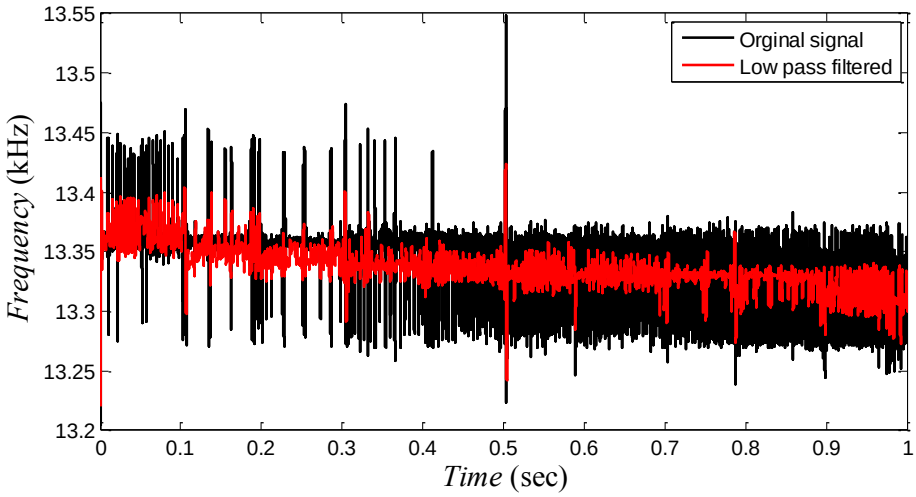

Figure 4.11: Frequency time trace during a typical test run (262144 samples). The red line represents the low-pass filtered component of the RPM sensor output. Rotor speed indicates an average RPM near 57,000 (13.33 kHz) The rotor slows down slightly during the experiment.

4.3 Algorithm of the Vold-Kalman Filter

The Vold-Kalman filter, introduced by Vold and Leuridan [61], extracts the non-stationary periodic components from a signal using a known frequency vector (e.g., rotor RPM). Several additional works describe its functionality and applications [33, 62, 63]. The filter is formulated as a least-squares problem and can be solved as a linear system. Similar to the Kalman filter, which is based on the process/ measurement equations (i.e. state-space model) and a global estimator (orthogonal projection) [64] , the Vold-Kalman filter is based on the structural/data equations and a global estimator (least squares). Only the second-generation

multi-order Vold-Kalman filter will be reviewed and applied in this paper.

4.3.1 Data Equation

Engineers are interested in signals that exhibit periodicity, i.e., events that occur repeatedly in time with a prescribed period [65]. This may be a result of an oscillating spring/membrane, mechanical systems, or the sound pressure generated by the periodic volume displacement of air by the blades of a propeller. These are deterministic processes. Broadband noise, in contrast, is typically generated by a more or less stochastic process. Such noise sources include turbulence, vortex shedding, interaction effects, and represent everything that is uncorrelated with the RPM sensor signal. An arbitrary real-valued signal can be modeled as a summation of a deterministic periodic part consisting of K sine waves with varying phase and amplitude, plus a stochastic part of uncorrelated broadband noise $\eta(t)$. This sinusoidal plus noise formulation is called the Wold decomposition [66]. The total measured signal $y(t)$ is of the form:

$$y(t) = \sum_{k=1}^{K} x_k(t) \exp\left(2\pi k i \int_0^t f(t)dt\right) + \eta(t) \tag{4.1}$$

Here the deterministic periodic signal is written in complex polar coordinates, with k indicating the order extracted. The exponential term is called the complex phasor and represents a constant-amplitude, frequency-modulated carrier wave. The instantaneous frequency $f(t)$ of the carrier wave is determined by the tachometer or RPM sensor. The slowly time-varying (complex) amplitude $x_k(t)$ modulates the carrier wave (i.e. the complex phasor). The objective of the Vold-Kalman algorithm is to minimize the sum of squares of the errors (e.g., broadband signal) for a number of harmonics by properly choosing the complex envelope $x_k(t)$. Storing the complex phasor on the diagonals of the matrix C_k, the above

expression takes the compact form:

$$y(t) - \sum_{k=1}^{K} C_k x_k(t) = \eta(t) \tag{4.2}$$

4.3.2 Structural Equation

The structural equation imposes smoothness on the complex envelope $x_k(t)$ by means of a backward finite-difference sequence. This is accomplished by minimizing the error $\varepsilon(t)$ made in the smoothness of the envelope, where the smoothness is represented by a low-order polynomial. The polynomial order designates the number of the filter poles. The equations for 1-,2-, and 3- pole filter coefficients are found by the Pascal triangle:

$$\nabla x_k[n] = x_k[n] - x_k[n-1] \;=\; \varepsilon_k[n] \tag{4.3a}$$

$$\nabla^2 x_k[n] = x_k[n] - 2x_k[n-1] + x_k[n-2] \;=\; \varepsilon_k[n] \tag{4.3b}$$

$$\nabla^3 x_k[n] = x_k[n] - 3x_k[n-1] + 3x_k[n-2] - x_k[n-3] \;=\; \varepsilon_k[n] \tag{4.3c}$$

Assuming a second-order difference, the system of structural equations with the complex envelope x_k for order k as the unknown takes the form of a matrix equation:

$$\begin{bmatrix} 1 & -2 & 1 & 0 & \cdots & & & \\ 0 & 1 & -2 & 1 & 0 & \cdots & & \\ \vdots & 0 & 1 & -2 & 1 & 0 & \cdots & \\ & \vdots & 0 & \ddots & \ddots & \ddots & 0 & \cdots \\ & & & & 1 & -2 & 1 & 0 \\ 0 & 0 & 0 & 0 & & 1 & -2 & 1 \end{bmatrix} \begin{bmatrix} x_k[1] \\ x_k[2] \\ x_k[3] \\ \vdots \\ \\ \\ \\ x_k[n] \end{bmatrix} = \begin{bmatrix} \varepsilon_k[3] \\ \varepsilon_k[4] \\ \varepsilon_k[5] \\ \vdots \\ \\ \\ \\ \varepsilon_k[n] \end{bmatrix} \tag{4.4}$$

Notice that the errors $\varepsilon_k[1]$ and $\varepsilon_k[2]$ cannot be determined since the stencil contains points outside the domain of the complex envelope. For an order k, the matrix on the left hand side is a sparse band matrix (tridiagonal matrix in this example) with dimensions of $(N-p)\times N$, p being the number of the filter poles ($p = 2$ in this example). In compact notation the matrix reads as:

$$Ax_k = \varepsilon_k \tag{4.5}$$

4.3.3 The Least-Squares Problem

The set of data and structural equations creates an over-determined linear system for the desired waveform amplitude $x_k(t)$. No exact solution exists, nor does a two-sided inverse. A pseudo inverse can be obtained using ordinary least-squares, QR decomposition, or the singular value decomposition (SVD). Normally, the Vold-Kalman filter uses least squares because of speed. Here, the objective is to estimate the non-random complex envelope $x_k(t)$ by minimizing the square of the errors from the data and structural equations due to non-periodic components and envelope roughness, respectively. Introducing a scalar weighing factor r, a cost function is formulated to find the optimum solution in the sense of least squares:

$$J(x) = \sum_{k=1}^{K} r_k^2 \varepsilon_k^H \varepsilon_k + \eta^H \eta \tag{4.6}$$

The purpose of the weighting factor is to slant the prominence of the structural equation with that of the data equation. For instance, if r is large the cost function is strongly influenced by the structural equation yielding a very smooth modulator. The value of r also determines the bandwidth of the filter. Large r results in very small bandwidth and vice-versa. The minimum is found by evaluating the derivative $dJ/dx^H = 0$, and rearranging to a more familiar “normal" least-squares form:

$$\Big(r^2 A^T A + I\Big)x_k = C_k^H y \tag{4.7}$$

The equivalent “second-derivative" minimization requirement for a multidimensional problem is that the symmetric hessian matrix (r^2A^TA+I) be positive definite. It can be shown that r^2A^TA+I is positive semi-definite, and adding the identity matrix turns it positive definite. This property ensures that the matrix on the left hand side is invertible. Moreover, the matrix r^2A^TA+I is independent of the tracked frequency in C_k and the signal y. This allows for the matrix to be reused for tracking of orders with different phasors, reducing the extensive computational memory resource required. With regards to rotor noise separation, no crossing orders exist. Efficient Vold-Kalman filtering is accomplished using multi-order tracking through a single order scheme by simply changing the terms in the phasor term on the right hand side of Eq. 7 for different harmonics, and solving the respective linear system independently. For instance, given the high sampling rate necessitated by small scale acoustical experiments, and the multiple orders tracked, the single order scheme drastically shrinks the matrix dimension from 1,750,000 to solving 7 decoupled matrices with dimension of 250,000. The expanded version of Eq. 7 for a two-pole Vold-Kalman filter and order k has the form:

$$\begin{bmatrix} r+1 & -2r & r & 0 & \cdots & & & \\ -2r & 5r+1 & -4r & r & 0 & \cdots & & \\ \vdots & r & -4r & 6r+1 & -4r & 0 & \cdots & \\ 0 & 0 & 0 & \ddots & \ddots & \ddots & \ddots & \cdots \end{bmatrix} \begin{bmatrix} x_k[1] \\ x_k[2] \\ x_k[3] \\ \vdots \\ \\ \\ x_k[n] \end{bmatrix} = \begin{bmatrix} C_k^H y[1] \\ C_k^H y[2] \\ C_k^H y[3] \\ \vdots \\ \\ \\ C_k^H y[n] \end{bmatrix} \tag{4.8}$$

The linear system is very large, sparse, banded, and positive definite. This implies that the solution can be obtained efficiently by using Cholesky factorization. In the process of determining a solution the matrix on the right hand side undergoes zero-phase low-pass filtering. The frequency response characteristic, defined by a -3 dB drop in magnitude, is controlled by the value of the weighting coefficient r. Fig. 4.12 depicts the bandwidth of the

filter with varying pole counts and a weighting factor. A higher weighting factor results in a smaller bandwidth and a smoother varying amplitude as shown in the figure. However, the value of r should not overshadow the effect of adding unity to the main diagonal. Typical Vold-Kalman order tracking codes utilize a two-pole filter.

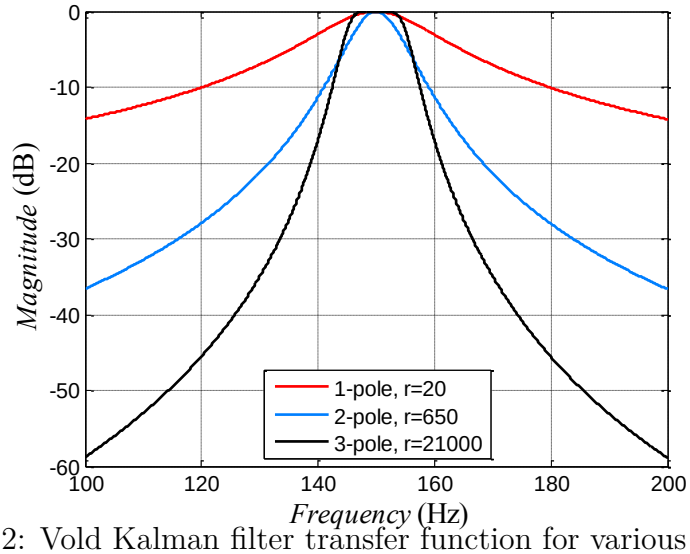

Figure 4.12: Vold Kalman filter transfer function for various pole counts.

4.3.4 Comparison With Other Transforms

There are some similarities between the Vold-Kalman filter and other non-stationary time-frequency methods such as wavelets, chirplets, Hilbert transform, and Hilbert Huang transform [67]. Here we discuss commonalities with the Hilbert transform since wavelets are a subset of the Hilbert transform. The main advantage of the finite impulse response filter-Hilbert method over wavelet convolution is that the filter-Hilbert method allows more control over the frequency characteristic of the filter, whereas the filter shape of a Morlet wavelet or chirplet is always Gaussian [68]. On the other hand, the Hilbert-Huang transform is a way to decompose a complex signal into its basis time series (intrinsic mode function), to which the Hilbert transform can be applied [69].

A complex sinusoidal signal is defined by its amplitude and phase. It can be represented using Euler's formula: $a(t)e^{i2\pi ft}$. Here $a(t)$ is the time varying amplitude and the exponential

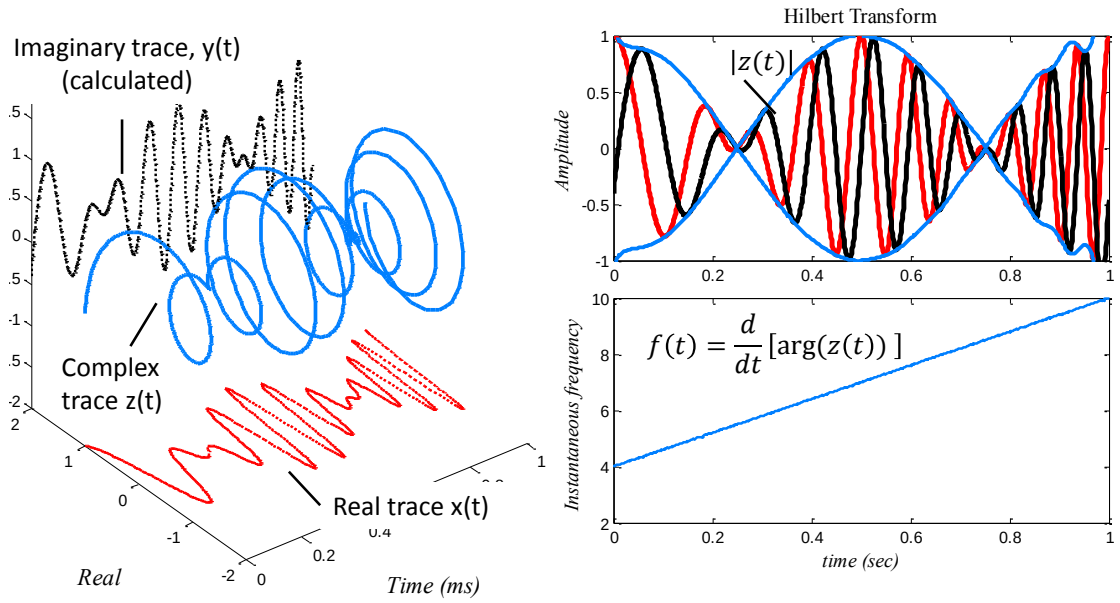

Figure 4.13: The Hilbert transform in complex space-time. The analytic signal in complex space is projected onto the real axis to form the signal. Projection onto the imaginary axis (quadrature) shifts the phase of the real signal by 90°. This complex signal can be written as a complex phasor with amplitude and phase: $a(t)e^{i2\pi ft}$.

represents the oscillation. This notation can be explained as a vector (phasor) at the origin of the complex plane having a length $a(t)$ and angular position $2\pi ft$. This representation is useful for narrow-band signals, where $a(t)$ is usually "slow" compared to the signal temporal variations. The signal can be represented in a three-dimensional space as depicted in Fig. 4.13. In this complex space-time the real value signal $x(t)$ measured by a transducer is confined to the real plane, and $y(t)$ is the Hilbert transform of $x(t)$ and is confined to the imaginary axis. When $x(t)$ and $y(t)$ are added vectorially, the result is a complex analytic trace $z(t) = x(t) + iy(t)$, in the shape of a helical spiral extending along the time axis [70]. Analytic means that the complex signal satisfies the Cauchy-Riemann conditions, that is, the derivative of $z(t)$ is path-independent and unique. The reason for converting the real signal into a complex trace is because the instantaneous amplitude and frequency can be calculated by taking the magnitude and argument of $z(t)$, as shown in the right image of Fig. 4.13. The real-valued signal of the Vold-Kalman filter is analogous to the filtered real-valued signal $x(t)$ in the Hilbert transform [33]. However, the phase of the

signal is computed from the tachometer signal rather than computing the mapping on the imaginary plane. Since a phase-accurate estimate of the instantaneous frequency is obtained directly from the tachometer, the complex phasor is already known. No unwrapping of the phase (revolute) and application of a Savitzky-Golay filter, or conjugate multiplication of adjacent complex samples ($\arg\{z[n]z^*[n+1]\}$) are required to compute the instantaneous frequency [70]. Thus, the Vold-Kalman filter only requires the linear estimation of the complex envelope x_k (analogous to $|z(t)|$) which is generated by the structural equation rather than the signal itself as in the Hilbert transform. Just like in wavelets, the Vold-Kalman filter is a subset of the more general Hilbert transform were information about the signal phase is obtained a priori.

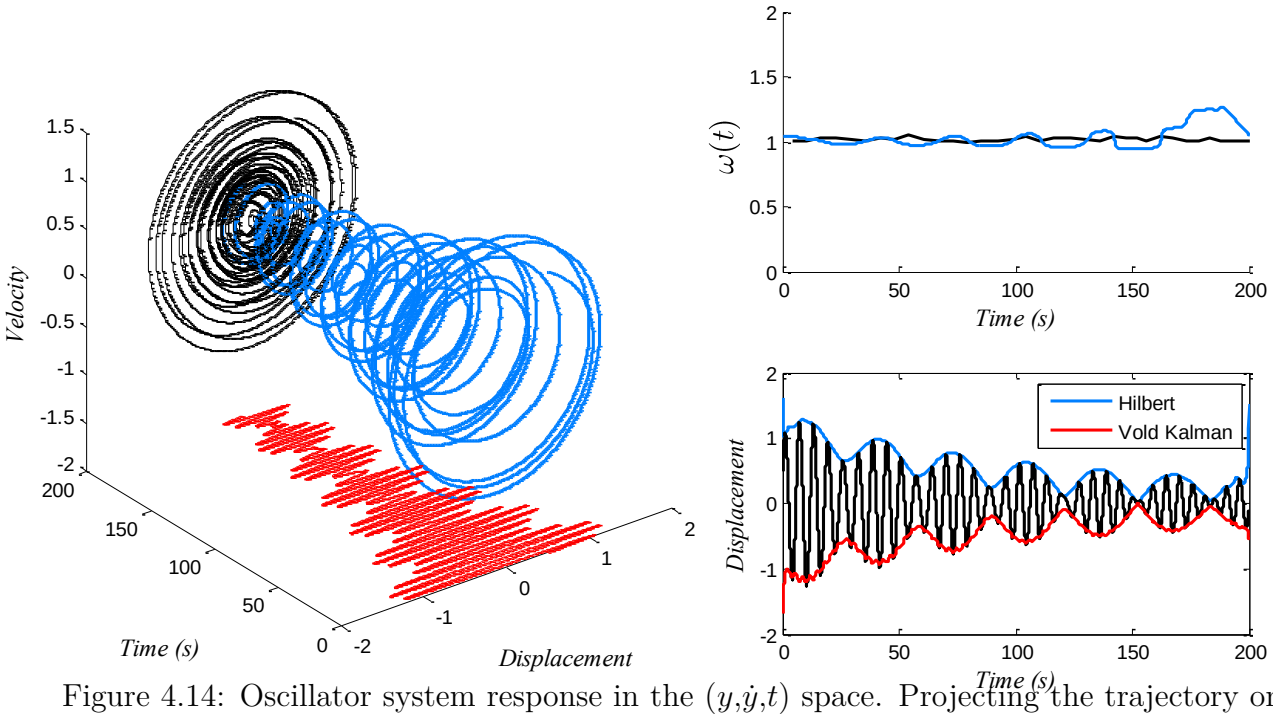

Figure 4.14: Oscillator system response in the (y,$\dot{y}$,t) space. Projecting the trajectory onto the displacement time axis gives the measured signal. Mapping the curve to space and velocity gives the phase portrait.

In Fig. 4.14, a representative solution for a forced linear oscillator described by the second-order nonautonomous differential equation $\ddot{y}+2\zeta\dot{y}+y = f\cos(\omega t)$ is graphed. $y, t, \zeta, f,$ and ω are the displacement, time, damping ratio, excitation amplitude, and excitation frequency, respectively. Projecting the trajectory onto the displacement time axis gives the

measured signal. Mapping the curve to space and velocity gives the phase portrait. White noise was added to the simulated solution. The stationary system is driven near the resonance frequency producing beats. Two times scales are present, an exponentially decaying envelope, and the oscillation corresponding to the natural frequency of the system. The exponential decay is represented by the trajectory inward spiral toward the origin. The linearity of the system implies a constant instantaneous frequency, as illustrated in the right image of Fig. 4.14. The oscillations are periodic, deterministic, and are modeled by a composition of a small number of monocomponent signals:

$$y(t) = \sum_{k=1}^{K} x_k(t) \exp\left(2\pi k i \int_0^t f(t)dt\right) \tag{4.9}$$

Non-correlated signals are manifested in the broadband noise term, $\eta(t)$. Here only one order exists, allowing effortless calculation of the complex envelope for both methods; if not, the results of the Hilbert transform are difficult to interpret when the data contain a range of frequencies and filtering or decomposition of the raw signal is required. To capture similar details to the Hilbert transform the Vold-Kalman bandwidth must be tuned. There are several techniques for the estimation of the narrowband signal frequency bandwidth of the Hilbert transform. Nevertheless, when we examine the average variance of the frequency excursion of the signal around the mean value, the average spectrum bandwidth is:

$$\sigma_{bw}^2 = \int_0^\infty (\omega - \overline{\omega})^2 S(\omega) d\omega = (\overline{\omega^2} - \overline{\omega}^2) + \overline{\dot{A}^2} \tag{4.10}$$

where ω, $S(w)$, A are the angular frequency, power spectrum, and amplitude of the signal ($A = |z(t)|$). The overbars represent time averages. The equation was obtained from Parseval's theorem and indicates that the average bandwidth is equal to the mean square value of the rate of the amplitude variation plus the mean square value of the deviation from the baseband frequency [70, 71]. Using a frequency vector at the natural frequency, the Vold-Kalman filter gives the envelope in red. Alternatively, the filter-Hilbert transform

computed similar results as depicted in blue. As noted earlier for the Hilbert transform, the signal phase was derived from the data rather than a tachometer.

Even though the real signal (red) is the same, the trajectory of the integral curve (Fig. 4.14) does not necessarily match the analytic trace $z(t)$ (Fig. 4.13), especially for non-linear systems. The addition of a non-linear cubic term y^3 to the simple harmonic oscillator, leading to the Duffing oscillator, dramatically changes the picture. Typically, the phase portrait becomes more distorted, generating sharp peaks and troughs in the time series. Additionally, a Duffing oscillator exhibits time variations in its natural frequency [70, 72]. In other words, the increased stiffness for large deflections is accompanied by a faster oscillation. Nevertheless, the filter also applies to the limit cycle response of non-linear systems. When the excitation frequencies change, the responses will still be harmonics of the excitation for non-linear structures. Since mechanical systems normally have transfer characteristics dependent upon frequency, the amplitude and phase of these sine waves will typically also change as the periodic loading change their speed [65]. Table 4.3 compares the Vold-Kalman filter with other noise separation techniques.

Table 4.3: Filter Comparison

	Spectral Methods	**Phase Averaging**	**Hilbert Transform**	**Vold-Kalman**	**Sree's Method**
Nonstationary	No	No	Yes	Yes	Yes
Domain	Frequency	Time	Time	Time	Frequency
Encoder	No	Yes	No	Yes	No
Filter shape	No	No	User set	Adaptive bandpass	No
Phase accurate	No	No	Yes	Yes	No
Processing speed	Fastest	Medium	Medium	Slowest	Fast

Chapter 5

Results and Discussion

For all the conditions covered in this report, the RPM was 56500 ± 1.0 %. This corresponds to a rotor tip Mach number of 0.61 ± 1.0 %. Fan exhaust total pressure was 2.30 psig, which translates to FPR=1.157, rotor induced velocity of 88.9 m/s, fan exit velocity of 159 m/s, and power output of 4700 W (6.3 hp). This translates to a motor conversion efficiency of 92 % according to ESC data logs.

A two-pole second-generation, multi-order using single order scheme Vold-Kalman filter was used to isolate each harmonic from a narrow frequency band around the tracked tone while preserving accurate phase information. To work out the phasor information in the data equation, the tracked tone was determined by the instantaneous frequency of the rotor specified by the RPM sensor. Although the signal consists of a rapidly changing frequency, the Vold-Kalman filter is able to track even at extreme slew rates. Filtering of the 23 microphone data for 6 orders took a few minutes on an Intel Xenon based desktop computer using the Matlab® backslash matrix solver. No down-sampling was applied. The acoustic results will be presented as follows:

1. Isolated ducted fan time history, plotted for various polar angles, referenced to 305-mm arc.

2. Isolated ducted fan narrowband SPL spectra in laboratory scale, referenced to 305-mm

arc.

3. Narrowband SPL spectra in laboratory scale, and directivity of fan shielding effects. Referenced to 305-mm arc.

4. Isolated ducted fan comparison with NASA large scale test, UCI data referenced to a linear traverse displaced 305 mm from the model centerline.

5. Shape parameters determined through least-squares matching of the measured far and near-field cross-spectra density.

6. Diffraction computation using BEM and comparison to UCI data.

5.1 Decomposition of Time Traces

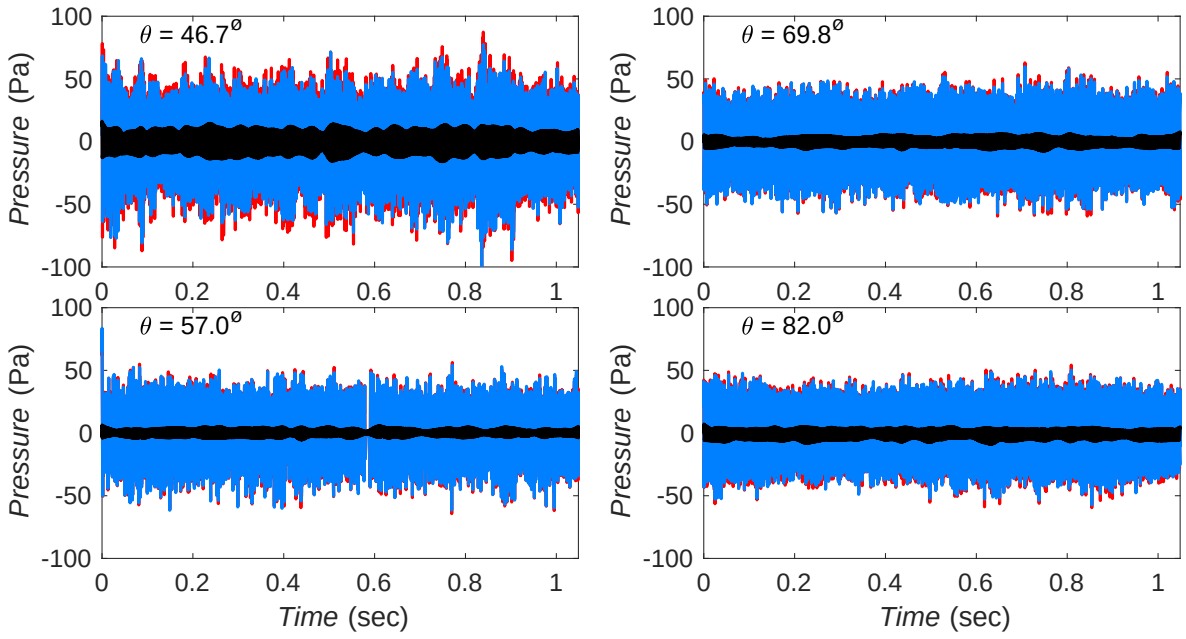

Figure 5.1: Time domain signal decomposition of the ducted fan noise at various polar angles. Total signal (red), broadband (blue), harmonic (black).

We first examine the Vold-Kalman decomposition of microphone signals at various polar angles as a function of time. Each panel of Fig. 5.1 plots the time history at an fixed

microphone location. The number of samples was 262144 per microphone, or 1.04 seconds of data. Total, broadband, and harmonic are colored red, blue, and black, respectively. The amplitudes of the noise components are dependent on the polar emission angle. At a polar angle of $\theta = 46.7°$, the amplitude of the overall and tonal pressure fluctuation is largest. Furthermore, the harmonic component amplitude varies, a local minimum exists at $\theta \sim 57.0$ ° before increasing for smaller or larger polar angles. This phenomenon illustrates the complexity of the tonal sound field. At polar angles between 70-80°, the amplitude of the broadband noise encompasses the majority of the signal.

5.2 Narrowband Spectra

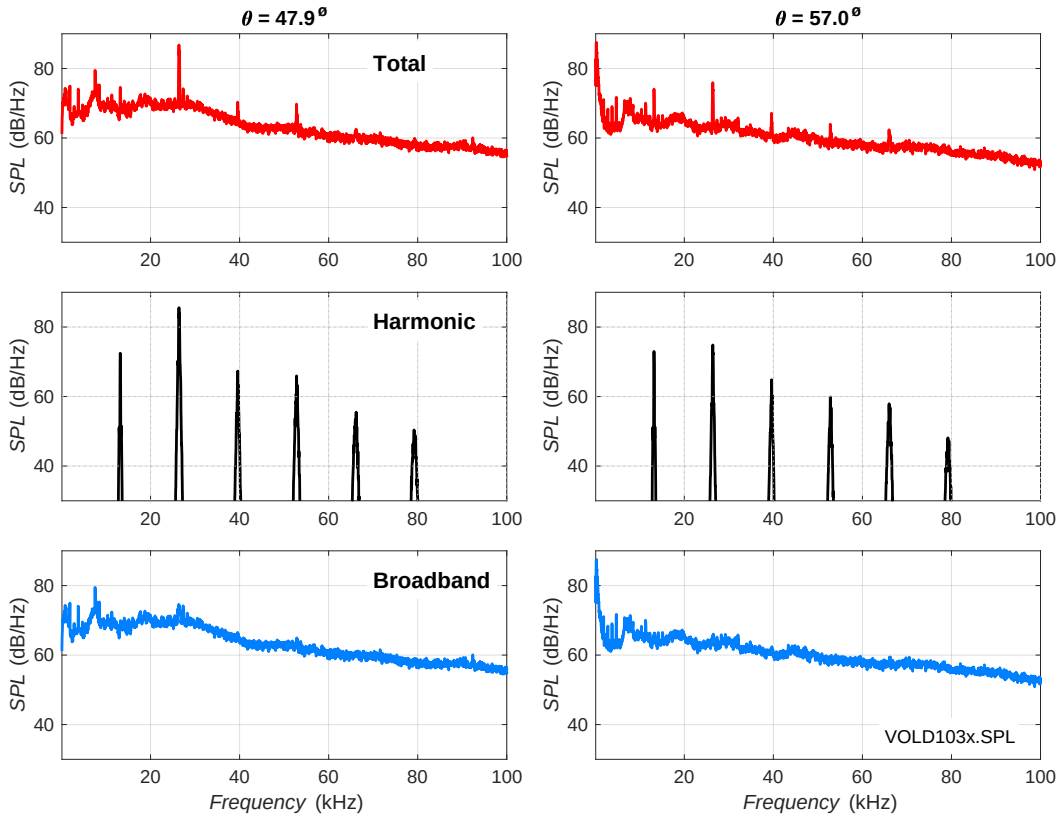

Figure 5.2: Narrowband SPL spectra at two polar angles. Total signal (top), harmonic (middle), broadband (bottom).

The second set of assessments consists of conventional spectral analysis of the Vold-

Kalman filtered signals for two polar angles, θ=47.9° and 64.0°. The SPL narrowband spectra were corrected for actuator response, free-field correction, and atmospheric absorption, resulting into lossless spectra. Narrowband spectra are shown in Fig. 5.2. Spectral analysis of the microphone signal shows that tones up to 5× BPF were resolved. For rigorousness, six orders were filtered from the total signal using the Vold-Kalman filter. The Vold-Kalman weighting factor was determined by minimizing the "divots" (or negative peaks) in the broadband spectrum, giving a bandwidth of 1.5 Hz. The weighting factor was below the recommended limit described by Tuma for a two-pole, second-generation filter [62]. The black line (middle image) represents the harmonic components that were isolated from the total signal. The bandwidth of each tone relates to the tonal energy removed at that particular order. Spectral lines are sharp separating precise BPF harmonic components. Subtraction of the total signal from the BPF harmonics (black) yields the broadband component (blue). Comparing the spectra at the two polar angles, the harmonic content is more prevalent at θ =47.9 °.

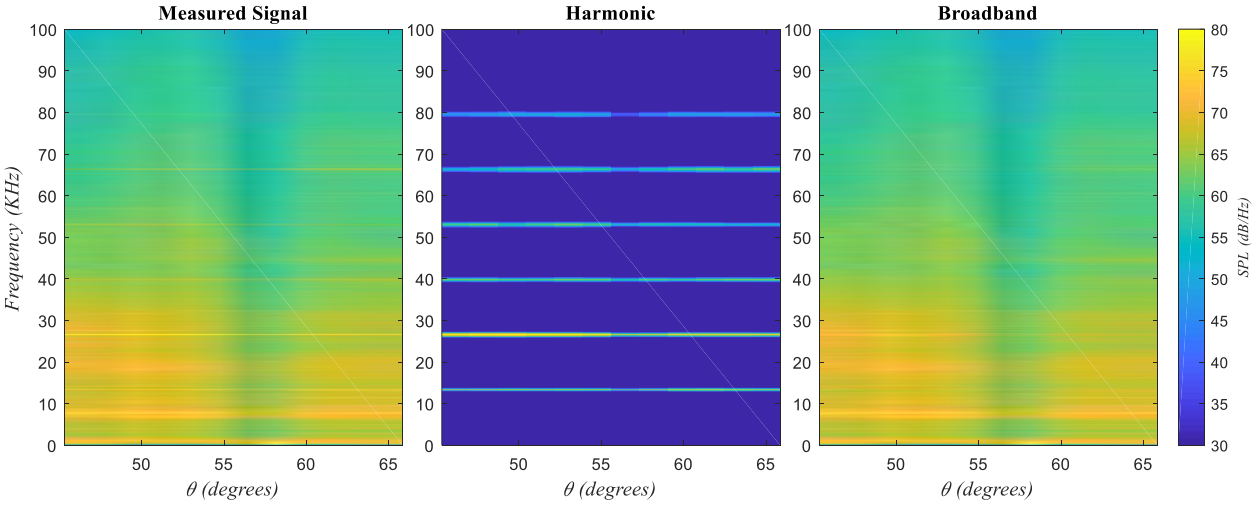

Figure 5.3: Contour plots of narrowband SPL spectra.

Figure 5.3 displays contour maps of the SPL versus frequency and polar angle for the total and decomposed signals. As evident in the contour maps of the harmonic component, rotor harmonics ranging from 1×BPF through 6×BPF are extracted. The tonal energy of the filtered (broadband) signal is substantially reduced compared to the measured signal.

The broadband signal still retains small remnants of tonal noise, which is the effect of some broadband noise being weakly correlated with the shaft orders. The subtraction of tonal noise makes a more pronounced impact at low frequency, indicating the relative strength of the tonal component there. Fig. 5.3 also serves to illustrate the complex directivity of broadband sound, with a local minimum evident near $\theta = 57°$.

5.3 Effect of Nacelle Axial Position and Shield Installation

We now assess the role of engine placement on shielding on the far-field sound level and spectral characteristics. The acoustic results include the acoustic narrowband lossless spectra referenced to 12 in. arc, and directivity of tones as detected from narrowband spectra. The data were obtained with the nozzle centerline located 65 mm above the shielding surface and centered spanwise. The distance of the nozzle exit to the shield trailing edge, X_{TE} was 0, 26 , 52, and 78 mm. A test matrix for the shielding experiment is shown in table 5.1.

Table 5.1: Test Matrix for Rectangular Shielded Experiments

Experiment	X_{TE} (mm)	X_{TE}/D_0	Notation
DFAN103	Isolated		
DFAN092	78	1.10	Nominal position based on BWB0009C drawing
DFAN094	52	.733	0.37× D Aft
DFAN095	26	.367	0.73× D Aft
DFAN102	0	0	Shield TE at Nozzle Exit

Figure 5.4 compares the acoustic of the shielded and unshielded isolated(red) ducted fan. For clarity, only 3 configurations are shown. The narrowband spectrum illustrates the shield placement highly influence the tonal and broadband noise. Furthermore, noise reduction is highly dependent on polar angle. The shield does not produce significant reductions at shallow polar angles ($\theta < 50°$). Thus, maximum suppression occurs for angles directly below the shield. Comparison of different shield arrangements, clearly verify our intuition

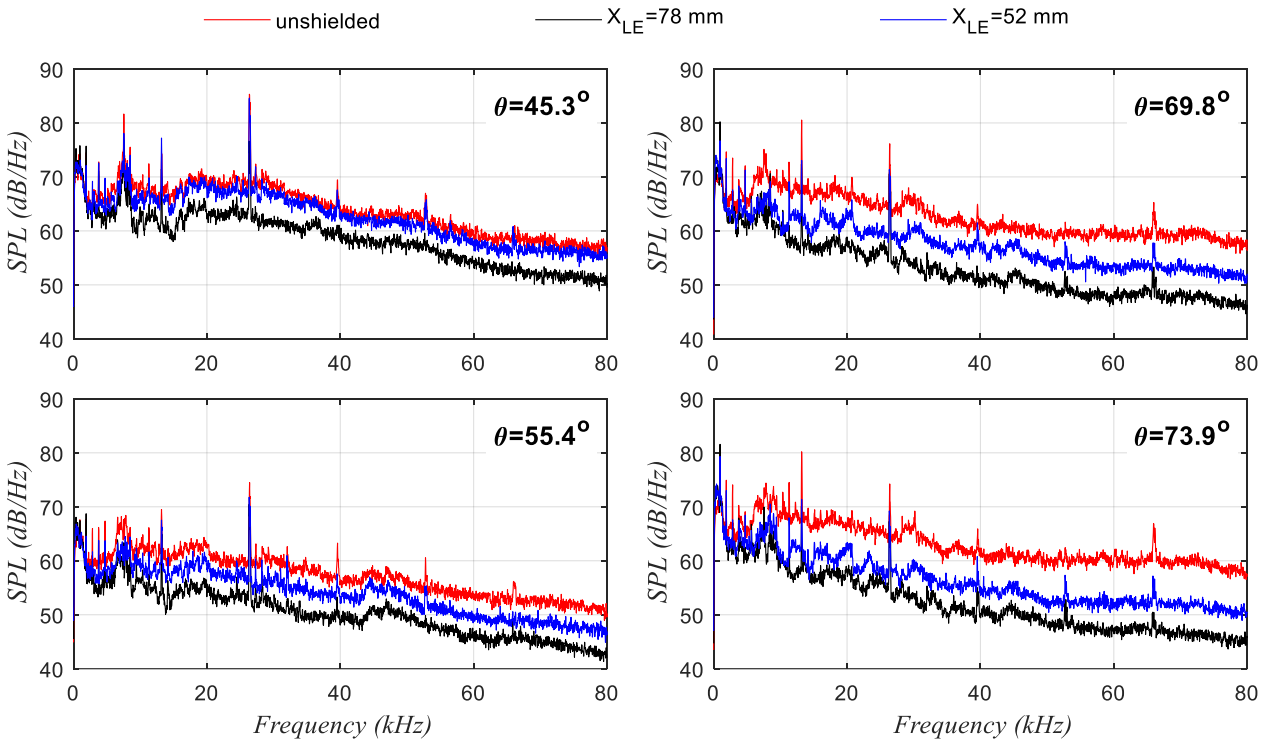

Figure 5.4: Effect of shield on acoustics.

that a larger trailing edge distance, X_{TE} more easily blocks sound yielding greater noise reductions. For instance at $\theta = 73.9°$ and $X_{TE} = 52$ mm, noise reduced by 8.82 dB and 6.3 dB for the 1× BPF tone and broadband noise, respectively.

Figure 5.5 reveals the complicated directivity of the scattered acoustic field due to the effect of shielding on the BPF tones. Some tones are amplified and others are suppressed. Here, the amplification is confined to a shallow polar angles (relative to the downstream direction). This phenomenon arises from constructive interference between the noise source and the sound diffracted by the shield. Additional sound interaction occurs when the nozzle exit and shield trailing edge are coincident ($X_{TE} = 0$ mm). Otherwise, the shield attenuates rotor noise at larger polar angles by approximately 10 dB depending on the particular tone of interest. Thus, the exact placement of the shield has considerable effect on the achievable noise suppression. Moving the engine upstream of the shield trailing edge can produce substantial noise reductions.

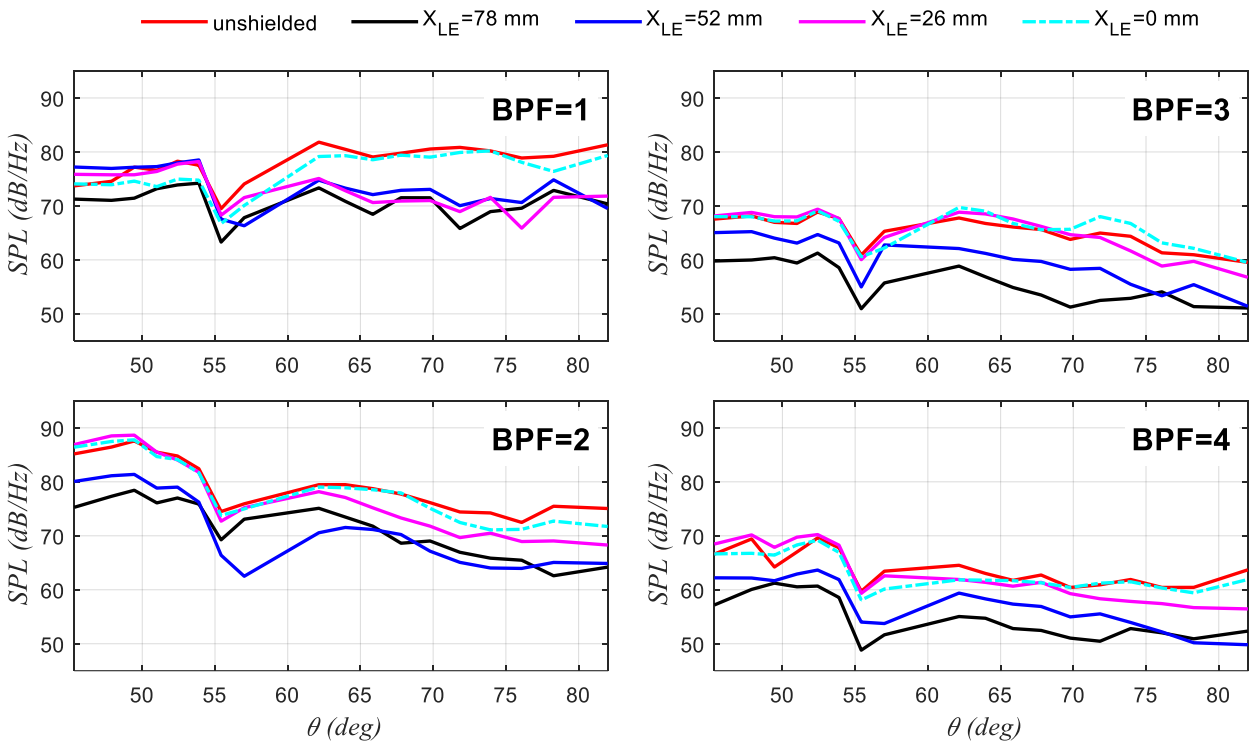

Figure 5.5: Effect of shield on acoustic directivity of the BPF tones.

5.4 Comparison with NASA Large Scale Tests

In this section we make qualitative comparisons of our results with large-scale fan acoustic data acquired at NASA Langley's 9'× 15' tunnel using a continuously traversing microphone [6, 33]. There are significant differences in the fan design and operating conditions between the UCI and NASA rigs. A quantitative comparison in thus impossible. However, the NASA experiment being the only known fan test where a signal decomposition was carried out, we are compelled to try a qualitative comparison.

Table 5.2 summarizes the sizes, operating conditions, and measurement approaches of the two experiments. The most important operational difference was that the NASA rotor was transonic, while the UCI rotor was subsonic. Consequently, the NASA rotor emitted multiple pure tones (MPTs), in addition to the conventional tonal and broadband noise. MPTs are caused by the formation of leading-edge shocks on the suction side of the blades [73].

Table 5.2: Summary of Fan Specifications and Experimental Conditions

Quantity	UCI	NASA
Scale	1:38	1:5
Diameter	2.67 in	22 in
M_{tunnel}	0	0.1
M_{tip}	0.60	1.08
Rotor count	14	22
Stator count	24	26
FPR	1.157	1.47
Power	6.3 hp	5000 hp
Fan hub/ tip ratio	0.42	0.30
Scan Method	Fixed array	Continuous scan
Polar angle	15° to 110°	46° to 152°

The resulting nonlinear quadrupole term transfers acoustical energy from BPF harmonics to other modes that radiate upstream [74]. For a perfect fan, with meticulous blade spacing and uniform blade geometry, the shock system will only emit energy at integer multiple of the BPF. However, natural manufacturing variations produce shocks of non-uniform amplitude and spacing, resulting in numerous tones in addition to the BPF harmonics. These additional harmonics are called MPTs and are often referred to as “buzz saw" noise. Some MPT harmonics can be louder than the BPF tones. Buzz saw tones are deterministic and are separated as a harmonic component.

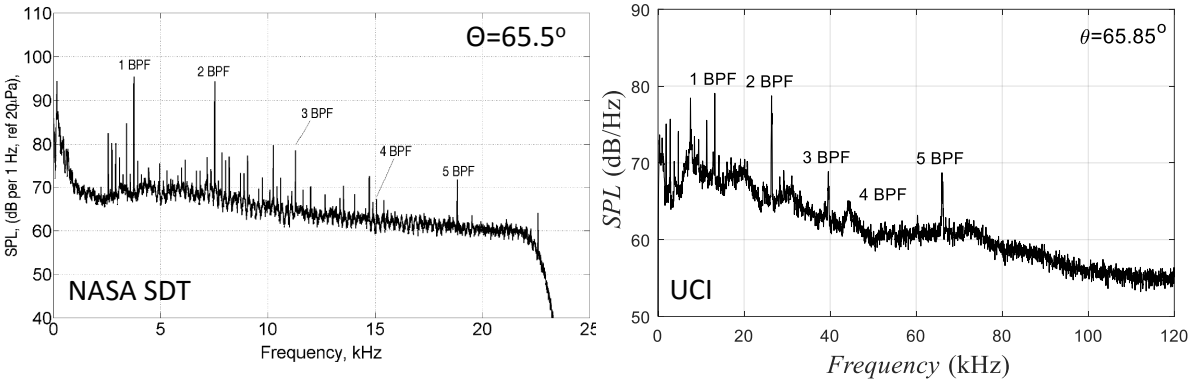

Figure 5.6: Comparison of UCI and NASA Narrowband SPL from Shah [6] for a exhaust arc microphone at $\theta = 65.5°$.

From the measurement standpoint, the NASA tests utilized a single microphone travers-

ing a straight sideline path at a speed of 0.0102 m/s (0.4 in/s), covering small to large polar angles θ (using UCI's geometric convention) [6]. Because the microphone was moving continuously through the sound field the spatial resolution was practically infinite. In contrast, in the UCI experiment a number of stationary microphones were placed at fixed polar angles. Note that the range of polar angles was different in each experiment, UCI emphasizing the aft angles while NASA surveying mostly the forward angles. NASA's one-third octave spectra were interpolated to UCI's polar angles to facilitate comparisons. In addition, the UCI sound measurements were scaled to the distances along an axial traverse offset of 12 in. from the jet centerline.

Comparisons of the narrowband sound pressure level (SPL) spectra for identical polar angles are shown in Fig. 5.6. This microphone location represents an aft polar angle. Both spectra are dominated by the blade passage frequency harmonics of the rotor-stator interaction, which are above the broadband level up to the fifth BPF harmonic. Furthermore, the distribution of energy from the BPF harmonics are similarly suppressed. For instance, the first two BPF are of equal amplitude followed by the third harmonic which protrudes from the broadband at half of the amplitude of the lower harmonics.

Fig. 5.7 compares the polar directivities of 1/3-octave bands of the UCI and NASA experiments, both scaled to the full-scale diameter of 2.67 m. The comparison is done at similar, although not identical, frequency bands. The first comparison band includes the 1×BPF harmonic, and the second comparison band includes 4 & 5×BPF (UCI) and 4×BPF (NASA). The NASA bands include MPTs, as discussed above. At low frequency, the harmonic content of the NASA fan is stronger than that of the UCI fan, possibly because of the presence of the MPTs. At higher frequency the broadband component dominates in both tests, the harmonic spectrum being on on the order of 15 dB below the broadband spectrum. It is significant that the small-scale test captures the high-frequency trends measured in the NASA facility.

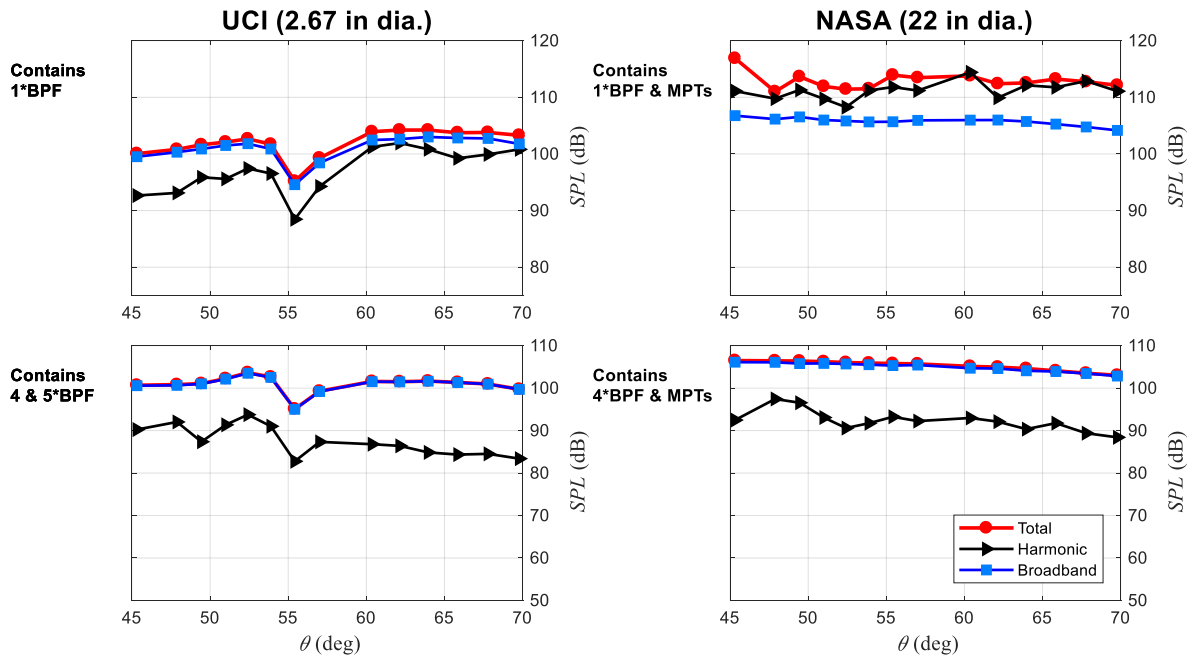

Figure 5.7: Comparison of UCI and NASA one-third octave band directivities. Total signal (red), broadband (blue), harmonic (black).

5.5 Wavepacket Source Parameterization

To properly model traveling waves of the form of "wavepackets" on a cylindrical radiator surface surrounding the exit of the nozzle requires optimization of the model parameters to fit experimental far-field data. Parameterization of the wavepacket requires reasonable initial estimates for the azimuthal mode m, and axial wavenumber k_z (or convective velocity). Turbofans produce an infinite number of azimuthal modes. However, numerous experiments with azimuthal microphone measurements show the predominance of Tyler-Sofrin modes [19, 75]. For our mini turbofan which contains 14 rotor blades and 24 stator blades, the Tyler-Sofrin rule describes the most energetic azimuthal modes must obey:

$$m = 14h + 24k \qquad k = \ldots, -1, 0, 1, \ldots \tag{5.1}$$

Table 5.3 present the main azimuthal modes for tones up to the second harmonic.

Table 5.3: Dominant Azimuthal Modes from Tyler-Sofrin Rule

mode	harmonic	integer,k	k_z (m^{-1})
m=14	h=1	k=0	166.9
m=4	h=2	k=-1	334.8
m=28	h=2	k=0	333.9

Modes $m = 14$, 28 are due to the rotor-only field for the first and second BPF, which rotate at the shaft speed. A vane-blade ratio of less than two ensures that the interaction of the first harmonic lies within the propagating region. On the other hand, $m = 4$ is due to the rotor-stator interaction field. This interaction mode rotates seven times the angular velocity of the subsonic rotor according to $hB\Omega/m$. While the rotor tip speed is subsonic, this interaction field rotates much faster than the rotor itself, increasing the efficiency of propagation. Thus, this fan-stator interaction mode is expected to dominate the sound field for the second harmonic. To summarize, $m = 14$ and $m = 4$ are two azimuthal modes that will best fit the experimental conditions. Corresponding axial wavenumber, k_z, inferred from the duct mode dispersion relation are computed on the right hand side of table 5.3.

5.5.1 Far Field Parameterization

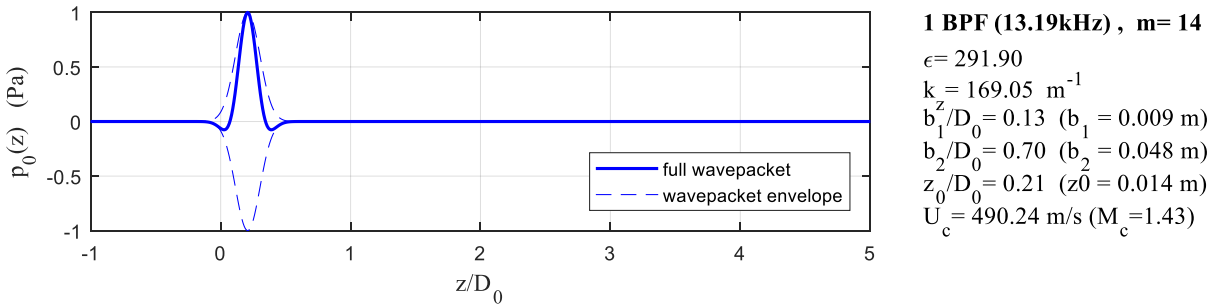

Figure 5.8: Results of parameterization for fundamental blade passage frequency (1 × BPF). Plotted is the wavepacket shape. Optimum parameters are $\epsilon = 291.8$, $k_z = 169.05$ ($U_c = 490$ m/s), b_1/D_0 =0.13, b_2/D_0 =0.70, z_0/D_0 =0.21.

Figures 5.8- 5.9 exhibit parameterization results for 1× BPF using far-field experimental data. An asymmetric wavepacket (equation 3.19) was used as the equivalent noise source. Fig 5.8 depicts the full wavepacket shape $p_0(z)$, and demonstrates the primary source region

of the aft fan noise. The wavepacket Gaussian width parameters b_1, b_2 are consistent with those found from computations [76]. In addition, the optimized convective speed, U_c of the wavepacket is in line with analytical estimates. The axial location of the peak noise source relative to the exit, z_o is fairly close to the nozzle exit. This placement of the origin of the assumed source coordinate system affects the output directivity of the reconstructed sound field. These findings shows that the source can be modeled as a short wavepacket on a cylinder surrounding the engine exhaust. The length of the source is critical. It must be close and short enough to the nozzle for accurate scattering computation. The apparent relationship between the wavepacket parameters and the far-field sound field may be better understood by comparing the magnitude and phase relationship between various microphones.

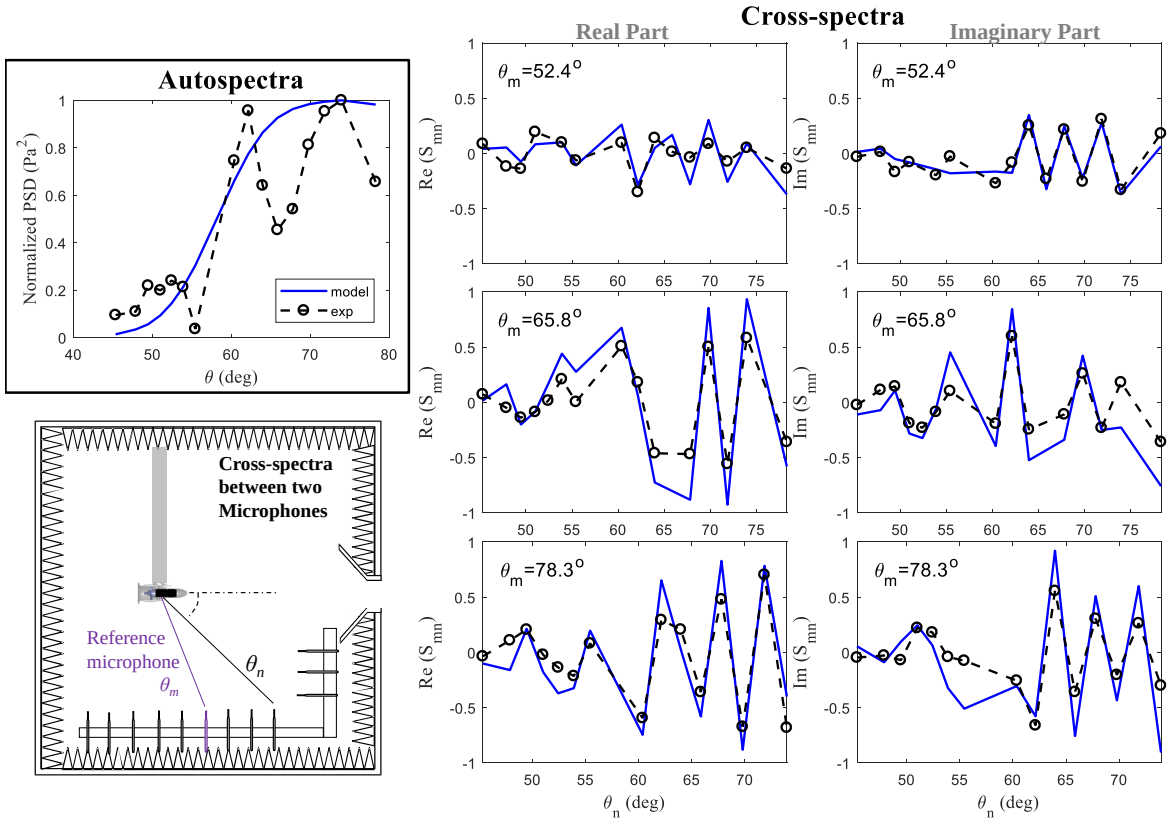

Figure 5.9: Results of parameterization for fundamental blade passage frequency (1 × BPF) in the far-field. Plotted are the modeled (blue) and experimental(black) auto and cross-spectra, and a sketch of the microphone layout.

The first statistical measure- the autospectrum, is plotted on the left of Fig. 5.9 . This

graph describes the distribution of power of the fundamental blade passage frequency (1 × BPF) over a range of polar angles. The modeled polar intensity distribution (blue) is compared with the experimental (black) measurements in the downward direction. The plots are normalized by their maximum value. Notice the jaggedness of the experimental autospectra. The sound radiation pattern power shows a pattern of "lobes" at various angles, separated by "nulls" or minimums. Our wavepacket model has difficulty recreating this complex directional radiation pattern. Wavepacket autospectra are typically smooth, however through optimization the model captures the most prominent features of the experimental data as illustrated in Fig. 5.9. At large polar angle the model intensity is maximum and smoothly decays for shallow polar angles.

More important are the statistics between microphones: the cross-spectra. Here one microphone is fixed (purple microphone at θ_m) and its signal is compared to others (θ_n) as demonstrated in the bottom left drawing in Fig. 5.9. Cross spectral analysis allows one to determine relationship or similarity of the fundamental blade passage frequency signal (1× BPF) over a range of polar angles. The real part (co-spectrum) is the in-phase signal and the complex (quadrature spectrum) is the out-of-phase signal. On the right side of Fig. 5.9 are plots that compares the model and experimental cross-spectra (real and imaginary components) for three reference microphone θ_m. Good fit can be obtained between the modeled and experimental cross-intensity polar distributions across numerous microphones. The wavepacket model captures both in-phase (real) and out-of-phase (imaginary) relationships.

Similar statistical observations are obtained in Fig. 5.10-5.11 for the parameterization of the second harmonic (2× BPF). Note the parameters of the wavepacket written in the right hand side of Fig. 5.10. Variables such as asymmetric Gaussian width, b_1, b_2, wavepacket alignment z_0, are smaller than those of 1× BPF for this interaction azimuthal mode, $m = 4$. This phenomenon is in line with computational results from Hu *et al* [76]. Furthermore, reasonable fit were obtained between the modeled and experimental auto and cross-spectra particularly for large polar angles.

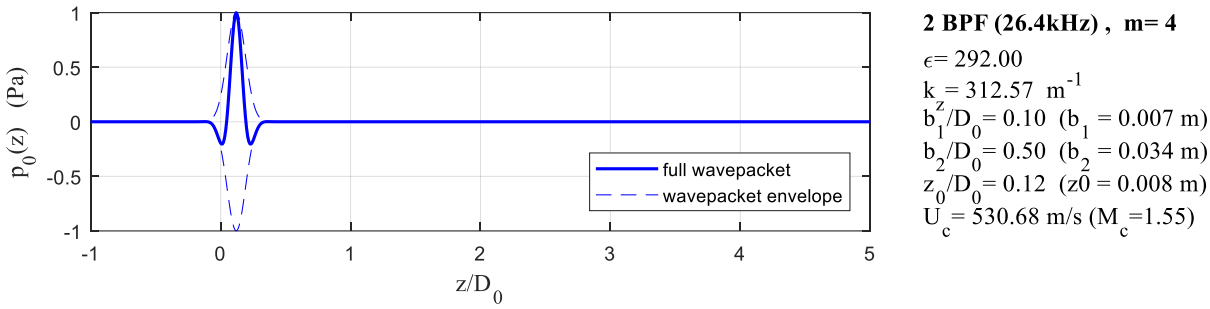

Figure 5.10: Results of parameterization for 2^{nd} harmonic (2 × BPF). Plotted is the wavepacket shape. Optimum parameters are $\epsilon = 292.0$, $k_z = 312.57$ ($U_c = 530.68$ m/s), b_1/D_0 =0.10, b_2/D_0 =0.50, z_0/D_0 =0.12.

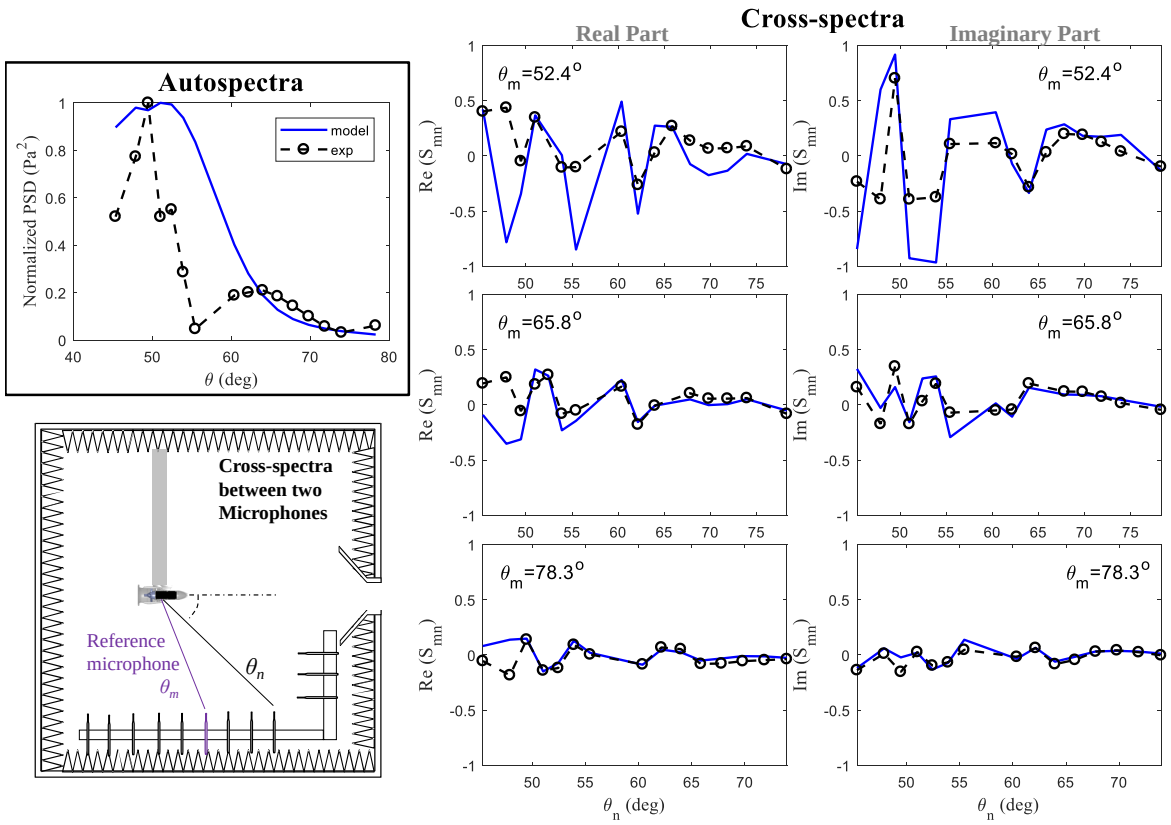

Figure 5.11: Results of parameterization for fundamental blade passage frequency (2 × BPF) in the far-field. Plotted are the modeled (blue) and experimental (black) auto and cross-spectra, and a sketch of the microphone layout.

5.5.2 Near Field Statistics and Parameterization

It is important to realize that far-field phased array measurements detect only the radiating part of the noise source. Acquiring pressure signals just outside the mixing layer by an near-

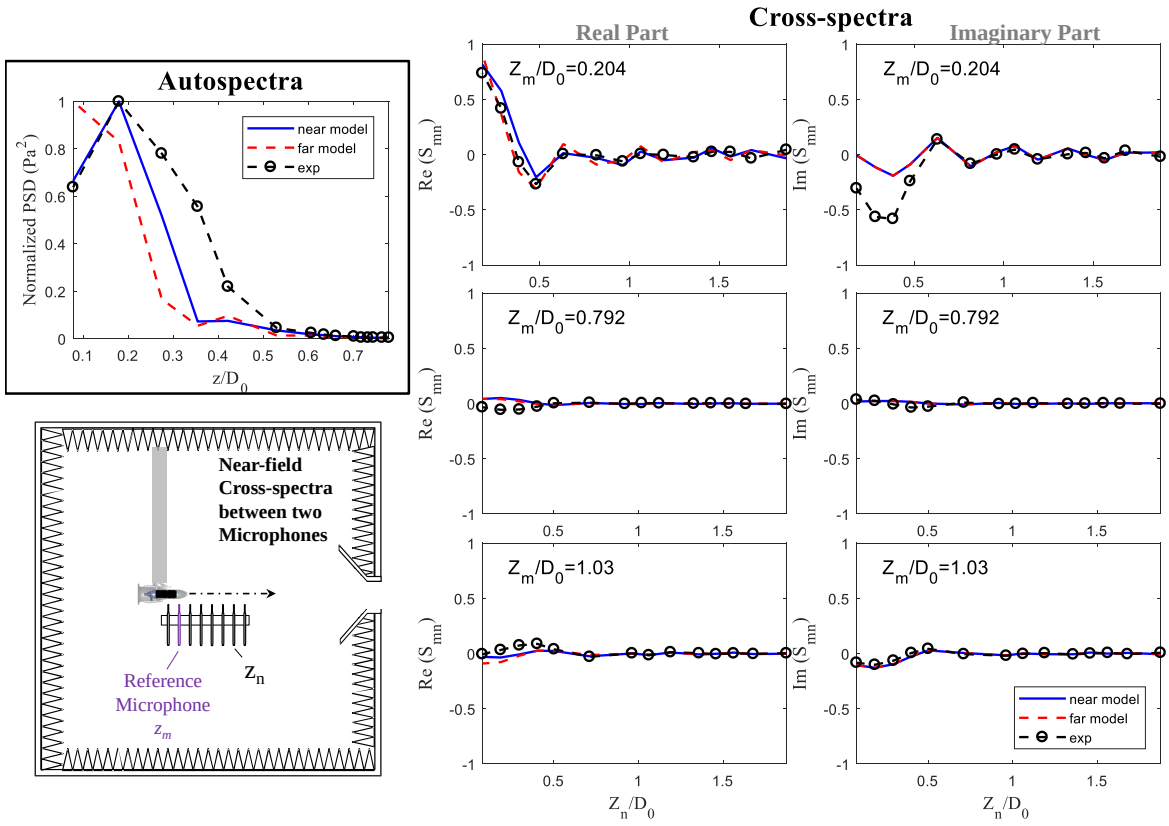

Figure 5.12: Results of parameterization for the fundamental blade passage frequency (1 × BPF) in the near-field. Plotted are the near field parameterized model (blue), far field parameterized model (red), and experimental (black) auto and cross-spectra. The near-field microphone layout is sketched in the lower left corner.

field microphone array captures the evanescent pressure field associated with wavepackets, which is exponentially decaying with radius in this region. This allows us accurately infer properties of the source, and propagate to the far-field to determine whether the pressure field is consistent with the wavepacket. This observation is essential to establish quantitative cause-and-effect relationships between the dynamics of near-field modal structures and far-field sound. The array microphones are located at $z/D_0 = 0.074$ from the nozzle exit, and extends to $z/D_0 = 5.99$.

Figure 5.12 presents the experimental and modeled statistics in the near-field. The wavepacket labeled "far model" is identical to foregoing far-field parameters for 1×BPF. The autospecta illustrates the evolution of pressure amplitude along the near-field microphone

array. The experimental signal appears to grow, saturate around z/D_0=0.22, and decay. Conversely, the modeled intensity distribution saturates near the nozzle exit and decay slower than the experimental autospectra. More significantly, the cross-spectra in-phase (real) and out-of-phase (imaginary) relations closely follow the experimental data. As the frequency is increased (2× BPF), the near-field fits are problematic. Wavenumbers associated with 2× BPF are near the upper limit of the nearfield array microphone spacing reported here. Similar to far-field observations for 2× BPF, larger differences in near-field cross-spectra terms occurs than those of the fundamental tone. We hypothesize that more complex functional forms of the wavepacket envelope $p_0(z)$, will address this problem.

Table 5.4: Far and Near-Field Parameterized Wavepacket Variables

	Far Field	**Near Field**
k_z (m^{-1})	169.05	167.67
b_1/D_0	.13	.126
b_2/D_0	.70	.65
z_0/D_0	.21	.28

Table 5.4 compares the reconstructed wavepacket shape parameters acquired from far and near-field microphone arrays. The axial wavenumber (k_z) and asymmetric Gaussian widths (b_1, b_2) are at most 8% different. Conversely, the axial location of the peak noise source relative to the nozzle exit, z_0 is further downstream for the near-field parameterization. This variable reshapes the evolution of pressure amplitude along the near-field microphone array as illustrated in the autospectra of Fig. 5.12. Near field parameterized signal is plotted in blue/ The modeled autospectra appears to grow, and saturate similarly to experimental findings. However, the modeled intensity distribution decays much faster. Overall, much improvement in fitting is observed. Near-field cross-spectra relationships are unaffected by the axial placement of the source. Furthermore, far-field statistics such as those depicted in Fig. 5.9, are insensitive to minor changes in axial placement. This is because a lot of information is lost when measurements are taken away from the source.

One of the most truly remarkable aspects is the degree of consistency of the cross-

spectra in the near and far-field. This continuity illuminates the existence of modal structures which radiate sound. These findings suggest traveling waves of the form of "wavepackets" on cylindrical radiator surface fundamentally works as a equivalent tonal noise source for sound generated by the exhaust of a ducted fan.

5.6 Diffraction Predictions

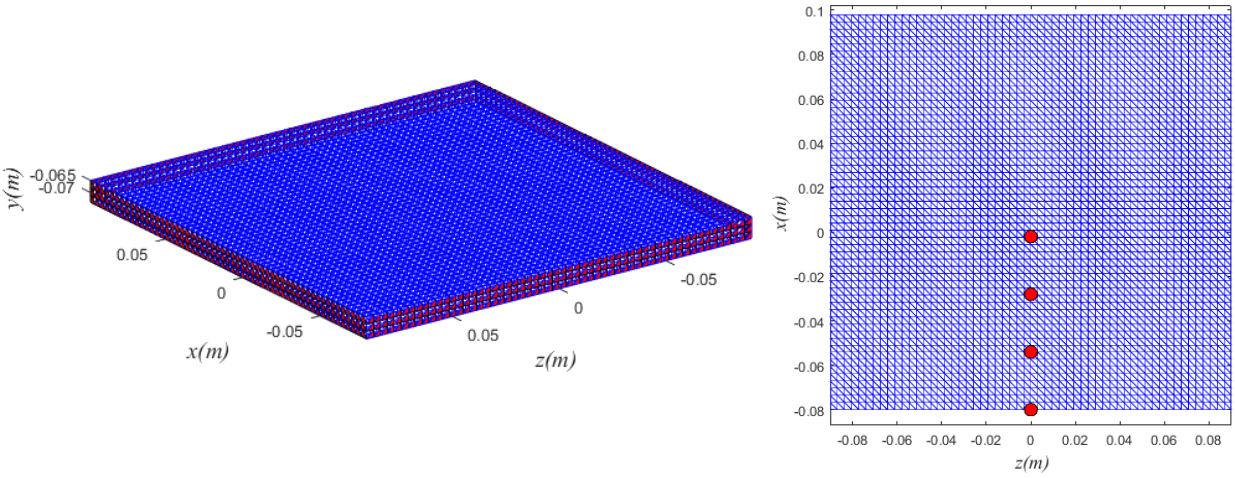

Figure 5.13: Rectangular flat plate mesh used in boundary element method (BEM) computations. Red dots in the right image represents the source centers for various trailing edge locations, X_{TE}.

In this final section, we evaluate the predictive capability of far-field fan noise shielding using our low-order, physics-based cylindrical wavepacket source model. The sound is scattered and diffracted by an rectangular flat plate, which is discretized into a finite number of 8 node per wavelength triangular elements. Trials with different mesh coarseness ranging from 8 nodes to 4 nodes per wavelength, show insensitivity of the results. The computational plate geometry aims to preserve the critical dimensions of the UCI's experimental setup. The boundary dimensions used in the experiments was 1.5 mm thick by 609.6 mm wide (span). Conversely, the computational geometry was 17.8 mm thick by 180 mm wide. The reason is that BEM cannot handle very thin plates, so the plate is thicker for the computations. Moreover, the span was reduced since the BEM cannot have boundary surface with more

than 7000 elements. Surface dimensions and source locations are summarized in table 5.5 and illustrated in Fig 5.13.

Table 5.5: Surface Dimensions and Noise Source Location

Elements per wavelength for mesh	8
Mesh type	triangular
Chord length	.178 m
Model Span	$S = .18$ m
Distance between nozzle exit and trailing edge	$X_{TE} = 0$, 26, 52, 78 mm
Elevation of noise source above shield	65 mm
Number of elements for 1× BPF	7083

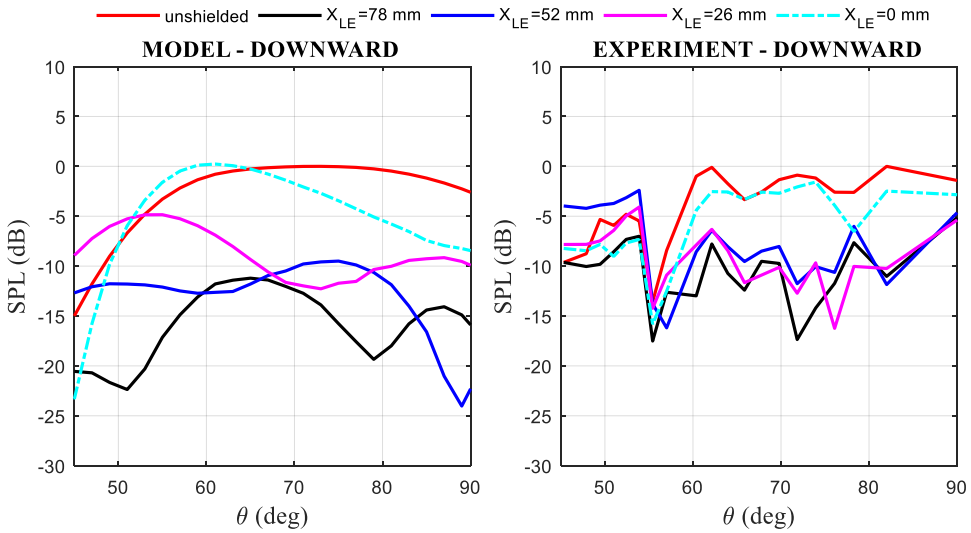

Figure 5.14: Comparison of 1× BPF aft fan noise shielding intensity distributions for experimental investigations and BEM predictions.

Figure 5.14 compares the shielding predictions from the BEM with their experimental counterparts for various axial trailing edge locations, X_{TE}. The plot on the left side correspond to the numerical intensity distribution whereas the results on the right side corresponds to the experimental results. The distributions are plotted versus polar angle for 1× BPF, and the red curves represent the isolated or unshielded ducted fan. Only results for the first harmonic are displayed, as computations for 2×BPF exceeded memory limits. The numerical results predicts complicated changes in far-field noise radiation when shielded. For $\theta < 55°$, the wavepacket model fails to capture the pattern of "lobes" or "nulls" present in the

experimental data, thus predictions are non-physical in this region. For larger polar angles, computations capture the average noise reductions seen the experimental data. Oscillations of the intensity distribution are not as well reproduced. Table 5.6 compares the insertion loss around the mid-range polar angle of $\theta = 65°$. Experimental noise reductions are not simply monotonic, highlighting the complexity of the noise physics. Values from table 5.6 indicate that the airframe significantly suppresses the noise in this region. For the fundamental tone, 1× BPF, the computations capture the experimental noise reduction reasonably well, with some over-prediction of reduction at $X_{TE} = 52$ mm.

Table 5.6: Computational and Experimental Shielding Insertion Loss

$X_{TE}(mm)$	ΔSPL_{model}	ΔSPL_{exp}
78	10.95	9.09
52	11.54	6.22
26	9.09	9.07
0	0	0

Chapter 6

Conclusion and Future Work

A large number of experiments in uninstalled and installed configurations have validated the capability of the small-scale rig to reproduce the fan noise emitted by the turbofan engine and have demonstrated the large potential to reduce noise through shielding by the airframe. Complementing our earlier studies of the isolated and installed small-scale ducted fan [29], this work demonstrates that important aspects of fan noise can be studied at low cost in university-scale facilities, leveraging advances in additive manufacturing and brushless motor technology. The rapid-prototyped ducted fan featured a 14-bladed rotor and 24 stators, and operated at fan pressure ratio of 1.157 and rotor tip Mach number of 0.61. Its operation was representative of future geared turbofan engines with very large bypass ratio.

This project demonstrated the application of Vold-Kalman filtering of aeroacoustic measurements from a small scale ducted fan, for the purpose of rigorously determining the harmonic and broadband components of noise. Knowledge of the tonal and broadband noise content is essential for characterizing the fan noise source and predicting propulsion-airframe integration effects. A second-generation Vold-Kalman filter was employed to separate the time-domain contributions of harmonic and broadband contents. This filter is advantageous to frequency domain methods since it can easily localize information with high resolution needed to correct for the non-stationary behavior in real world experiments.

Fan exhaust discrete tone noise was modeled as a cylindrical wavepacket with azimuthal modes inferred from the Tyler-Sofrin theory and shape parameters determined through least-squares matching of the experimental Vold-Kalman filtered tonal cross-spectral density in the far field. A asymmetric wavepacket was used as the equivalent noise source. This framework provides, a deterministic model that capture the salient physics of the source and that allow understanding and enable predictions of the radiated sound and its scattering around objects without inordinate computational resources. Parameterization shows that the amplitude modulated traveling wave on a control surface (Kirchhoff) surrounding the exit of the nozzle can be modeled as short cylindrical disturbances. The length of the source is critical since it must be close and short enough to the nozzle for accurate scattering computation. Our wavepacket model captures the most prominent far-field and near-field experimental magnitude and phase relationship across numerous microphone (i.e. cross-spectra distribution). One of the most truly remarkable aspects is the degree of consistency of the cross-spectra in the near and far-field. This continuity illuminates the existence of modal structures which radiate sound. These promising results indicate that the noise radiated by modal structures in the form of traveling waves or "wavepackets" fundamentally works as a equivalent tonal noise source for sound generated by the exhaust of a ducted fan.

Installation of a rectangular flat plate representing the airframe enables experimental studies of the diffraction of the sound emitted by the ducted fan. Addition of the rectangular plate shield created complex trends in the tonal content and demonstrated the large potential to reduce noise through shielding by the airframe. Tones below the shielding surface were well attenuated, while tones emitted in the aft direction were poorly shielded. Numerical shielding prediction using Boundary element method (BEM) exhibit complicated changes in far-field noise radiation. For $\theta < 55^\circ$ the wavepacket model fails to capture the pattern of "lobes" or "nulls" present in the experimental data, thus predictions are non-physical in this region. For larger polar angles, computations capture the average noise reductions as seen in experimental data. Oscillations of the intensity distribution are not as well reproduced.

This new framework provide more general methods for the effects related to propulsion airframe aeroacoustic interaction, and allows for low-noise optimization of the BWB aircraft with an ultra high bypass propulsor. In addition, such improvements strengthen insight and understanding into controlling noise physics.

6.1 Recommendations For Future Work

The semi-empirical fan noise source model was calibrated to takeoff conditions. As the fan tip speed varies across the operating regime of the engine, the properties of the wavepacket shape changes. Future revisions to this framework includes the parameterization of experimental data simulating the certification points of approach and cutback (61.7% and 87.5% of design conditions, respectively). Furthermore, the mechanisms that generate aft-radiated noise are similar to those that generate the forward-radiated noise. Therefore, the wavepacket can be reframed to model inlet radiated noise in future explorations.

To expand this model to cover a wide range of fan diameters, mass flow rate, and fan pressure ratio, the current "state of the art" in empirical predictions (ANOPP module HDNFAN) utilizes the Heidmann normalization as part of its underlying framework [77]. This amounts to simple sound pressure level corrections based on the fan temperature rise and mass flow rate. One limitation to more complex corrections concerns the experimental data used to formulate the model. In other words, acoustical experiments investigating numerous engine operating conditions and configurations are prohibitively expensive and laborious. CFD provides a relatively low cost and useful way to assess the effect of geometry, shape, and flow conditions on the noise propagation and directivity. These computational solutions can inform the prescription of the noise source on the radiator surface [17].

Several topics were not thoroughly examined in the present work due to complications. Significant effort was entailed in the design and construction of a small-scaled ducted fan rig that includes all the relevant components of the turbofan engine and simulates accurately

the sound emission generated by the fan of such engines. The nacelle (including the stators) were fabricated during a previous investigation using simple thermodynamic relations and specified camber (metal angles). Redesign of the fan for improved reliability using aluminum metal casting and more advanced turbomachinery design codes enhanced the compression capability. As a result, the originally designed stator pitch and metal angles may not recover the induced tangential velocity as proficiently, lowering the thrust performance of the engine. However, since this fan was meant to be representative of current technology, this compromise was deemed to be acceptable for this test. Future experiments involving low-noise stator designs such as stator sweep or lean dictates the re-optimization of this baseline radial stator set.

Another obstacle was the 7000 element limit for regular BEM diffractions simulations. This constraint entails reducing the computational domain (i.e. wing span) and low spatial grid resolution (4 nodes per wavelength) to get inside the limit. Trials with different mesh coarseness show insensitivity of the results with the finest mesh containing 8 nodes per wavelength. In addition, minor changes in intensity distribution emerged with increasing wing span. However, computations for 2×BPF failed since it exceeded element limits. FastBEM can handle much larger matrices, possible up to 10,000 elements and is sold commercially through CAE Research lab. Extensive comparisons between conventional and fastBEM will provide confidence in predictions. Additionally, this tool can provide insight into realistic shield geometry such as the BWB. In addition, acoustical impacts such as the placement of the engines, geometry of elevon, and positioning and shape of the vertical fins can be numerically predicted.

Future enhancement to this approach of simulating fan noise is to increase power. An power boost permits operating at higher fan pressure ratio such as those found at NASA Glenn which operate at FPR=1.46. Power can increase from 5 kW (FPR=1.15) to 14 kW (FPR=1.29) or 22 kW (FPR=1.46) depending on components. This is accomplished two ways: increasing the voltage or capacity of the battery. The lithium-polymer pack and the

web of connectors between cells used to power the fan cost a great deal. Luckily, such improvements may be incremental. That is, to purchase and reconfigure battery packs and upgrade ESC over time. During renovation of the test rig the battery capacity was increased (connected in parallel), which enables larger total current draw through this distributed system. Moving beyond to higher voltages (15S), consist of adding two NeuEnergy 3S 8300 mAh battery pack and the acquisition of a new MGM COMPRO electronic speed controller. The cost of this upgrade is approximately $1000.

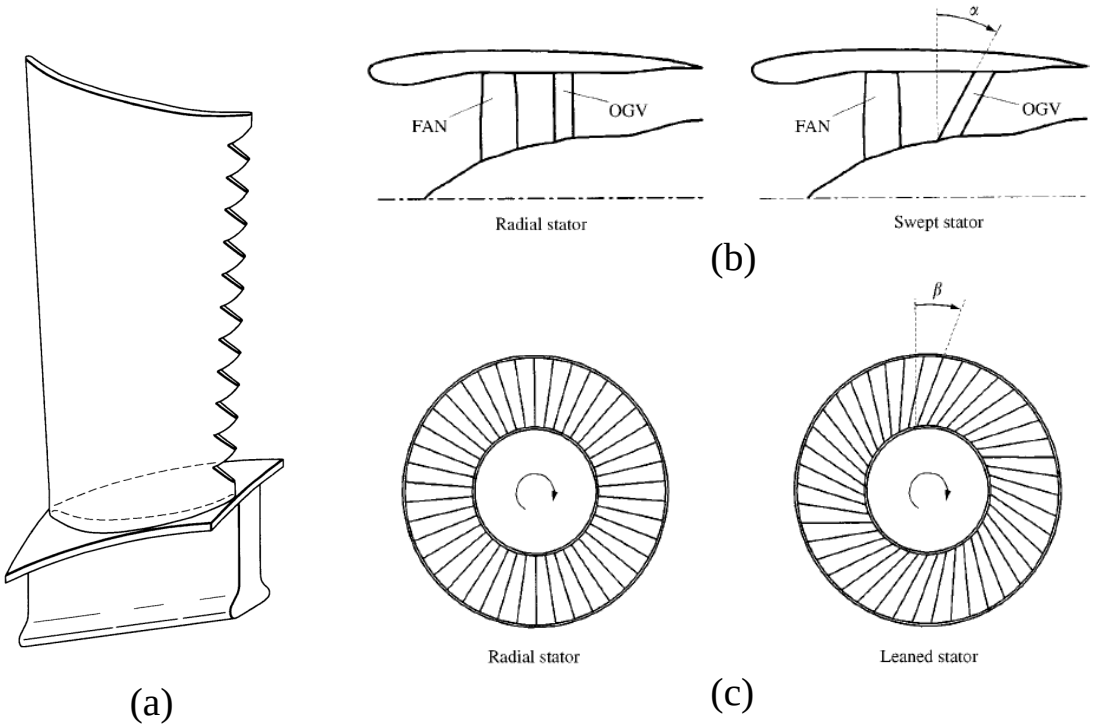

Figure 6.1: Noise reduction concepts (a) Serrated rotor blade from Gliebe [7], and geometry and definition of stator vane: (b) sweep angle and (c) lean angle form Envia [1].

Several noise reduction technology concepts can be investigated using scale model testing of turbofan engine simulators. Fan noise may be reduced by increasing fan diameter and reducing fan tip speed and pressure ratio. However, of particular importance is reducing rotor-stator interaction noise. Interaction noise may be decreased by increasing the axial spacing between fan blades and vanes, selection of the number of blades and vane to provide cut-off of the blade passage frequency, or noise absorbing acoustic liners. Yet, these noise attenuation techniques affect engine performance, size or weight. Two minimally invasive

concepts are proposed . First are serrated fan trailing edges blades. Serrations like chevrons aim to mix the downstream moving viscous waves due to the rotor velocity deficit before interacting with the stator leading edge. This reduces the instationary stator blade forces that generates noise [78]. Another way to target the noise generated by the periodic impingement of fan wakes on the vanes are low-noise stator design. Sweeping and leaning the outlet guide vane have shown noise reductions of 5 dB for the inlet quadrant and 10 dB for the exhaust quadrant for all angles [1]. Here, tone noise is reduced by introducing a phase variation along the span of the vane, from the hub to the tip. When the rotor wake moves downstream it does not strike the stator leading edge all at once reducing the impact of rotor-stator interaction. On the other hand, phase variation by asymmetric stator spacing appears to have "no practical value" according to Sofrin [79]. This report studied the noise benefit for stators with small random variations (due to manufacturing imperfections) from precisely equal spacing in the circumferential direction. Acoustic test suggested asymmetry spreads the acoustic energy over a larger number of modes and was a source of extraneous sound. Studies on optimal non-random uneven stator spacing using psychoacoustic metrics are nonexistent and may be a topic of future exploration.

Bibliography

[1] E. Envia, A. Wilson, and D. Huff, "Fan noise: A challenge to caa," *International Jour of Comp Fluid Dyn*, vol. 18, pp. 471–480, 2004.

[2] S. Rienstra, "Acoustic radiation from a semi-infinite annular duct in a uniform subsonic mean flow," *Journal of Fluid Mechs*, vol. 94, pp. 267–175, 1984.

[3] X. Huang and X. Chen, "Efficient computation of spinning modal radiation through an engine bypass duct," *AIAA Journal*, vol. 46, pp. 1413–1423, June 2008.

[4] S. Redonnet and Y. Druon, "Computational aeroacoustics of aft fan noises characterizing a realistic coaxial engine," *AIAA Journal*, vol. 50, pp. 1029–1048, 2012.

[5] G. Reboul and C. Polacsek, "Toward numerical simulation of fan broadband noise aft radiation from aeroengines," *AIAA Journal*, vol. 48, pp. 2038–2048, 2010.

[6] P. Shah, H. Vold, D. Hensley, E. Envia, and D. Stephens, "A high-resolution, continuous-scan acoustic measurement method for turbofan engine applications," ASME Paper GT2014-27108, June 2014.

[7] P. Gliebe, "Serrated fan blade," US Patent 4,741,207, May 2004.

[8] B. Magliozzi, D. Hanson, and R. Amiet, "Propeller and profan noise," Tech. Rep. N92-10598 01-71, NASA Langley Research Center, Hampton, VA, July 1991.

[9] M. J. Lighthill, "On sound generated aerodynamically: I. general theory," *Proceedings of the Royal Society of London*, vol. 211, pp. 564–587, 1952.

[10] J. Groeneweg and E. Rice, "Aircraft turbofan noise," *Trasactions of the ASME*, vol. 109, pp. 130–140, 1987.

[11] R. Liebeck, "Design of the blended wing body subsonic transport," *Journal of Aircraft*, vol. 41, no. 1, pp. 10–25, 2004.

[12] S. Mayoral and D. Papamoschou, "Effects of source redistribution on jet noise shielding," AIAA 2010-0652, Jan. 2010.

[13] R. Thomas and C. Burley, "Hybrid wing body aircraft system noise assesment with propulsion airframe aeroacoustic experiments," AIAA 2010-3913, June 2010.

[14] J. Berton, "Empennage noise shielding benefits for an open rotor transport," AIAA 2011-2764, June 2011.

[15] A. Truong and D. Papamoschou, "Aeroacoustic testing of open rotors at very small scale," AIAA 2013-0217, jan 2013.

[16] D. Papamoschou, "Prediction of jet noise shielding," AIAA 2010-0653, Jan. 2010.

[17] D. Papamoschou, J. Xiong, and F. Liu, "Towards a low-cost wavepacket model of the jet noise source," AIAA 2015-1006, Jan. 2015.

[18] P. Jordan and T. Colonius, "Wave packets and turbulent jet noise," *Annual Review of Fluid Mechanics*, vol. 45, pp. 173–195, 2013.

[19] T. Sofrin, "Some modal-frequency spectra of fan noise," AIAA 1981-1990, October 1981.

[20] J. Tyler and T. Sofrin, "Axial flow compressor noise studies," *Transactions of the SAE*, vol. 70, pp. 309–332, 1962.

[21] A. Topol, C. Ingram, M. Larkin, C. Roche, and R. Thulin, "Advanced subsonic technonolgy (ast) 22-inch low noise research fan rig preliminary design of adp-type fan 3," Tech. Rep. NASA/CR-2004-212718, NASA Langley Research Center, Hampton, VA, Feb 2004.

[22] C. Hughes, R. Jeracki, R. Woodward, and C. Miller, "Fan noise source diagnoistic test-rotor alone aerodynamics performance results," NASA/TM-2005-211681 (AIAA-2002-2426), Apr. 2005.

[23] L. Heidelberg, "Fan noise source diagnostic test - tone model structure results," NASA/TM-2002-211594 (AIAA-2002-2428), Apr. 2002.

[24] B. Morin, "Broadband fan noise prediction system for turbofan engines, volume 1: Setup bfans user's manual and developer's guide," Tech. Rep. CR-2010-216898, NASA, Nov 2010.

[25] B. Morin, "Broadband fan noise prediction system for turbofan engines, volume 3: Validation and test cases," Tech. Rep. CR-2010-216898, NASA, Nov 2010.

[26] C. Hughes, R. Jeracki, R. Woodward, and C. Miller, "Aerodynamic performance of scale-model turbofan outlet guide vanes designed for low noise," NASA/TM-2001-211352 (AIAA-2002-0374), Dec. 2001.

[27] R. Woodward, "Comparison of far-field noise for three significantly different model turbofans," *AIAA Paper 2008-0049*, Jan 2008.

[28] R. Woodward, D. Elliott, C. Higher, and J. Berton, "Benefits of swept-and-leaned stators for fan noise reduction," *AIAA Journal*, vol. 38, no. 6, 2001.

[29] A. Truong and D. Papamoschou, "Experimental simulation of ducted fan acoustics at very small scale," AIAA 2014-0718, jan 2014.

[30] A. Parry, M. Kingan, and B. Tester, "Relative importance of open rotor tone and broadband noise sources," AIAA 2011-2763, June 2011.

[31] D. Stephens and E. Envia, "Acoustic shielding for a model scale counter-rotation open rotor," NASA/TM-2012-217227 (AIAA-2011-2940), Jan. 2012.

[32] D. Sree and D. Stephens, "Tone and broadband noise separation from acoustic data of a scale-model counter-rotating open rotor," AIAA 2014-2744, June 2014.

[33] D. Stephens and H. Vold, "Order tracking signal processing for open rotor acoustics," *Journal of Sound and Vibration*, vol. 333, no. 16, pp. 3818–830, 2014.

[34] M. Smith, *Aircraft Noise*. Cambridge: Cambridge University Press,, 1st ed., 1989.

[35] C. Ventres, M. Theobald, and W. Mark, "Turbofan noise generation volume 1: Analysis," Tech. Rep. CR-167952, NASA Lewis Research Center, Cleveland, OH, July 1982.

[36] W. Eversman and D. Roy, "Ducted fan acoustic radiation including the effects of nonuniform mean flow and acoustic treatment," AIAA 93-4424, Oct. 1993.

[37] D. Huff, "Fan noise prediction - status and needs," NASA/TM-1997-206533 (AIAA-1997-177), Jan. 1997.

[38] B. Mugridge, "The measurement of spinning acoustic modes generated in an axial flow fan," *Journal Sound Vib.*, vol. 10, no. 2, pp. 227–246, 1969.

[39] S. Grace, D. Sondak, W. Eversman, and M. Cannamela, "Hybrid prediction of fan tonal noise," AIAA 2008-29921, June 2008.

[40] J. Anderson, *Modern Compressible Flow: With Historical Perspective*. New York: McGraw-Hill, 3rd ed., 2003.

[41] R. Haberman, *Applied partial differential equations*. New Kersey: Pearspm Pentice Ha;;, 4th ed., 2004.

[42] E. Rice, M. Heidmann, and T. Sofrin, "Modal propagation angles in a cylindrical duct with flow and there relation to sound radiation," Jan. 1979.

[43] W. Stack, G. Knip, A. Weisbrich, J. Godston, and E. Bradley, "Technology and benefits of aircraft counter rotation propellers," *NASA Technical Memorandum*, Oct 1982.

[44] S. Rienstra, "A classification of duct modes based on surface waves," AIAA 2001-2180, 2001.

[45] G. Gabard and R. Astley, "Theoretical model for sound radiation from annular jet pipes: far- and near-field solutions," *Journal of Fluid Mechanics*, vol. 549, pp. 315–341, Feb. 2006.

[46] M. R., "The interaction of sound with a subsonic jet issuing from a semi-infinite cylindrical pipe," *Journal Fluid Mech.*, vol. 83, no. 4, pp. 609–640, 1977.

[47] P. Sijtsma, "In-duct and far-field mode detection techniques," AIAA 2007-3439, 2007.

[48] D. Sutliff, "Rotating rake turbofan duct mode measurement system," NASA/TM-2005-213828, Oct. 2005.

[49] C. Tam and D. Burton, "Sound generation by the instability waves of supersonic flows. part 1. two-dimensional mixing layers," *Journal of Fluid Mechanics*, vol. 138, pp. 241–279, 1984.

[50] D. Crighton and P. Huerre, "Shear-layer pressure fluctuations and superdirective acoustic sources," *Journal of Fluid Mechanics*, vol. 220, pp. 355–368, 1990.

[51] E. J. Avital, N. D. Sandham, and K. H. Luo, "Mach wave radiation by mixing layers. part i: Analysis of the sound field," *Theoretical and Computational Fluid Dynamics*, vol. 12, pp. 73–90, 1998.

[52] D. Papamoschou, "Wavepacket modeling of the jet noise source," AIAA 2011-2835, June 2011.

[53] P. Morris, "A note on noise generation by large scale turbulent structures in subsonic and supersonic jets," *International Journal of Aeroacoustics*, vol. 8, no. 4, pp. 301–316, 2009.

[54] P. J. Morris, "Jet noise prediction: Past, present and future," *Canadian Acoustics*, vol. 35, no. 3, pp. 16–22, 2007.

[55] D. F. Shanno and K. H. Phua, "Minimization of unconstrained multivariate functions," *ACM Transactions on Mathematical Software*, vol. 6, no. 4, pp. 618–622, 1976.

[56] D. Amos, "Algorithm 644: A portable package for bessel functions of a complex argument and nonnegative order," *ACM Transactions on Mathematical Software (TOMS)*, vol. 12, pp. 265–273, Sept. 1986.

[57] C. Huang and D. Papamoschou, "Numerical study of noise shielding by airframe structures," May 2008.

[58] M. Dunn and J. Tweed, "The application of a boundary integral equation method to the prediction of ducted fan engine noise," NASA 20040086509, 1999.

[59] T. Wu, *Boundary Element Acoustics*. Boston: WIT Press, 2000.

[60] R. Bullock and I. Johnsen, "Aerodynamic design of axial flow compressor," NASA-SP-36, Jan. 1965.

[61] H. Vold and J. Leuridan, "High resolution order tracking at extreme slew rates using kalman tracking filters," SAE Technical Paper 931288, May 1993.

[62] J. Tuma, "Setting the passband width in the vold-kalman tracking filter," 12th International Congress on Sound and Vibration, July 2005.

[63] C. Feldbauer and R. Holdrich, "Realization of a vold-kalman tracking filter- a least squares problem," Proceedings of the COST-6 Conference on Digital Audio Effects (DAFX-00), Dec. 2000.

[64] R. Kalman, "A new approach to linear filtering and prediction problems," *Journal of Basic Engineering, Transactions of ASME*, vol. 82, pp. 35–45, 1960.

[65] H. Herlufsen, S. Gade, K. Hansen, and H. Vold, "Characteristics of the vold-kalman order tracking filter," Bruel and Kjaer Technical Review, Apr. 1999.

[66] H. Wold, *A Study in the Analysis of Stationary Time Series*. PhD thesis, Stockhom University, 1938.

[67] N. Huang, M. Wu, W. Qu, S. Long, and S. Shen, "Applications of hilbert-huang transform to non-stationary financial time series analysis," pp. 245–268, May 2009.

[68] M. Cohen, *"Analyzing Neural Time Series Data"*. Cambridge: "The MIT Press".

[69] R. Oweis and E. Abdulhay, "Seizure classification in eeg signals utilizing hilbert-huang trasnform," *Biomedical Engineering Online*, pp. 10–38, May 2011.

[70] M. Feldman, "Hilbert transform in vibration analysis," *Mechanical Systems and Signal Processing*, vol. 25, pp. 735–802, Apr. 2011.

[71] L. Cohen and C. Lee, "Standard deviation of instantaneous frequency," *Acoustic, Speech, and Signal Processing*, vol. 4, pp. 2238–2241, 1989.

[72] I. Kovacic and M. Brennan, *The Duffing Equation: Nonlinear Oscillators and their Behavior*. New Jersey: John Wiley and Sons, 1st ed., 2011.

[73] A. Goldstein, F. Glaser, and J. Coats, "Acoustic properties of a supersonic fan," NASA/TN-1973-15025, Jan. 1973.

[74] F. Han, C. Shieh, A. Sharma, and U. Paliath, "Multiple pure tone noise prediction and comparison with static engine test measurement," AIAA 2007-3523, May 2007.

[75] A. Maldonado, R. Miserda, and B. Pimenta, "Computational tonal noise prediction for the advanced noise control fan," AIAA 2012-2128, 2012.

[76] F. Hu and X. Li, "Time domain wave packet method and suppression of instability waves in aeroacoustic computations," *Journal of the Fluids Eng.*, June 2014.

[77] M. Heidmann, "Interim prediction method for fan and compressor source noise," NASA/TM X-71763, 1979.

[78] D. Geiger, "Comparative analysis of serrated trailing edge designs on idealized aircraft engine fan blades for noise reduction," Master's thesis, Virginia Polytechnic Institute, Dec. 2004.

[79] T. Sofrin and D. Mathews, "Asymmetric stator interaction noise," *Journal of Aircraft*, vol. 17, no. 8, pp. 554–560, 1980.

[80] W. Sullivan, J. Turnberg, and J. Violette, "Large-scale advanced prop-fan (lap) blade design," Tech. Rep. CR-174790, NASA, 1984.

Appendix A

Aerodynamic Design of a Sub-Scaled Ducted Fan

Nomenclature

c	=	Chord: length of stright line connecting LE to TE
FPR	=	Fan pressure ratio
i	=	Incidence angle: difference between the inlet and the leading edge meanline angle. i=$\beta_1 - \beta_1^*$ or $\alpha_1 - \alpha_1^*$
$\dot{m}_c$	=	Corrected mass flow rate
M	=	Mach number
P_0	=	Total pressure
T_0	=	Total temperature
α	=	Absolute air angle: angle between airstream and the axial direction
β	=	Relative air angle: angle between airstream and the axial direction
α^* or β^*	=	Meanline metal angle: angle between meanline at the blade edge (LE or TE) and the axial direction, α^* for stators and β^* for rotors
γ	=	Specific heat ratio, $\gamma = 1.4$ for air
δ	=	Deviation angle: difference between the exit air angle and the trailing edge meanline angle$\delta = \beta_2 - \beta_2^*$ or $\alpha_2 - \alpha_2^*$
η_{ad}	=	Adiabatic efficiency
η_p	=	Polytropic efficiency
λ	=	Blockage factor
ξ	=	Stagger angle: angle between the chord of a blade and the axial direction
ρ	=	Density
σ	=	Solidity: chord to circumferential distance (spacing) between two blades/ vane. $\sigma = c/S$, $S = 2\pi r/N$

ϕ = Camber angle: curvature of the meanline of an airfoil
(often expressed as $\beta_1^* - \beta_2^*$ or $\alpha_1^* - \alpha_2^*$)
$\bar{\omega}$ = Total pressure loss coefficient

A.1 NASA's Ultra-High Bypass Turbofans

Recent NASA investigations regarding the realistic simulation of gear turbofan noise (Source Diagnostic Test/ Advanced Ducted Propulsor) relied on rotors designed by General Electric Aircraft Engines (GEAE) such as depicted in Fig. A.1.

Figure A.1: 22 inch scale model of the Source Diagnostic Test (SDT) model fan installed in the 9-ft by 15-ft low speed wind tunnel at NASA Glenn from TM 2008-215415.

The fan is a $1/5^{th}$ scale model of a current technology turbofan engine, and represents a realistic baseline design for the ultra-high bypass class turbofan [22, 24, 25]. This new class of aeroengines includes Pratt and Whitney Gear Turbofan (GTF). The NASA fan referred to as the "R4" baseline fan, is 22 inches in diameter and has 22 blades. Its design stage pressure ratio is 1.47 (at 1,215 ft/s or $M_{tip} = 1.07$). The stator consists of 26 radial wide-cord vanes

and is known as the "Low count" OGV configuration. Similarly, the rotor of this present study is a scaled down version of General Electric's R4 fan combined with the "low-count" radial stator vanes [23].

A.1.1 Flowpath and Airfoil Specifications

A Wealth of literature were published about the geometry of the R4 rotor and low count stator set. Therefore, it is appropriate to initialize the baseline GTF design plan according to these references. Duct geometry of the inner (hub) and outer walls, aerodynamic and stacking line data for the rotor/stator blades were extracted from a NASA appendix (CR-2010-216898 Vol 1 & 3 by Morin). Fig. A.2a shows the coordinate system used to define the nacelle geometry. The z-direction is measured along the engine axis with z-values increasing from the inlet toward the exit. The axial location of the origin for convenience is at the blade stacking line. When viewed from the rear, the x-axis is horizontal with values increasing toward the right. Likewise, the y-axis is vertical with values increasing in the upward direction. The corresponding cylindrical coordinate system is defined such that the polar angle θ increases in the counter-clockwise direction when viewed from the rear.

A plot of the duct geometry is shown in Fig A.2b. The nose cone shown does not represent the actual nose cone geometry, but is merely an approximation to facilitate flow-field calculations. Thus, realistic nose cone coordinates were obtained from other NASA sources. A example of a table obtained from Morin's report containing the duct geometry in the cylindrical coordinates system is reproduced in Fig A.3.

In addition, Morin's coordinates files details the flow-path, and blade stacking geometry of the fan blades. A table containing the duct geometry in the cylindrical coordinates system is copied in Fig A.4. Airfoil Properties including chord, solidity, gap, and stagger are computed using the leading and trailing edge coordinates. Relations are:

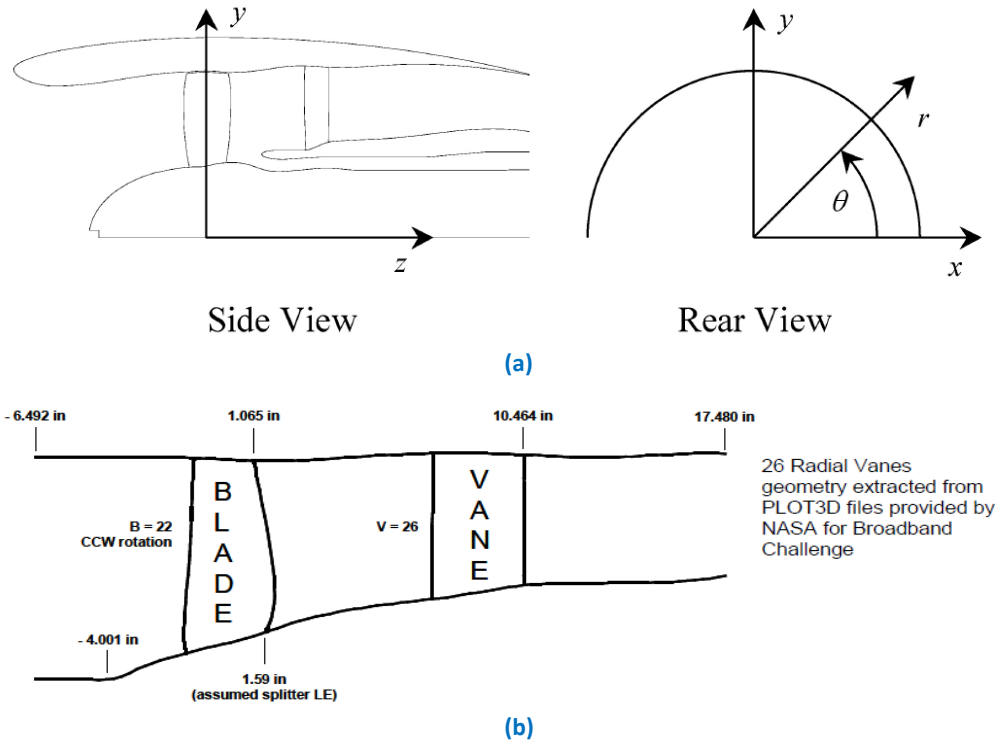

Figure A.2: (a) Engine coordinate system (b) cross-sectional view of the SDT model fan stage.

$$\text{chord}: \quad c = \sqrt{(x_{TE} - x_{LE})^2 + (y_{TE} - y_{LE})^2 + (z_{TE} - z_{LE})^2}$$

$$\text{airfoil gap}: \quad \tau = \frac{2\pi r_{LE}}{\#\text{ blades}}$$

$$\text{solidity}: \quad \sigma = \frac{c}{\tau}$$

$$\text{stagger}: \quad \xi = tan^{-1}\left(\frac{\sqrt{(r_{TE} - r_{LE})^2 + (z_{TE} - z_{LE})^2}}{r_{TE}\theta_{TE} - r_{LE}\theta_{LE}}\right)$$

However, the specifics of the airfoil profile were not included. Many of the scientific studies by NASA emphasized a generic selection of the blade section airfoil [60, 80]. This convention assumes a NACA 65-series airfoil. In addition, the thickness distribution of the airfoil sections was acquired by another NASA report [22]. A least curve fit was applied to the data points to yield the span-wise thickness distribution. Table A.1 summaries the references used in this report. With information regarding the aerodynamic profile, stacking

filedescr	Flowpath: Inside Diameter Wall - HUB				
nduct_h	90				
parmname	Axial				
zhub	-6.502327	-6.232568	-5.962808	-5.693049	-5.423289
	-5.153530	-4.883770	-4.614011	-4.344251	-4.074492
	-3.804733	-3.534973	-3.265214	-2.995454	-2.725695
	-2.455935	-2.186176	-1.916416	-1.646657	-1.376897
	-1.107138	-0.837379	-0.567619	-0.297860	-0.028100
	0.241659	0.511419	0.781178	1.050938	1.320697
	1.590456	1.860216	2.129975	2.399735	2.669494
	2.939254	3.209013	3.478773	3.748532	4.018291
	4.288051	4.557810	4.827570	5.097329	5.367089
	5.636848	5.906608	6.176367	6.446126	6.715886
	6.985645	7.255405	7.525164	7.794924	8.064683
	8.334443	8.604202	8.873961	9.143721	9.413480
	9.683240	9.952999	10.222759	10.492518	10.762278
	11.032037	11.301796	11.571556	11.841315	12.111075
	12.380834	12.650594	12.920353	13.190113	13.459872
	13.729631	13.999391	14.269150	14.538910	14.808669
	15.078429	15.348188	15.617948	15.887707	16.157467
	16.427226	16.696985	16.966745	17.236504	17.506264
parmname	Radius				
rhub	2.250805	2.250757	2.250756	2.250848	2.250945
	2.250908	2.250703	2.251318	2.250009	2.268878
	2.297416	2.372692	2.525183	2.674208	2.791127
	2.900357	3.002891	3.099274	3.189671	3.276292
	3.358367	3.435867	3.509917	3.581078	3.650682
	3.720369	3.794309	3.870063	3.969007	4.067281
	4.170762	4.275789	4.379734	4.479830	4.572974
	4.656779	4.721721	4.799961	4.862569	4.921029
	4.976265	5.029055	5.079441	5.127756	5.173022
	5.214911	5.251548	5.287234	5.322497	5.356940
	5.391048	5.429902	5.478404	5.524245	5.592687
	5.649140	5.699945	5.740850	5.772924	5.795676
	5.810992	5.821017	5.827940	5.831110	5.833467
	5.835088	5.836256	5.836969	5.836978	5.836439
	5.836241	5.837039	5.839078	5.843604	5.850944
	5.859892	5.875835	5.892634	5.916299	5.941113
	5.971287	6.001601	6.027731	6.073982	6.113209
	6.155001	6.196693	6.242894	6.289515	6.336137
blank					
filedescr	Primary Splitter: Inside Diameter Wall - UPPER				
nsplt_u	50				
parmname	Axial				
zsup	6.756294	6.975681	7.195069	7.414456	7.633843
	7.853230	8.072617	8.292004	8.511391	8.730778
	8.950166	9.169553	9.388940	9.608327	9.827714
	10.047101	10.266488	10.485875	10.705263	10.924650
	11.144037	11.363424	11.582811	11.802198	12.021585
	12.240972	12.460360	12.679747	12.899134	13.118521
	13.337908	13.557295	13.776682	13.996070	14.215457
	14.434844	14.654231	14.873618	15.093005	15.312392
	15.531780	15.751167	15.970554	16.189941	16.409328
	16.628715	16.848102	17.067489	17.286877	17.506264
parmname	Radius				
rsup	5.362028	5.389747	5.420494	5.457386	5.500269
	5.546825	5.594395	5.640565	5.683004	5.719951
	5.750893	5.775476	5.793916	5.807258	5.816899
	5.823565	5.828091	5.831034	5.833065	5.834527
	5.835635	5.836469	5.836996	5.836986	5.836640
	5.836273	5.836223	5.837216	5.839722	5.842403
	5.846898	5.854175	5.862836	5.875341	5.888147
	5.907170	5.926415	5.948395	5.972991	5.997588
	6.026151	6.058633	6.088115	6.118328	6.152295
	6.186142	6.222389	6.260305	6.298221	6.336137
blank					

Axial and radial coordinates for hub

Axial and radial coordinates for duct

Figure A.3: Sample fan casing geometry coordinate file.

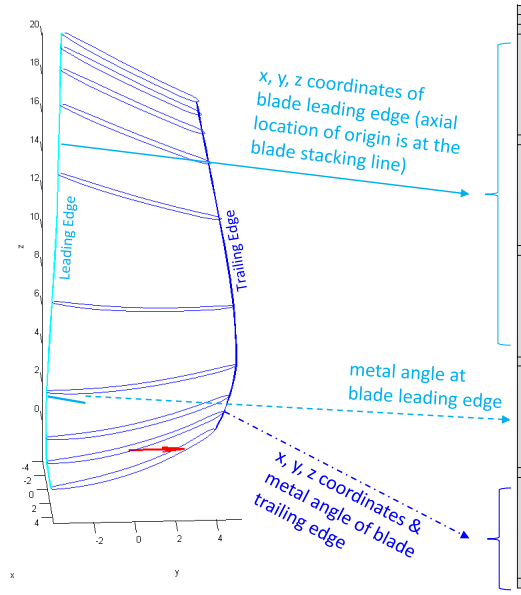

filedescr	NASA SOURCE DIAGNOSTICS FAN ROTOR AIRFOIL DATA				
numrle	51				
parmname	XLE				
xle	-3.300717	-3.303815	-3.308069	-3.313466	-3.320478
	-3.329237	-3.340175	-3.353832	-3.370878	-3.392150
	-3.419686	-3.451780	-3.493053	-3.544528	-3.608829
	-3.689264	-3.790090	-3.916614	-4.075167	-4.272249
	-4.520267	-4.828773	-5.215665	-5.700811	-6.305202
	-7.061386	-7.823350	-8.427942	-8.918634	-9.317997
	-9.638566	-9.894466	-10.098216	-10.260604	-10.390247
	-10.493849	-10.576728	-10.643064	-10.696187	-10.738648
	-10.772699	-10.799839	-10.821598	-10.839005	-10.852990
	-10.864068	-10.872978	-10.880105	-10.885885	-10.889806
	-10.893050				
parmname	YLE				
yle	0.056113	0.058546	0.061189	0.064622	0.069084
	0.074686	0.081611	0.090282	0.101076	0.114469
	0.131012	0.151285	0.175824	0.204902	0.238888
	0.278229	0.323901	0.353320	0.385976	0.442296
	0.516396	0.600291	0.691755	0.792650	0.902052
	1.099041	1.227651	1.360980	1.421185	1.429222
	1.423645	1.421548	1.426293	1.439713	1.441808
	1.448014	1.453255	1.457092	1.459912	1.462011
	1.463594	1.464802	1.465734	1.466459	1.467026
	1.467472	1.467826	1.468104	1.468316	1.468480
	1.468602				
parmname	ZLE				
zle	-1.297397	-1.297990	-1.298759	-1.299756	-1.301048
	-1.302684	-1.304649	-1.307122	-1.310177	-1.313938
	-1.318526	-1.324082	-1.330689	-1.338260	-1.346618
	-1.354728	-1.359192	-1.361948	-1.360299	-1.357423
	-1.351905	-1.328906	-1.312679	-1.274927	-1.226997
	-1.165948	-1.118212	-1.100427	-1.086892	-1.072864
	-1.064589	-1.060213	-1.057601	-1.056210	-1.052801
	-1.049800	-1.046823	-1.043761	-1.041383	-1.039327
	-1.037684	-1.036288	-1.035179	-1.034292	-1.033560
	-1.032978	-1.032611	-1.032136	-1.031847	-1.031624
	-1.031459				
parmname	BETATE1				
betale	66.841801	66.815885	66.783103	66.742593	66.693989
	66.614494	66.518115	66.399710	66.240933	66.023458
	65.730624	65.367511	64.838772	64.115849	63.165000
	61.994470	60.605418	59.429298	58.195041	56.664610
	54.802715	53.044276	51.019794	48.938041	46.809141
	43.971135	41.697607	39.574998	38.057755	36.881772
	35.808748	35.100205	34.436097	33.761993	33.149026
	32.649980	32.246985	31.915624	31.643211	31.425093
	31.245762	31.101723	30.986598	30.895777	30.819186
	30.759661	30.714022	30.676131	30.646688	30.624129
	30.608167				
parmname	XTE				
xte	-4.089949	-4.092835	-4.097195	-4.103248	-4.111110
	-4.120894	-4.132927	-4.147878	-4.166385	-4.189279
	-4.217576	-4.252514	-4.295610	-4.348718	-4.414104
	-4.494511	-4.593260	-4.714419	-4.862988	-5.045069
	-5.268126	-5.541716	-5.878458	-6.292905	-6.801577
	-7.431093	-8.067842	-8.579260	-8.995760	-9.329889
	-9.620321	-9.846050	-10.027071	-10.172226	-10.288950
	-10.382961	-10.459827	-10.520140	-10.569674	-10.609668
	-10.641939	-10.667974	-10.689969	-10.708896	-10.725843
	-10.740546	-10.739413	-10.746562	-10.752061	-10.756291
	-10.759548				
parmname	YTE				

Figure A.4: Airfoil Leading and Trailing edge coordinate convention (left). Sample fan geometry coordinate file (right).

characteristics, and airfoil geometry data, a realistic rotor can be synthesized. However, the gear turbofan configuration must be properly sized to fit the constraints of our lab.

Table A.1: Summary of sources and details used

Author	Reference	Information Obtained
Morin	NASA/CR-2010-216898/VOL1 NASA/CR-2010-216898/VOL3	Duct geometry Chord distribution
Hughes	NASA/TM-2005-211681	Spanwise airfoil thickness ratio
Lieblein	NASA-SP-36	NACA 65-series airfoil

A.2 Scaling of UCI Ducted Fan

Early discussion of simulating realistic ducted fan noise involved scaling. How large can our mini-fan be? To accurately replicate the realistic acoustics and aerodynamics, our sub-scale model must match the full-scale tip speeds. It should be realized that rotating a small scale rotor with a tip speed of 700 feet per second (60 percent of design speed) or approximately 60,000 RPM is a difficult proposition fraught with safety and feasibility concerns. This stringent requirement means extremely powerful, compact and sophisticated brushless motors are required. Nevertheless, electric motors only output so much power. Too large of a rotor diameter, the rotor would simply spin too slowly. Too small of a rotor diameter, the rotor would not be operating near its peak efficiency (not impedance matched). Thus, sizing of the fan was constrained by the power capacity of the brushless motors, which was Neu Motors Model 1530-1.5D. This motor achieves a maximum power of 5000 Watts (6.7 HP).

To gain an understanding of the overall process, it is useful at first to study a highly simplified model. We use the laws of thermodynamics and fluid mechanics to explain the behavior of our micro air-breathing engine. The purpose is to estimate the best possible engine performance as a function of principal design parameters- maximum allowable pressure ratio, and fan diameter for a given power level.

Fig. A.5 illustrates our simple thermodynamic model. Let's assume that all components except the fan are reverisble and adiabatic. Since the fan pressure ratio FPR is

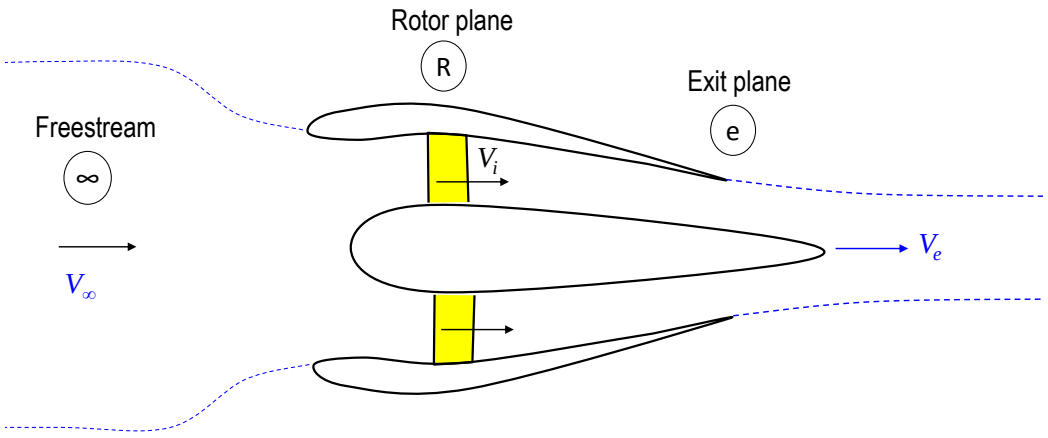

Figure A.5: Schematic of model ducted fan engine.

specified, we can determine the outlet stagnation pressure from

$$FPR = \frac{p_{0e}}{p_{0\infty}} \qquad \leftrightarrow \qquad p_{0e} = FPR * p_{0\infty} \tag{A.1}$$

and the outlet stagnation temperature from

$$T_{0e} = T_{0\infty}\left[1 + \frac{1}{\eta_{ad}}\left(FPR^{\frac{\gamma-1}{\gamma}} - 1\right)\right] \tag{A.2}$$

in which γ is the specific heat ratio (assumed constant) for the compression process and η_{ad} is the fan adiabatic efficiency. The outlet stagnation temperature was obtained using the definition of fan adiabatic efficiency

$$\eta_{ad} = \frac{(h'_{0e} - h_{0\infty})_{ideal}}{(h_{0e} - h_{0\infty})_{actual}} \qquad where \qquad \frac{T'_{0e}}{T_{0\infty}} = \left(\frac{p_{0e}}{p_{0\infty}}\right)^{\frac{\gamma-1}{\gamma}} = FPR^{\frac{\gamma-1}{\gamma}} \tag{A.3}$$

It is defined as the enthalpy (temperature) rise that would be obtained in a compressing a gas isentropically from an initial to a final conditions divided by the actual enthalpy (temperature) rise observed. More simply, it is the ratio of the ideal enthalpy change to the actual enthalpy change. The efficiency characterize effect of irreversiblies on the process of compression which lowers the stagnation pressure at the stagnation pressure than if the

compression was isotropic. For well-designed engines efficiency range from $0.85 < \eta < 0.90$.

We may write the exhaust mach number as

$$M_e = \sqrt{\frac{2}{\gamma - 1}\left[\left(\frac{p_{0e}}{p_e}\right)^{\frac{\gamma-1}{\gamma}} - 1\right]} \tag{A.4}$$

as long as the nozzle exit flow is unchocked, i.e. the exhaust pressure p_e is equal the ambient pressure $p_e = p_\infty$. Exhaust properties are determined from the speed of sound, and ideal gas relations

$$\begin{aligned} T_e &= \frac{T_{0e}}{1 + \frac{\gamma-1}{2}M_e^2} \\ V_e &= M_e\sqrt{\gamma R T_e} \\ \rho_e &= \frac{p_e}{RT_e} \end{aligned} \tag{A.5}$$

The thrust is the time rate of momentum (momentum flux) acting on the control volume

$$T = \dot{m}_e(v_e - v_\infty) \qquad\qquad \dot{m}_e = \rho_e V_e A_e \tag{A.6}$$

Power that is inputted by the fan into the fluid is the net rate of increase of energy stored in the control volume. That is, the difference of the enthaplies (thermal energy plus flow work, $h = e + pv$) times the mass flow rate

$$\begin{aligned} P &= \dot{m}_e(h_{0e} - h_{0\infty}) \\ &= \dot{m}_e c_p(T_{0e} - T_{0\infty}) \qquad\qquad C_p = 1004\ J/_{Kg-K} \end{aligned} \tag{A.7}$$

A excel data sheet permitted optimization of the rotor diameter for the available power of the high-performance DC motor. Accordingly, a nacelle with an inlet diameter of 70 mm and exit-to-inlet area ratio of 0.56 was selected. The rotor and stator counts were 14 and 24, respectively, giving a rotor-stator ratio of 0.58. In addition the chord (solidity) have

increased by a multiple of 1.3. These relatively low counts were selected for manufacturing considerations; however, having gained experience with the manufacturing process, higher counts will be possible in the future.

Table A.2: Ducted fan specifications

	Parameter	**Specifications**
Nacelle	Fan inlet diameter	70.0 mm
	Fan exit diameter	71.0 mm
	Nacelle exit to inlet area ratio	0.56
	Design fan pressure ratio	1.15
	Input power	5.0 kW (6.7 hp)
Rotor	Overall design	Based on GE R4 fan
	Count	14
	Diameter	69.2 mm (0.4 mm tip clearance)
	Design RPM	57000
	Design Tip Mach	0.61
	Hub-to-Tip ratio	0.42
	Blade Airfoil	NACA 65-series
	Blade Thickness/Chord Ratio	0.081 (hub) to 0.028 (tip)
Stator	Overall design	Radial vane, based on low-count SDT configuration
	Count	24
	Solidity	2.21 (hub) to 1.04 (tip)
	Blade Airfoil	NACA 65-Series
	Blade Camber	42.2 ° (hub) to 40.6 ° (tip)
	Blade Thickness/Chord Ratio	0.0707 (hub) to 0.0698 (tip)

The following section chronicles the development of the rotor geometry.

A.3 Blade Calculation Procedure

This section describes the calculation method, experimental data sets, and governing equations used in the aerodynamic design of a ducted fan blade. Since many concerns must be addressed without sacrificing weight or efficiency, the design of design of our mini-fan is a great challenge. The process begins with non-negotiable characteristics that the compressor must meet as documented in table A.3.

The need for simulation of the flow field within the compressor will be examined by a

Table A.3: Design Specifications

Fan Pressure Ratio	$FPR = 1.15$
Inlet Total Pressure and Temperature	$P_0 = 101325$ Pa, $T_0 = 293$ K
Physical Speed	$\Omega = 57{,}000$ RPM
Hub to tip ratio	0.42
Exit to rotor Area ratio	$\sigma = 0.56$
Rotor casing diameter	70 mm
Blade count	14
Physical mass flow rate	$\dot{m}_p = 0.3307\ kg/m^3$
Exit Mach number	$M_{exit} = 0.452$
Chord multiplier	1.3
Thickness ratio at meanline	8.0 %

variety of computerized methods of differing complexity. Before employing complex, numerically expensive techniques, preliminary design and layout of the compressor involves working first with simple one-dimensional mean-line analysis.

The mean-line methodology establishes the approximate velocity triangles, and the machine size resulting from the various design assumptions. Our consideration here is with the compressor operating under design values of shaft speed and mass flow rate. Next, the radial variation of hub and tip contours through the fan is determined. The blading is selected to satisfy the design-point velocity diagrams and to obtain high efficiency. Lastly, a commercial computational fluid dynamics (CFD) solver was utilized for the refinement and verification of our meanline analysis model. Our purpose is to bring together reasonably simple, yet representative models and ideals so that empirical, theoretical, and computational methods work together toward achieving the best possible performance. To summarize the design of the six-stage axial flow compressor is divided into 3 steps:

1. Mean-Line Analysis

2. Radial Equilibrium and generation of rotor blade

3. Computational Fluid Dynamics

A.3.1 Mean-Line Analysis

The first part of the design involves the determination of the various air velocities and flow angles, to best achieve the design point requirement of the compressor. A MATLAB code was developed to calculate the velocity triangles, thermodynamic and aerodynamics parameters at the various compressor stations. The mean radius (or root mean square radius r_{rms}) is used in the calculations to determine the blade speed. Fig. A.6 illustrates the stations along the flow path. This algorithm addresses the need for quick calculations, and sizing of the axial compressor. The mean-line method assumes that the radial velocity components are negligible, such that the average axial velocity is approximately the same between stations. A change in radius in between the blade rows does not alter the calculation profoundly. With a handful of design specifications, all of the key components are solved using simple, algebraic, yet representative physical models of the fluid dynamics inside the compressor. This preliminary design will make up a large proportion of the delivered design.

The mean-line approach requires various design assumptions to establish the approximate velocity triangles, aerodynamic and thermodynamic properties. Assumptions are as follows:

1. No swirl at inlet and exit of fan.
2. Blockage factor, $\lambda = 0.99$ at the inlet which linearly varies to 0.97 at the compressor exit based on backhand calculations.
3. The flow follows the compressor blades perfectly, deviation (δ) and incident (i) angles were determined iteratively using smooth-flow incident angle and Carter's Rule.

A schematic for the mean line (one-dimensional) calculation process is illustrated in Fig A.7. Before the calculations can begin, the inlet and exit conditions are determined. This

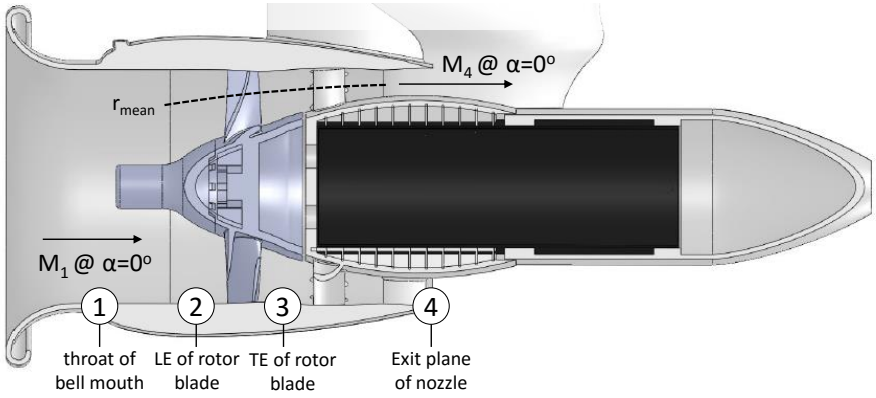

Figure A.6: Station locations of our ducted fan simulator.

inflow and outflow conditions will contain the properties and overall design of the compressor. The mean/ root mean squared radius (the average radius between the hub and casing/ rms radius) is used in the calculations to determine the tangential blade speed. The mean radius varies according to the geometry of the nozzle. The calculations are divided into two steps depending on whether it is a rotor or stator. First the code compute the properties at the rotor inlet required for the specified fan pressure ratio (FPR) and adiabatic efficiency (η_{ad}). In the next step, the solution is marched downstream to a position between the rotor and stators. Loss coefficients are included in the calculation to relate the fluid turning angles to the stagnation pressure loss due to friction. The stagnation total pressure loss for the rotor and stator are:

$$\bar{\omega}_{rotor} = \frac{P^r_{0,in} - P^r_{0,out}}{P_{0,in} - P_{static,in}} \qquad \bar{\omega}_{stator} = \frac{P_{0,in} - P_{0,out}}{P_{0,in} - P_{static,in}} \tag{A.8}$$

These are written for the rotor in terms of relative total pressure, and for the stator in terms of absolute total pressure. Thus, pressure losses through the stator involves replacing the relative total pressure ($P^r_0 = P_{static}(1 + 0.2M^2_{rel})^{3.5}$), with the absolute total pressure ($P_0 = P_{static}(1 + 0.2M^2_{abs})^{3.5}$). At design conditions the loss coefficient is, $\bar{\omega} = 0.04$. The resulting mean-line + loss coefficient computation determines the resulting pressure ratio of the entire compressor. To be able to have the desirable total pressure ratio FPR after the

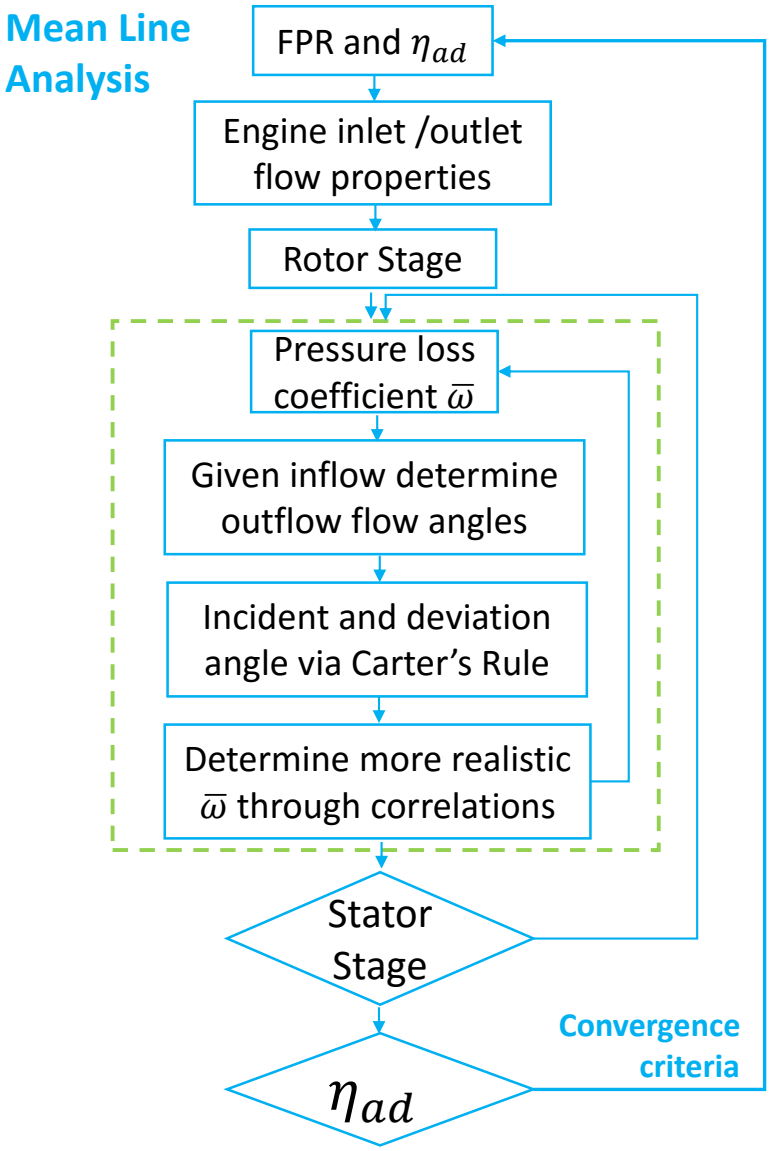

Figure A.7: Structure of meanline iteration procedure over the entire compressor.

calculation is done, it is necessary to adjust the compressor efficiency (η_{ad}). Put another way, the efficiency is adjusted to obtained the design point overall pressure ratio FPR. The following sections develops the expressions utilized in the meanline code. The algorithm can be broken down into calculations at the:

1. Inlet station
2. Nozzle exit station
3. Rotor station and then Stator station

Inflow Calculation Steps

Given the casing and hub profile, the root mean squared mean radius is

$$r_{rms} = \left(\frac{r_{case}^2 + r_{hub}^2}{2} \right)^{\frac{1}{2}} \tag{A.9}$$

the physical area

$$A_{phy} = \pi (r_{case}^2 - r_{hub}^2) \tag{A.10}$$

velocity of rotor at pitch line

$$U_{rms} = \frac{r_{rms} \pi RPM}{30} \tag{A.11}$$

the mach number at station 1 and 2 is obtained from

$$\frac{\dot{m}_p \sqrt{T_0}}{P_0 A_{phys} \lambda} = \sqrt{\frac{\gamma}{R}} \left[\frac{M}{(1 + \frac{\gamma - 1}{2} M^2)^{\frac{\gamma+1}{2(\gamma-1)}}} \right] \tag{A.12}$$

For a given total temperature/pressure (isotropic through inlet), and blockage ratio- the Mach number is solved implicitly. λ is the blockage factor- the ratio of effective flow area to physical area.

$$\lambda = \left(1 - \frac{A_{eff}}{A_{phy}} \right) x100\%$$

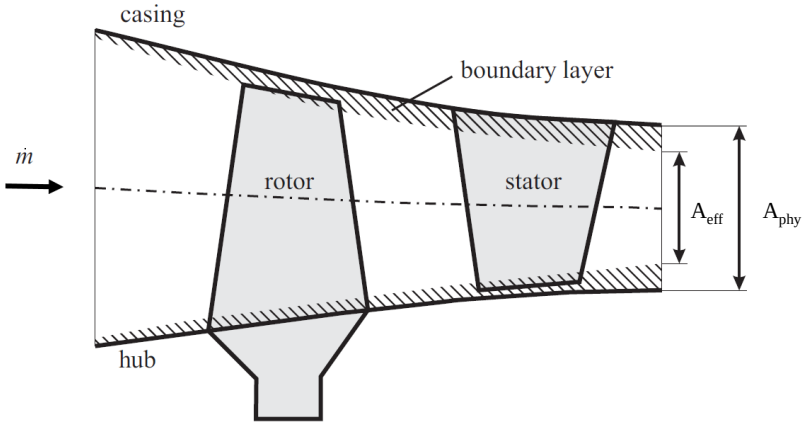

Figure A.8: Casing boundary layer growth and modeling.

This factor accounts for the area losses generated by the end walls due to the growth of the casing boundary layer. The formation, and development of these boundary layer block or reduce the physical area in which the flow can travel. A cartoon of end wall loses can be view in Fig A.8. Calculation of the inlet Mach number allows for determination of static thermodynamic variables

$$T_{static} = \frac{T_0}{1 + \frac{\gamma+1}{2}M^2} \qquad p_{static} = \frac{P_0}{(1 + \frac{\gamma+1}{2}M^2)^{\frac{\gamma}{\gamma-1}}} \tag{A.13}$$

$$a = \sqrt{\gamma R T_{static}} \qquad c = Ma \qquad \rho = \frac{p_{static}}{RT_{static}} \qquad \rho_0 = \rho\Big(1 + \frac{\gamma-1}{2}M^2\Big)^{\frac{\gamma}{\gamma-1}}$$

where a,c are the local speed of sound, and absolute velocity (flow velocity in the absolute frame of reference), respectively.

Nozzle Exit Calculation Steps

Overall temperature ratio

$$OTR = \frac{FPR^{\frac{\gamma-1}{\gamma}} - 1}{\eta_{ad}} + 1 \tag{A.14}$$

where η_{ad} is the adiabatic efficiency. It first value is approximated, and then a new value is calculated to adjust the approximated first value. This process iterates until η_{ad} converges as illustrated in Fig. A.7. The total temperature for last stage (station 4) is

$$T_0[4] = OTR * T_0[2] \tag{A.15}$$

the shaft work that must be supplied to drive the fan normalized by fan angular velocity is a function of the flow turning ($\Delta(rc_u)$) across the rotor in the absolute reference frame

$$\Delta(rC_u) = \frac{W}{\omega} = \frac{C_p \Delta T}{\pi * RPM/30} \tag{A.16}$$

Polytropic (or small-stage) efficiency is defined as the ratio of the energy which contributes to the pressure rise to the total energy delivered to the compressor. Polytropic efficiences are generally used to compare one compressor with another since it is independent of FPR.

$$\eta_p = \frac{\gamma - 1}{\gamma} \frac{ln(FPR)}{ln(OTR)} \tag{A.17}$$

Total pressure at nozzle exit is determined from

$$P_0[4] = P_0[2] * (OTR)^{\frac{\gamma \eta_p}{\gamma - 1}} \tag{A.18}$$

the prescribed exit mach number, M_4, and exit total temperature ($T_0[4]$) yield the static properties

$$T[4] = \frac{T_0[4]}{1 + \frac{\gamma-1}{2} M_4^2} \qquad a[4] = \sqrt{\gamma R\, T[4]} \qquad C[4] = M_4\, a[4]$$

Rotor and Stator Calculation Steps

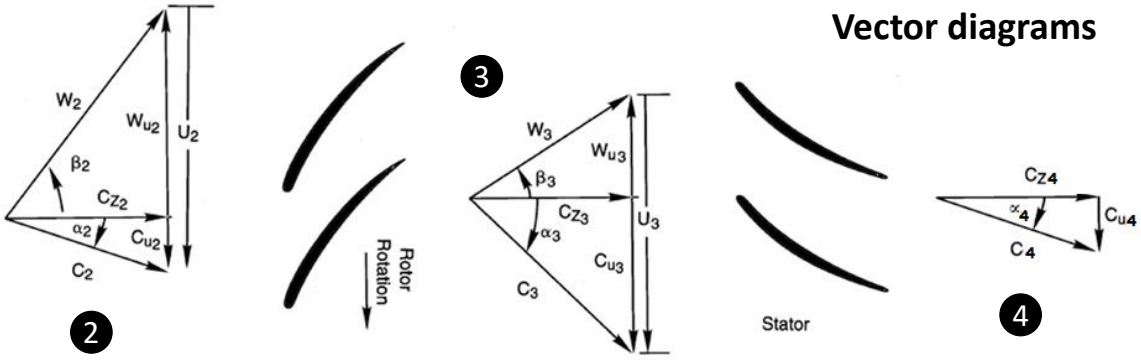

Figure A.9: Velocity triangle at meanline for the rotor inlet, interstage, and stator exit.

To calculate the static properties of the working fluid at the rotor inlet, the absolute velocity, $C[2]$ is required. With the aid of the velocity diagram, see Fig. A.9, the relative and the absolute velocity can be found, as well as the relative flow angle, $\beta[2]$.

$$C_u[2] = C[2] \tan(\alpha_2) \qquad W_u[2] = U_{rms}[2] - C_u[2] \qquad \beta[2] = \tan^{-1}\left(\frac{W_u[2]}{C_z[2]}\right) \tag{A.19}$$

The properties of the gas as seen by the rotor in the relative frame of reference are computed from the static properties of the gas, which do not change when transferring between reference frame.

$$W[2] = \frac{C_z[2]}{\cos\left(\beta[2]\right)} \qquad M_{rel} = \frac{W[2]}{a[2]} \qquad P_0^r[2] = P_{static}[2]\Big(1 + \frac{\gamma - 1}{2} M_{rel}^2\Big)^{\frac{\gamma}{\gamma-1}} \tag{A.20}$$

To move from the rotor-inlet towards the outlet of the rotor the rotor exit absolute flow angles ($\alpha[3]$) must be known. The rotor exit flow angle determines the incident (i) and deviation (δ) angles and loss coefficient ($\bar{\omega}$) which also depends on i, δ. This highly coupled system is solved using iteration. As illustrated in Fig. A.7 this procedure is composed of 3 main sub-calculations:

1. Determination of outflow angles
2. Determination of incident and deviation angles
3. Determination of more realistic loss coefficient $\bar{\omega}$

1. Absolute flow angle

The absolute mach number at the rotor exit (station 3) is

$$\frac{\dot{m}_p \sqrt{T_0[3]}}{P_0[3] A_{phys}[3]\ \lambda[3]} = \sqrt{\frac{\gamma}{R}} \left[\frac{M}{(1 + \frac{\gamma-1}{2} M^2)^{\frac{\gamma+1}{2(\gamma-1)}}} \right] \tag{A.21}$$

with static properties

$$T_{static}[3] = \frac{T_0[3]}{1 + \frac{\gamma-1}{2} M[3]^2} \qquad a[3] = \sqrt{\gamma R T_{static}[3]} \qquad c[3] = M[3]\ a[3]$$

For the specified FPR the flow properties are

$$C_u[3] = \frac{\Delta(rC_u) + r_{rms}[2]C_u[2]}{r_{rms}[3]} \qquad W_u[3] = U_{rms}[3] - C_u[3] \qquad \alpha[3] = \sin^{-1}(\frac{C_u[3]}{C[3]})$$

For typical multistage compressor design, the above step require iteration where a initial guess of the rotor exit absolute flow angle is made and checked until the associated stage work (ΔrC_u) converge to the required for design- since the hub geometry is unknown. Here, knowing the duct geometry simplifies the computation. For the absolute flow angle (α) the properties at the end of rotor are

$$C_z[3] = C[3]\cos(\alpha[3]) \qquad W[3] = \sqrt{C_z[3]^2 + W_u[3]^2} \qquad M_{rel} = \frac{W[3]}{a[3]}$$

The relative total pressure and static pressure is

$$P_0^r[3] = P_0^r[2] - \bar{\omega}_{rotor}(P_0^r[2] - P_{static}[2]) \qquad P_{static}[3] = \frac{P_0^r[3]}{(1 + \frac{\gamma-1}{2}M_{rel}[3]^2)^{\frac{\gamma}{\gamma-1}}}$$

Note the stagnation pressure loss coefficient $\bar{\omega}$ depends on i, δ. For the first loop, we use the design point loss coeffient $\bar{\omega} = 0.4$. Thus, iteration is required to get an realistic coefficient.

2. Incidence and deviation angle

For internal flows, the incident angle (i) is comparable to the angle of attack (α). The incidence angle is the difference between the blade angle and the flow angle as sketched in right illustration in Fig. A.12. The deviation angle is the difference between the air angle and the mean line angle at the trailing edge. Imagine a cascade operating under design conditions draw in the right panel in Fig A.12. As the inlet flow angle β_i increase the outflow angle β_{ii} remains essentially constant until the inflow is too steep for the flow to follow the surface of the airfoil. Boundary layer separation takes place due to the adverse pressure gradient on the suction surface of the blades. A separation region forms, increasing total pressure

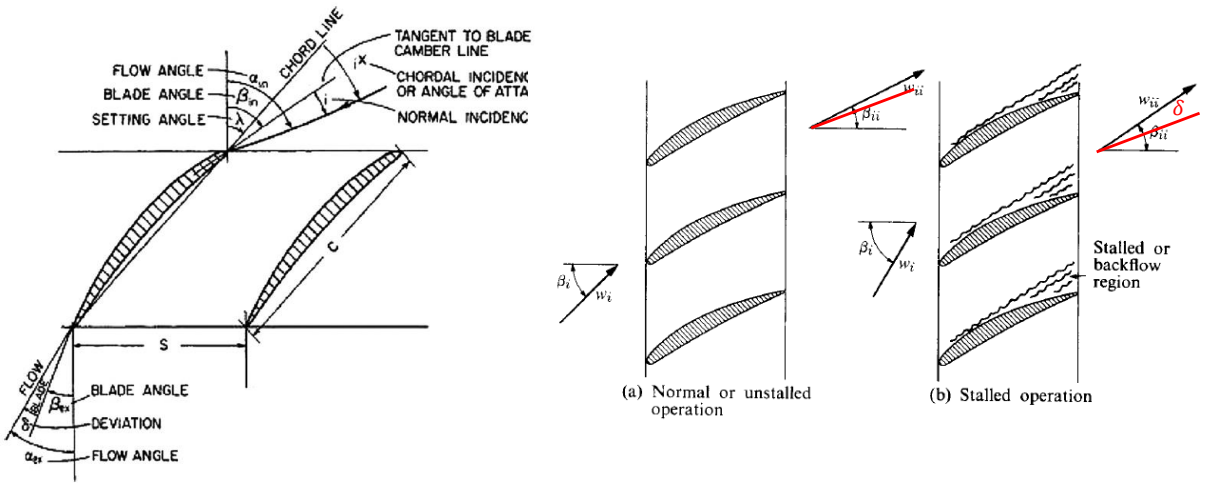

a) Definition of airfoil parameters

b) Cascade Stall and changes in deviation angle

Figure A.10: Incidence and deviation angle and definition of reference incidence/deviation angle.

loss due to turbulent mixing, and viscous effects. Since the streamlines no longer follow the surface, the outflow angle β_{ii} increases. A corresponding adjustment to the deviation angle occurs.

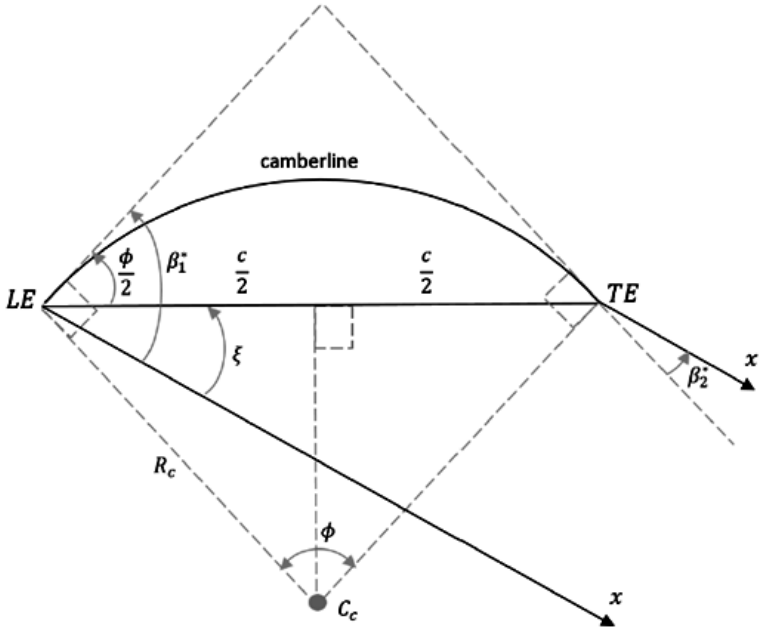

Figure A.11: Circular arc camber line design.

The airfoil was designed by using the simplistic method where the camber line is established as an arc of a circle as drawn in Fig A.11. To formulation of the camberline requires the determination of the blade angles. This requires an iteration scheme. Fortunately, a circular arc meanline drastically simplifies the relationship between stagger angle (ξ), camber angle (Φ), and incident angle (i). In this case the camber angle is estimated. Then the incidence and deviation angles can be found; from the incidence and deviation angle a new camber angle is calculated. This process is repeated until no changes in incidence and deviation angles are calculated. In other words, they converge. A schematic of the iterative process is shown in the figure A.12.

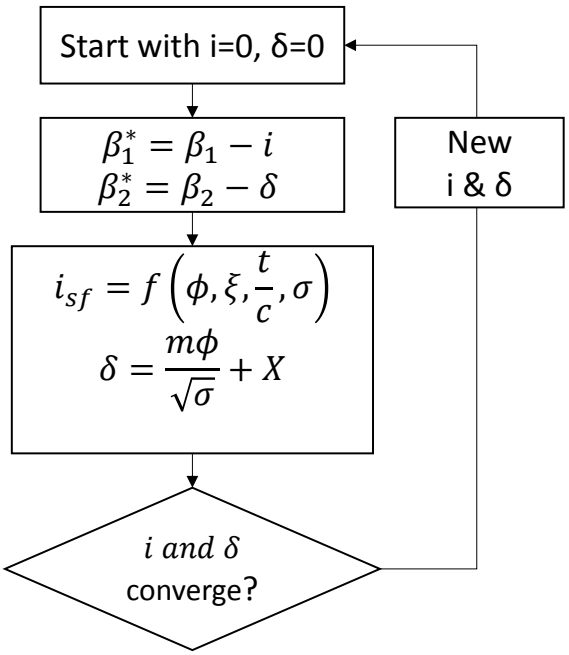

Figure A.12: Iterative algorithm for calculation of the blade angles and corresponding meanline.

This approach utilize two experimental or theoretical correlations. At the leading edge, the smooth flow incidence angle relationship is used. This correlation assumes a potential flow through a two-dimensional cascade flow where the stagnation streamline attaches directly to the leading edge of the airfoil. This particular smooth flow field will induce minimum loss, and the incidence angle is term the smooth-flow incidence angle. Thus, the smooth flow

incidence angle is used as a design guide for subsonic blading:

$$i_{sf} = A_1 + \frac{\Phi}{\sqrt{\sigma}}[A_2 + A_3\xi + A_4\xi^2] + \frac{t}{c}[A_5\sigma + A_6\sigma^2 + A_7\phi + A_8\sigma\Phi] + \Phi[A_9\Phi + A_{10}\sqrt{\sigma} + A_{11}] + A_{12}\sqrt{\sigma}$$

Where $A_n, i_{sf}, \Phi, \xi, \sigma, \frac{t}{c}$ are empirical constants, smooth flow incidence [deg], camber angle ($\beta_1^* - \beta_2^*$ for rotor, $\alpha_1^* - \alpha_2^*$ for stator [deg]) , stagger angle, ($\frac{1}{2}$ ($\beta_1^* - \beta_2^*$) for rotor, $\frac{1}{2}(\alpha_1^* - \alpha_2^*)$ for stator [deg]), solidity, thickness to chord ratio respectively. On the other hand, the deviation angle is correlated using Carter's rule:

$$\delta = \frac{m\Phi}{\sqrt{\sigma}} + X \qquad\qquad m = 0.216 + 8.75x10^{-4}\xi + 2.625x10^{-5}\xi^2$$

where m, and X are the deviation coefficient and empirical adjustment from test data. At the meanline the empirical factor is given as $X = 1°$.

3. Loss coefficient

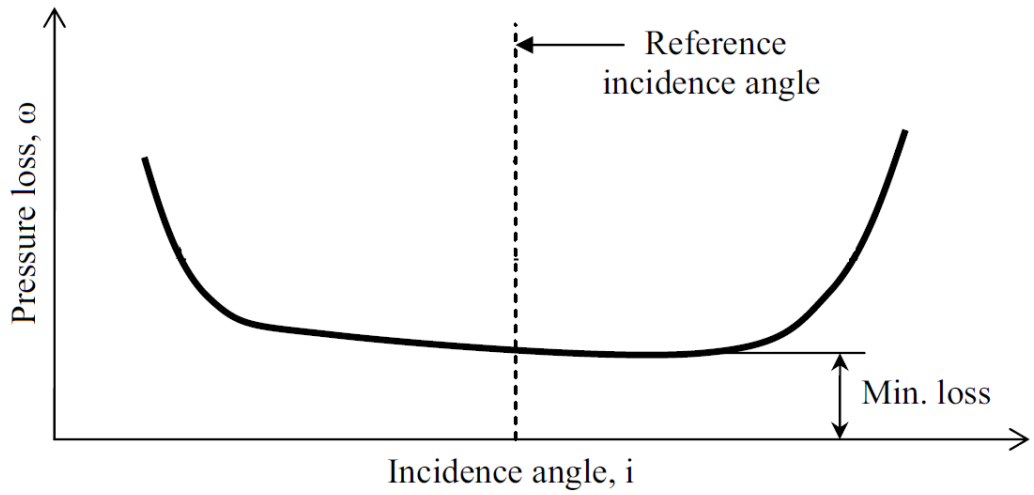

Figure A.13: Definition of experimental reference incidence angle.

The last step in the rotor is to calculate the entropy rise due to the losses throughout the rotor. In the beginning of the rotor calculation a approximation was made for the entropy rise. It must be corrected by calculation of the true entropy rise. Experimental studies on a

given cascade, format their results according to a reference incidence (i_{ref}) when testing at different inflow flow angles. The total pressure loss coefficient depends on incidence angle. Mirroring drag, the loss coefficient $\bar{\omega}$ will increase for both positive and negative incidence angles. The minimum total pressure loss occurs at the reference incidence angle according to Fig. A.13. In NASA report N65-23345, Chapter VI- "Experimental Flow in 2D Cascade", Lieblin proposed the correlation for reference incidence angle as

$$i_{ref} = (K_i)_{sh}(K_i)_t(i_0)_{10} + n\Phi$$

Where K_{sh} and K_t are corrections that accounts for blade shape and thickness. For a NACA 65-Series $K_{sh} = 1.0$. and the thickness correction K_t, is determined from an least square cubic curve fit as:

$$(K_i)_t = -0.0214 + 19.17\left(\frac{t}{c}\right) - 122.3\left(\frac{t}{c}\right)^2 + 312.5\left(\frac{t}{c}\right)^3$$

Φ is the camber, $(i_0)_{10}$ is the reference incidence angle for a zero camber 10% thick NACA 65-A10, and n is the incidence angle slope factor. Linear regression of the data set yields:

$$(i_o)_{10} = (0.0324 - 0.0674\sigma) + (-0.002364 + 0.0913\sigma)\beta_1 + (1.6x10^{-5} - 2.38x10^{-4}\sigma)\beta_1^2$$

$$n = (-0.063 + 0.02274\sigma) + (-0.0035 + 0.0029\sigma)\beta_1 - (3.79x10^{-5} + 1.11x10^{-5}\sigma)\beta_1^2$$

Graphs of the thickness correction $(K_i)_t$, zero-camber incidence angle $(i_o)_{10}$, and the incidence angle slope factor n are plotted in Fig. A.14-A.15.

Lieblin recommend a similar structure to that of the reference deviation angle. The reference deviation angle (δ_{ref}) is

$$\delta_{ref} = (K_\delta)_{sh}(K_\delta)_t(\delta_0)_{10} + m\Phi$$

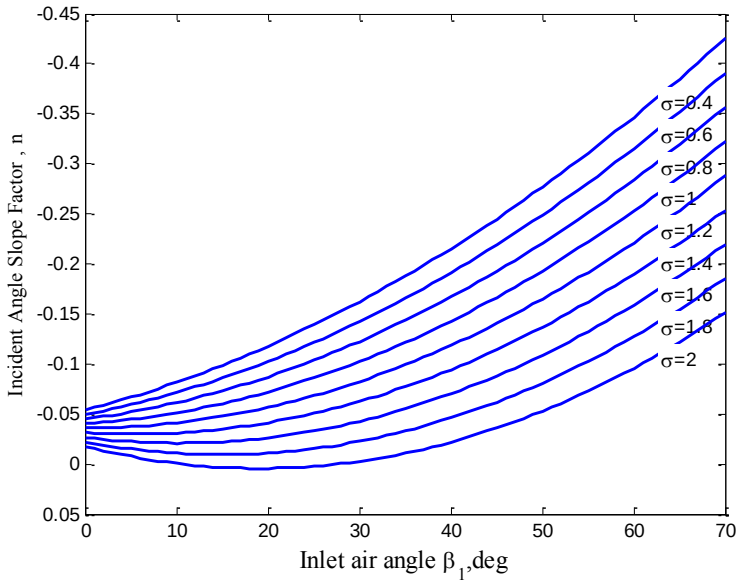

Figure A.14: Reference incidence slope factor for 10 % thick NACA 65-A10.

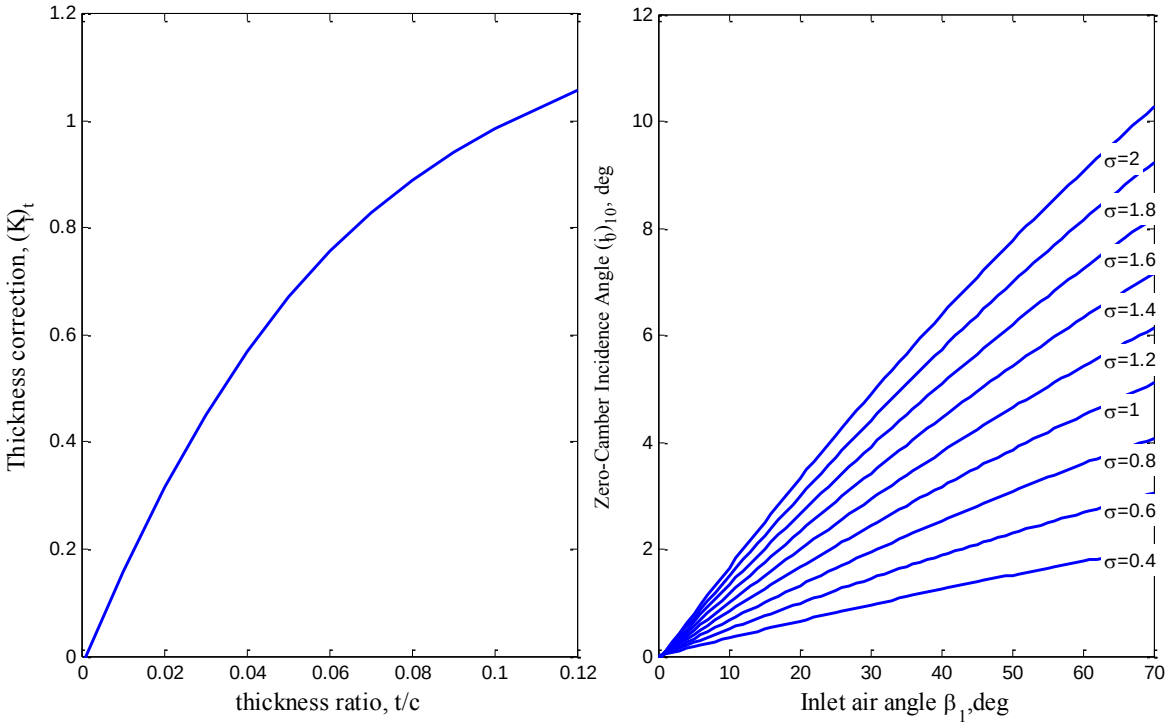

Figure A.15: a) Reference incidence angle thickness correction for 10 % thick NACA 65-A10. b) Reference incidence angle for zero camber for 10 % thick NACA 65-A10.

Where the nomenclature is similar except all corrections are for the deviation angle, δ. Similarly, the shape factor $(K_\delta)_{sh}$ uses the same constant as $(K_i)_{sh}$. The thickness correction

$(K_\delta)_t$ as a function of thickness ratio is given by another curve fit:

$$(K_\delta)_t = 0.0142 + 6.172\left(\frac{t}{c}\right) + 36.61\left(\frac{t}{c}\right)^2$$

$(\delta_0)_{10}$ is the reference deviation angle for zero camber 10 % thick NACA 65-A10.

$$(\delta_0)_{10} = (-0.0443 + .1057\sigma) + (0.0209 - .0186\sigma)\beta_1 + (-4.0x10^{-4} + 7.6x10^{-4}\sigma)\beta_1^2$$

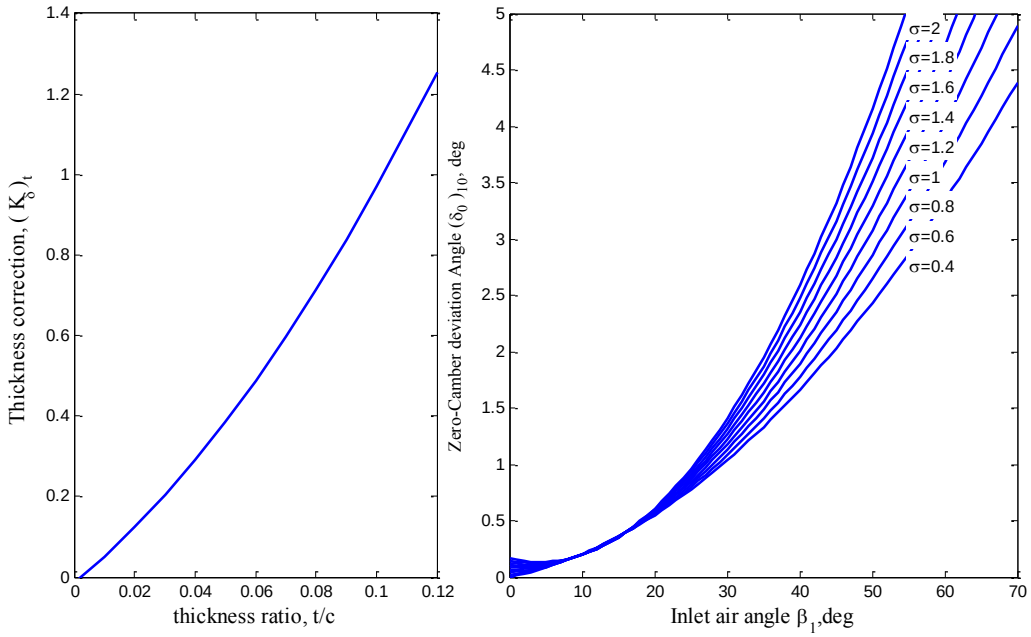

Figure A.16: a) Thickness correction for deviation angle for 10 % thick NACA 65-A10. b) zero-camber deviation Angle for 10 % thick NACA 65-A10.

Graphs of the thickness correction, zero- camber deviation angle and the incidence angle slope factor are shown Fig. A.16.

The variable m is comparable to n for the incident angle expression. m represent the deviation slope factor, and is more complex mathematically than n.

$$m = \frac{m_{(\sigma=1)}}{\sigma^b}$$

Where $m_{(\sigma=1)}$, the modified slope factor represents the value of slope factor, m for a cascade

with solidity, σ=1, and b is the exponent for deviation angle. Best fit of the data series gives:

$$m_{(\sigma=1)} = 0.17 - 3.33x10^{-4}(\beta_1 - 0.1\beta_1^2)$$

$$b = 0.9655 + 2.538x10^{-3}\beta_1 + 4.221x10^{-5}\beta_1^2 - 1.3x10^{-6}\beta_1^3$$

Fig A.17 plots the modified slope factor for cascade σ=1, the exponential factor b, and the slope factor m.

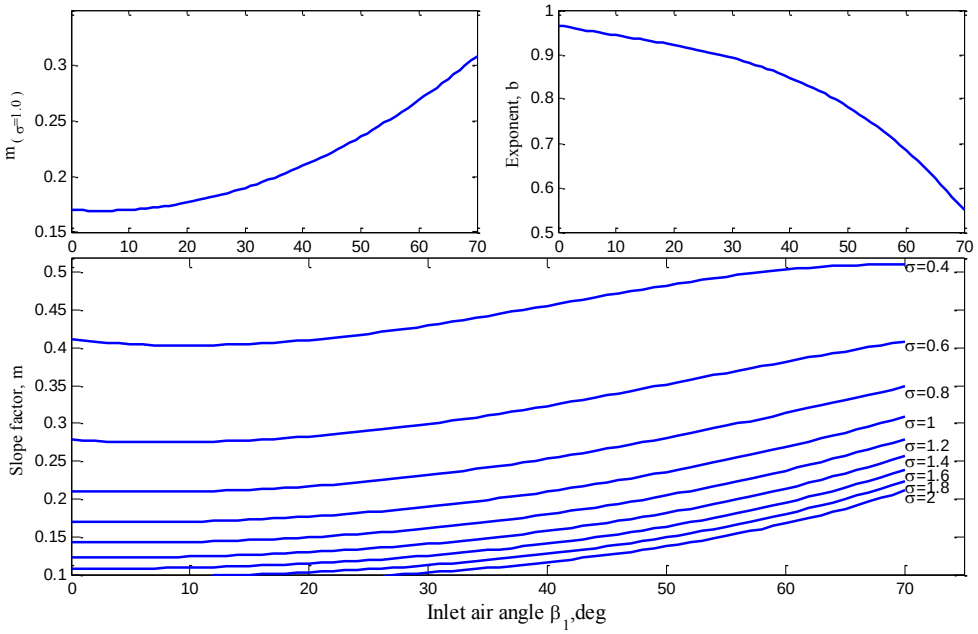

Figure A.17: slope factor for a cascade solidity of 1 (top left), Exponent b for deviation angle for 10 % thick NACA 65-A10 (top right), deviation angle slope factor(bottom).

With the reference minimum loss incidence angle and reference deviation angle established, the variation of deviation angle with incidence angle for small perturbations from design conditions can be estimated as

$$\delta = \delta_{ref} + (i - i_{ref})\left(\frac{d\delta}{di}\right)_{ref}$$

where $(d\delta/di)_{ref}$ represents the slope of the deviation angle variation at the reference incidence angle. An empirical determination of the slope variation of deviation angle was

obtained as:

$$\left(\frac{d\delta}{di}\right)_{ref} = \left[1 + 3.09\left(\frac{\beta_1}{70}\right)^2 \sigma^{1.4}\right] e^{-3.2\sigma}$$

Fig. A.18 charts the deviation angle slope $(d\delta/di)_{ref}$. Thus, it is possible to predict the deviation angle at incidence angle other than the reference location at design condition for off-design points for NACA 65-A10 blade. For instance given a inlet flow angle β_1, the deviation angle can be estimated. This approximation defines the outflow angle β_2, completing the off-design velocity triangle.

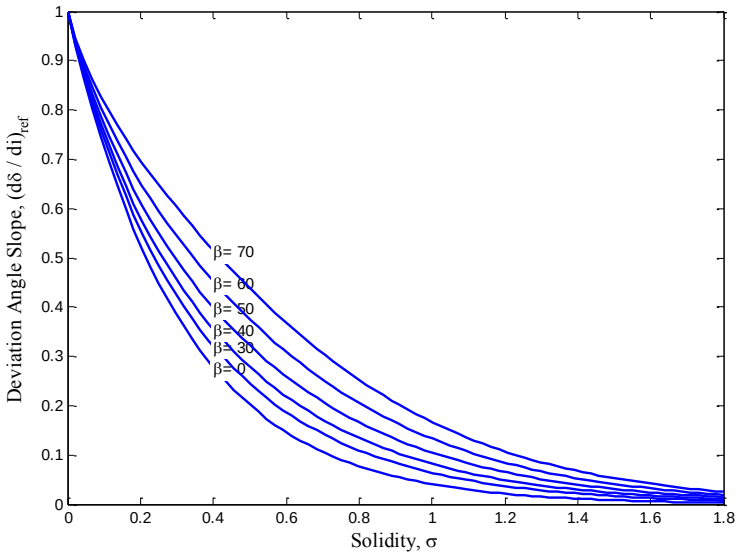

Figure A.18: Deviation angle slope $(d\delta/di)_{ref}$ at reference incidence angle from low-speed data for NACA 65-A10 blade.

In 1953, Lieblein proposed an empirical dimensionless number, so called the diffusion factor, D. This variable relates the peak velocity on the suction surface of the blade to the velocity at the trailing edge. Values in excess of 0.6 surface as an indicator of the possibility of boundary layer separation from the blades. Convenient evaluation of D involves quantities measured during cascade testing. The Lieblein's diffusion factor D is defined as:

$$D = \frac{W_{max} - W_{ii}}{W_i} = 1 - \frac{w_{ii}}{w_i} + \frac{w_{\theta i} - w_{\theta ii}}{2\sigma w_i}$$

A simplified method on how to establish the diffusion factor relies on the equivalent diffusion

ratio:

$$D_{eq} = \frac{c_{max}}{c_2}$$
$$= \frac{cos(\beta_2)}{\cos(\beta_1)}\left[1.12 + 0.61\frac{cos^2(\beta_1)}{\sigma}(tan(\beta_2) - tan(\beta_1))\right]$$

The equivalent diffusion ratio D_{eq} is also dependable indicator of the approach to separation for a variety of blade shapes. Because total pressure loss is produced by separation, the importance of Leiblein's D parameter is its correlation with measured cascade loss coefficients. For a specified D_{eq}, Aungier suggested the following curve fit for momentum thickness to chord ratio

$$\frac{\theta}{c} = 0.004\left[1 + 3.1(D_{eq} - 1)^2 + 0.4(D_{eq} - 1)^8 + k(i - i_{ref})^{1.43}\right]$$

where a=0.0117 for NACA 65-series blades. The corresponding total-pressure loss coefficent due to profile loss is given by

$$\bar{\omega_p} = 2\left(\frac{\theta}{c}\right)\frac{\sigma}{cos(\beta_2)}\left(\frac{cos(\beta_1)}{cos(\beta_2)}\right)^2$$

Profile losses arises from viscous effect such as skin friction and flow separation. Similar to flow over an airfoil the drag depends on angle of attack, α. At higher α, flow separation over the top surface begins to appear, and the drag due to separation increases. The total stagnation loss coefficent is the sum of all the loss coefficients. Since we only determined the profile loss, then $\bar{\omega} = \bar{\omega_p}$. Following the calculation of the loss coefficient $\bar{\omega_p}$ the sub-calculations are redone to converge onto the real rotor loss coefficient. Stator properties are determined using the same sub-calculations methodology. However, flow angles and total pressure are now in the absolute reference frame

$$\Phi = \alpha_1^* - \alpha_2^* \qquad \xi = \frac{1}{2}(\alpha_1^* + \alpha_2^*) \qquad \sigma = \text{solidity of stator} \tag{A.22}$$

that is, every relative flow angle is replaced by the absolute flow angle in the correlations, i.e. $\beta_1 \rightarrow \alpha_1$, $\beta_2 \rightarrow \alpha_2$. As shown in Fig. A.7, the total pressure loss-coefficient for the stator $\bar{\omega}_{stator}$ is computed by recursion. Since the stator blades were already designed during a previous investigation, to simplify and ease calculations it was assumed no total pressure loss occurred across the stators, i.e. $P_0[3] = P_0[4]$. Thus, the static pressure at the exit is

$$P_{static}[4] = P_0[4]\Big(1 + \frac{\gamma - 1}{2} M[4]^2\Big)^{\frac{\gamma}{\gamma - 1}} \tag{A.23}$$

A.4 Radial Equilibrium and Blade Stacking

So far we restricted our attention to the meanline. To design a efficient fan, the radial variations from the rotor hub to tip must be calculated. Thus, it is necessary to take into account radial varation in blade speed, axial velocity (c_z), and tangential velocity (c_θ). The design of the rotor blades is obtained from the energy equation, with the assumption that the radial gradient of the entropy and the stagnation enthaply are zero

$$\frac{d}{dr}(c_z^2) = \frac{-1}{r^2}\frac{d}{dr}(rc_\theta)^2$$

The above expression couples the axial velocity component and the angular momentum rc_θ. The velocity distributions must satisfy this relationship at the entrance and exit of the rotor. In order to provide uniform flow at the exit of the fan, it is necessary to evenly distribute the work input along the radial length of a rotor. Thus, to keep the work constant, the product $r\Delta c_\theta$ must be constant with radius. The product $r\Delta c_\theta(r)$ distribution is regarded as a design choice that will influence the blade twist. One configuration that satisfy this requirement is the "constant reaction" distribution

$$rc_\theta = ar^2 + b \tag{A.24}$$

The angular momentum distribution will be different upstream and downstream of the rotor. Writing the "constant reaction" angular momentum distribution before and after the rotor as

$$c_{1\theta} = a\left(\frac{r}{r_m}\right) - b\left(\frac{r}{r_m}\right) \qquad c_{2\theta} = a\left(\frac{r}{r_m}\right) + b\left(\frac{r}{r_m}\right) \tag{A.25}$$

where $r_m, a,\ b$ are the mean radius and constants, respectively. The change in stagnation enthaply through the rotor is

$$\Delta h_0 = \bar{\omega}^*_{rotor}\Omega r(c_{2\theta} - c_{1\theta}) = \bar{\omega}^*_{rotor}\Omega r 2b\frac{r_m}{r} = \bar{\omega}^*_{rotor}2b\Omega r_m = \bar{\omega}^*_{rotor}2bU_m \tag{A.26}$$

which gives a constant stagnation enthaply when the we keep the work the same at all radii, and $\bar{\omega}^*_{rotor} = 1 - \bar{\omega}_{rotor}$. This being the case, rearrangement gives the constant b

$$b = \frac{\Delta h_0}{2U_m\bar{\omega}^*_{rotor}} = \frac{c_p\Delta T_{0,rotor}}{2U_m\bar{\omega}^*_{rotor}} \tag{A.27}$$

The second constant a, is determined from the degree of reaction as

$$a = \bar{\omega}^*_{rotor}U_m(1 - R_m) \tag{A.28}$$

where R_m is the degree of reaction at the meanline.

$$R_m = 1 - \frac{c_u^2}{2c_p\Delta T_{0,rotor}} \tag{A.29}$$

The degree of reaction is defined as the change in enthalpy in the rotor divided by the change in stagnation enthalpy in the stage. Ideally the best efficiency would be obtained with R about 0.5. A degree of reaction of 0.5 means half of the enthaply rise takes place in the stator and half in the rotor. The "constant reaction" distribution aims to minimize substantial departure from $R_m = 0.5$ at root and tip diameter, see Fig. A.20. With constant c_z along the span and local blade speed Ωr, we can determine the complete velocity triangles

as shown in Fig. A.19. Also shown are blade cross sections as they might appear at the various radii.

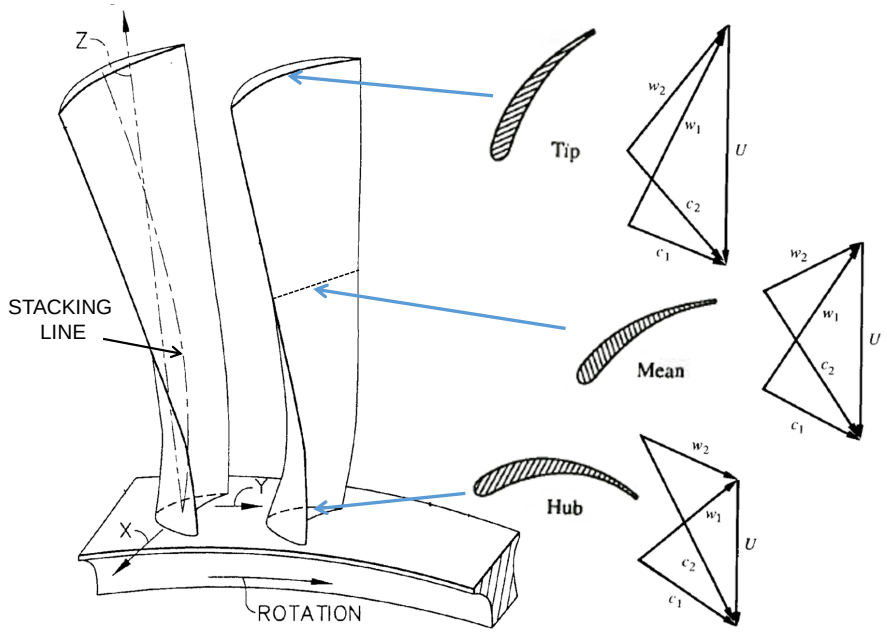

Figure A.19: Free Vortex Vector Diagram and blade profiles at hub meanline and tip when c_z is independent of radius. Figure adapted from pg. 334 of Mechanics and Thermodynamics of Propulsion.

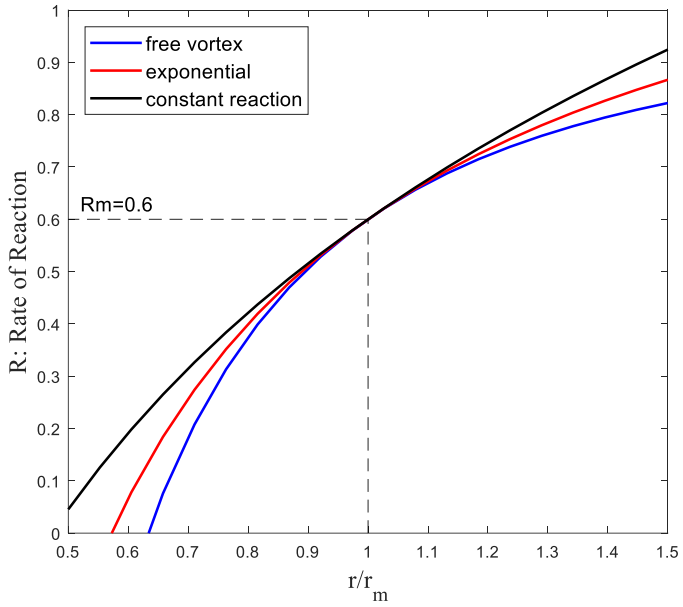

Figure A.20: Radial variation of rate of reaction for various work distribution.

Airfoil sections were determined at various radial positions. Thickness (t/c), and chord

(c) or solidity (σ) profiles were scaled by a multiplier to satisfy manufacturing constraints. Properties such as airfoil metal angles (β), and camber (Φ), were obtained from radial equilibrium. Sections geometry were based on NACA 65-airfoil series and were corrected for thickness and camber angle numerically. The camber angle was determined from the slope of the camberline at the leading and trailing edge. In addition thickness was added to the trailing edge. These sections are then stacked at the midchord to form the rotor blade as illustrated in Fig. A.21.

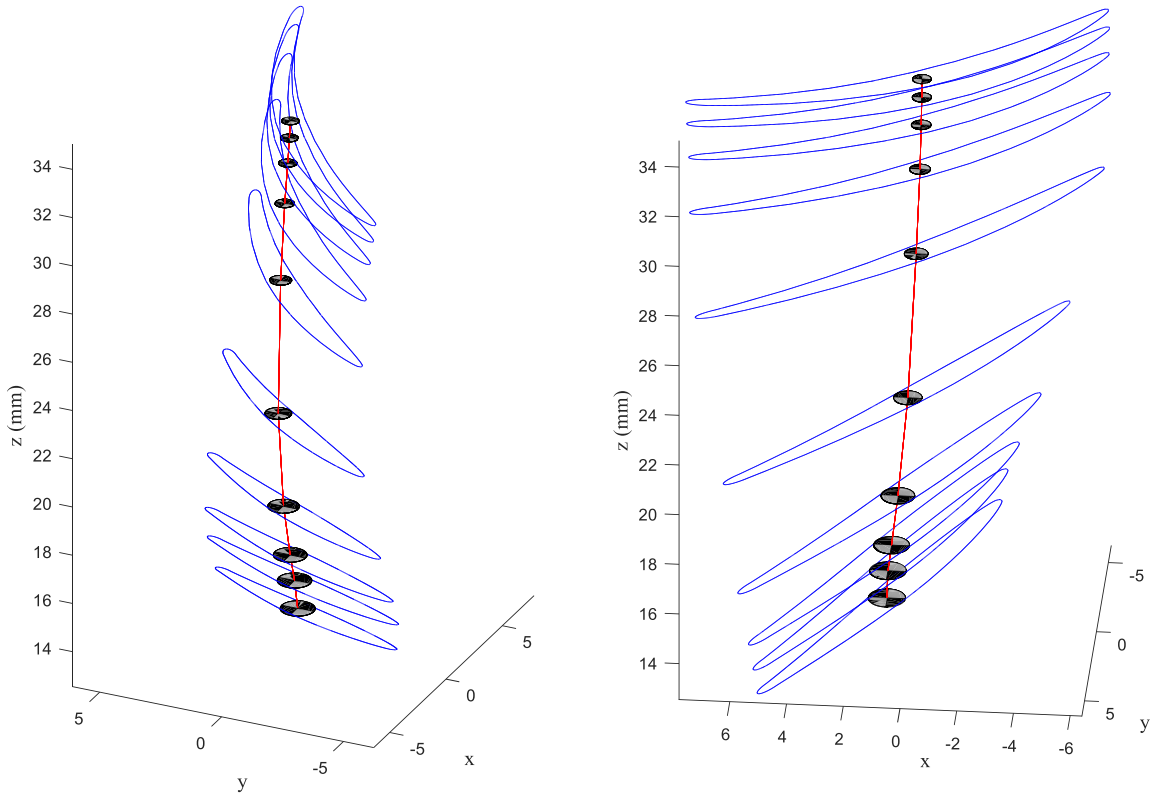

Figure A.21: Stacked Rotor blade.

A Solidworks CAD model of the rotor was produced using imported MATLAB generated blade-section coordinates files. The model integrates a lockring for easy removal of the rotor, provided a Park Tool FR-5.2 cassette lockring tool. The blade tip was cut to the specified diameter (i.e. tip clearance) using Solidworks. The rotor core features a hub and spoke wheel design to reduce the weight of this lightly loaded section. In addition, thick sections are more difficult to cast and more prone to solidification problems. That is, the

weight can more comfortably be supported by the shell as metal is poured in a hub and spoke wheel design. Many internal passages, through holes, or shape complexity are almost not a factor in the cost of a part. Hub to blade transitions were filleted to avoid sharp edges that can lead to tears and crack as the part solidify. Images of the rotor CAD model are shown in Fig. A.22.

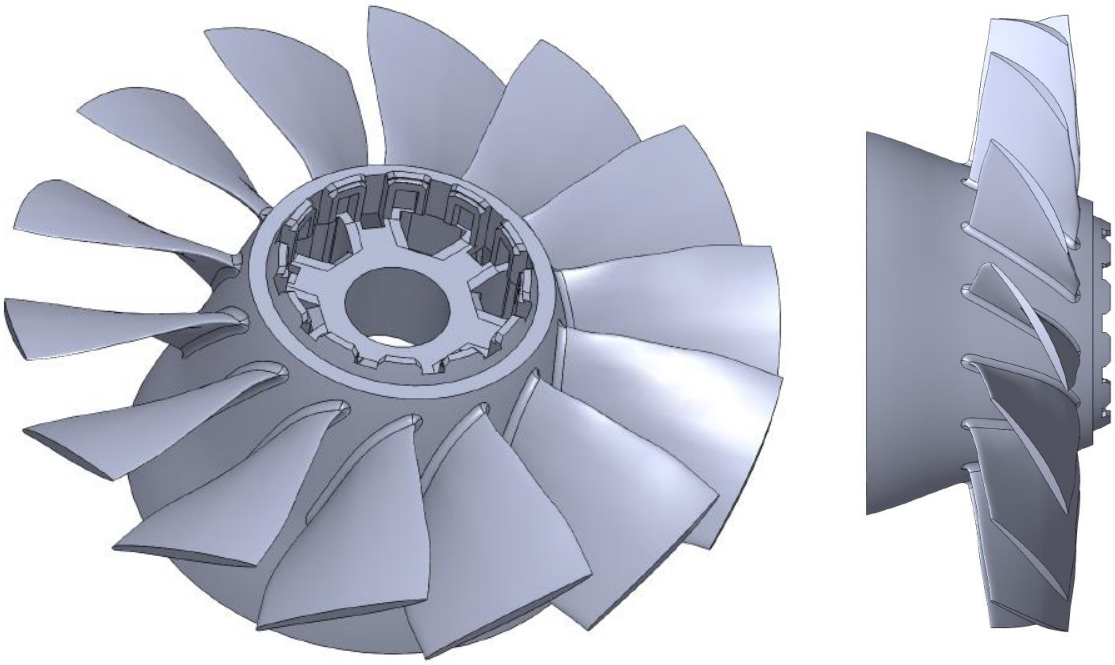

Figure A.22: Solidworks CAD model of the rotor.

A.5 Computation Fluid Dynamics

Computational fluid dynamics was used to numerically solve for the flow field inside the ducted fan. These computations substantiate efficient flow turning free of separation or stall,and proper blade stacking. The problem to be considered is shown schematically in Fig. A.23. The rotor consist of 14 blades. A steady state solution for this configuration using only one rotor blade is desired. There is no need to model the whole solution domain since it is expected that the flow are identical across boundaries cutting through the flow passage. Thus, circumferential periodicity is used to reduce the computational domain to

1/14 of its full size, greatly reducing the number of cells required for the simulation. No stators are involved, since the periodic angles for the rotor and stator are different, a mixing plane at the interface would complicate simulations.

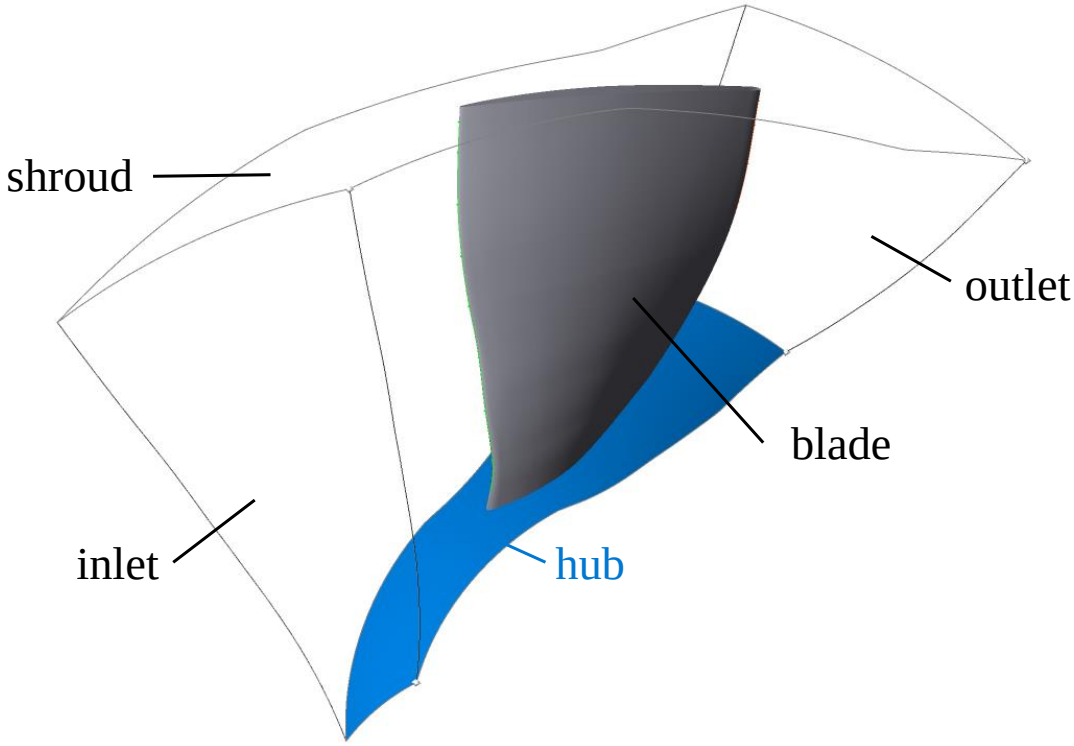

Figure A.23: Problem specifications.

The grid is set up with periodic boundaries on either side of the rotor blades. The no-slip boundary condition is used on the blades, hub, and shroud. At the inlet boundary, all quantities must be prescribed. Ambient air is drawn into the fan (at 101325 Pa and 273 K)and is compressed (at P_s =106480 Pa and 306 K). The hub and blade of the rotor are assumed to be rotating at 57,000 rpm.

For problems where all the moving parts (fan blades, hub and shaft surfaces, etc.) are rotating at a prescribed angular velocity, and the stationary walls (e.g., shrouds, duct walls) are surfaces of revolution with respect to the axis of rotation, the entire domain is best solved using a rotating reference frame for the fluid. In such flows the coordinate system is moving with the rotating equipment, and thus experiences a constant acceleration in the

radial direction. The conservation equations are

$$\nabla \cdot (\rho u) = 0$$

$$\rho\left(\frac{D\vec{u}}{Dt} + 2\vec{\Omega} \times \vec{u} + \vec{\Omega} \times (\vec{\Omega} \times \vec{x})\right) = -\nabla p + \nabla \cdot \bar{\bar{T}} \tag{A.30}$$

where the reference frame rotates with angular velocity $\vec{\Omega}$, and the position $\vec{x}$ and velocity $\vec{u}$ are measured in the rotating reference frame. The 2nd and third term in the parenthesis represents the Coriolis and centripetal acceleration, respectively. $\bar{\bar{T}}$ is the viscous stress tensor. The viscosity is modeled by a two equation SST k-ω model. The shear stress transport (SST) formulation combines the best of two worlds. The use of a k-ω formulation in the inner parts of the boundary layer makes the model directly usable all the way down to the wall. In the free-stream, the model switches to a k-ϵ behavior enabling more realistic predictions where mean pressure gradients are small.

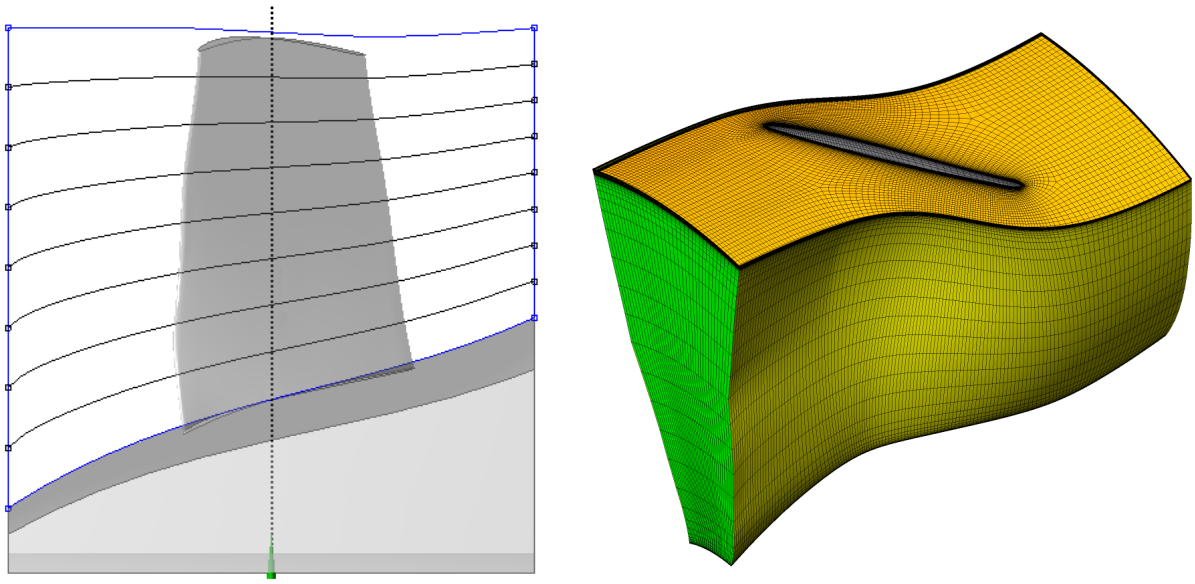

Figure A.24: Flow path coutours (left), meshed geometry (right).

The software ANSYS FLUENT was used to perform the simulations. This commercial software replaces the individual terms in the governing conservation equations with discretized algebraic forms, which in turn are solve to obtain numbers for the flow-field vari-

ables at discrete points in space. CAD geometry was imported to ANSYS Design Modeler and flow path contours are created by defining the hub and shroud using FlowPath. Flow path contours are depicted on the left in Fig. A.24. Structured mesh between the blade passage was generated using TurboGrid- a meshing tool that is specialized for CFD analyses of turbomachinery. Fig. A.24 depict the grid containing 950,000 nodes used in computation. Convergence was obtained when the residual for each equation falls below $1x10^{-3}$. Lastly, figures such as A.25 were generated with CFD-Post, a post-processor that is included in ANSYS Workbench.

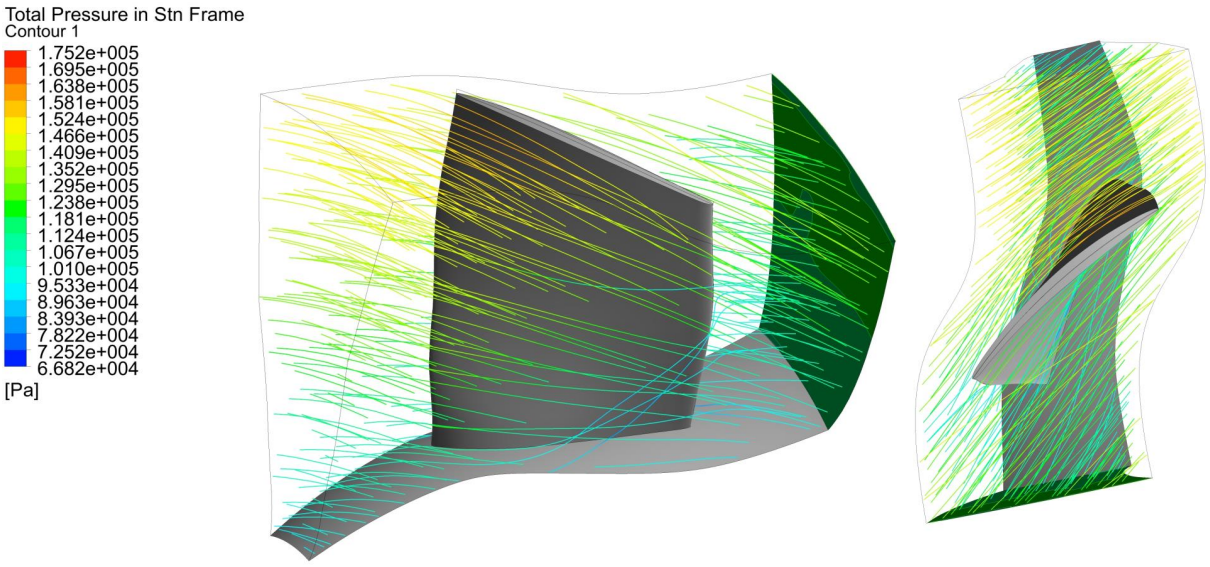

Figure A.25: Fluent CFD simulation of the rotor blade row.

Appendix B

Brushless RPM Sensor

B.1 Brushless motors

Radio control aircraft are often driven by brushless motors due to their high power to weight ratio, high speed, and efficiency. When paired with a high-discharge Li-Po (lithium polymer), fans can achieve high tip speeds. A traditional brushless motor is made up of two basic parts: a ring of permanent magnets, and an electromagnet. The permanent magnets rotate together on the motor shaft, while the windings of the electromagnets (coils) are fixed and surround the shaft, see Fig. B.1. The coils are connected together in specific pairs. The part that rotates and has the magnets mounted in a radial pattern is called the *rotor*. Meanwhile stationary components are called *stators*. The motor controller (commonly known as the electronic speed controller or ESC) is the device that controls the motor by activating and deactivating specific sections of electromagnets in the motor at very specific times to cause the rotor of the motor to spin due to the magnetic force. These electomagnets are connected into three main sections which is why all brushless motors have 3 wires coming out of them. These motor configuration is known as a 3-phase brushless motor.

Motors are described by numerous parameters, some important metrics are:

Kv rating. Kv rating is measured by the number of revolutions per minute (RPM) that a motor turns when one volt ($1V$) is applied with no load attached to that motor.

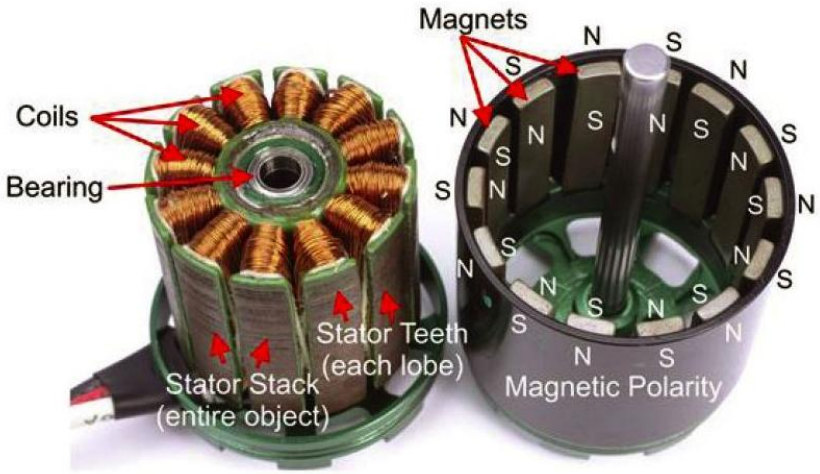

Figure B.1: Components of a brushless motor from DroneTrest "Brushless motors - how they work and what the numbers mean".

The Kv rating of a brushless motor is the ratio of the motor's unloaded rpm to the peak voltage on the wires connected to the coils. Knowing the Kv rating of a motor will help you determine how fast that motor will rotate when a given voltage is applied to it.

$$RPM = Kv \times V \tag{B.1}$$

where V is the voltage. For example, a 1355 Kv motor powered by an 44.4 V ($12S$) battery would spin at 60,162 RPM (1355 x 44.4) with no load. Torque is inversely proportional to the Kv rating. A low Kv motor has more winds of thinner wire-it will carry more volts at fewer amps, produce higher torque, and swing a bigger prop. Alternatively, a high Kv motor has fewer winds of thicker wire that carry more amps at fewer volts and spin a smaller prop at high revolutions.

Type of winding. There are two common electrical winding configurations: Y (wye) and D (delta). The delta configuration connects three windings to each other (series circuits) in a triangle-like circuit. A motor with windings in delta configuration gives low torque at low speed, but can give higher top speed. The Wye (Y-shaped) configuration, sometimes called a star winding, connects all of the windings to a central point (parallel circuits) and

power is applied to the remaining end of each winding. This configuration gives high torque at low speed, but not as high top speed. The type of winding correlates with the Kv rating, with higher rating for the D winding. For instance, our experiments requires high rpm, thus a D-winding is preferred.

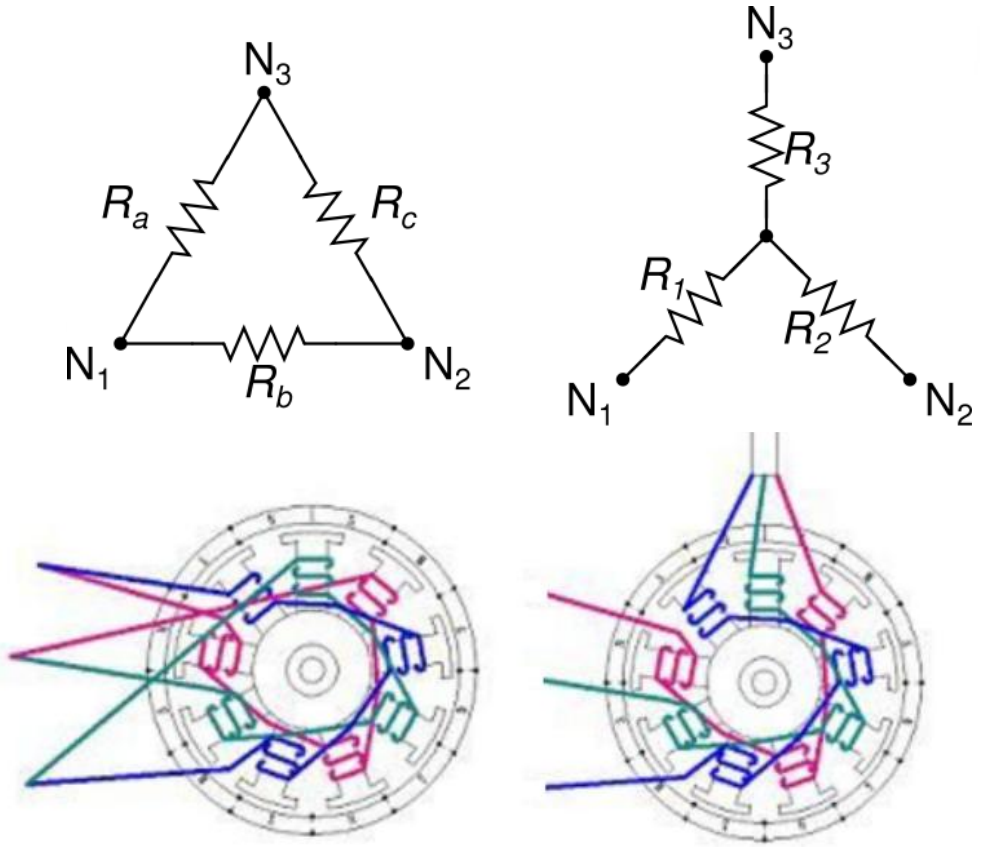

Figure B.2: Delta (left) and Wye motor configuration.

The Neu motor info can be decoded as follows using a **1530-1.5D** as a example.

15= 1.5 inch stator diameter.

30= 3.0 inch rotor length (longer means more torque).

1.5= 1.5 turn wire around each stator tooth (lower number gives higher Kv).

D= Delta wiring (high speed).

B.2 RPM sensing

A schematic of a 3 phase brushless motor is shown in Fig B.3. Let's imagine pole pair A is first fed a DC pulse which magnetizes pole A1 as a south pole and A2 as a north pole drawing the magnet into its initial position. As the magnet passes the first magnetized pole pair (A1/A2), the current to pole A is switched off and the next pole pair B is fed with a similar DC pulse causing pole B1 to be magnetized as a south pole and B2 to be a north pole. The magnet will then rotate clockwise to align itself with pole B. By pulsing the stator pole pairs in sequence the magnet will continue to rotate clockwise to keep itself aligned with the energized pole pair. This process of the current alternating direction is called commutation. The current pulses are triggered in a closed loop system where a Hall Effect sensor measures the motor position. Thus, the frequency of these pulses is equal to the rotational speed of the motor. Poly-phase stepped waveforms to the 3 wires connecting the brushless motor are shown to the right of Fig. B.3. Since the frequency of the current pulses is proportional to motor speed, a brushless RPM sensor was developed by sensing the current waveform from one wire.

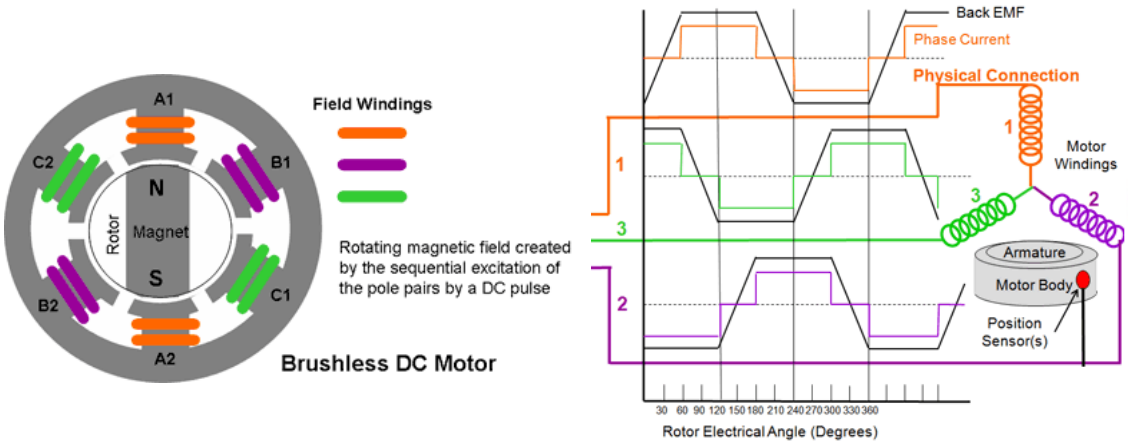

Figure B.3: Brushless DC motor commutation from Electropedia.

Measurement of the RPM relied on clamping a current sensor to one of the three wires leading from the ESC to the motor as depicted in Fig. B.4. Our custom made

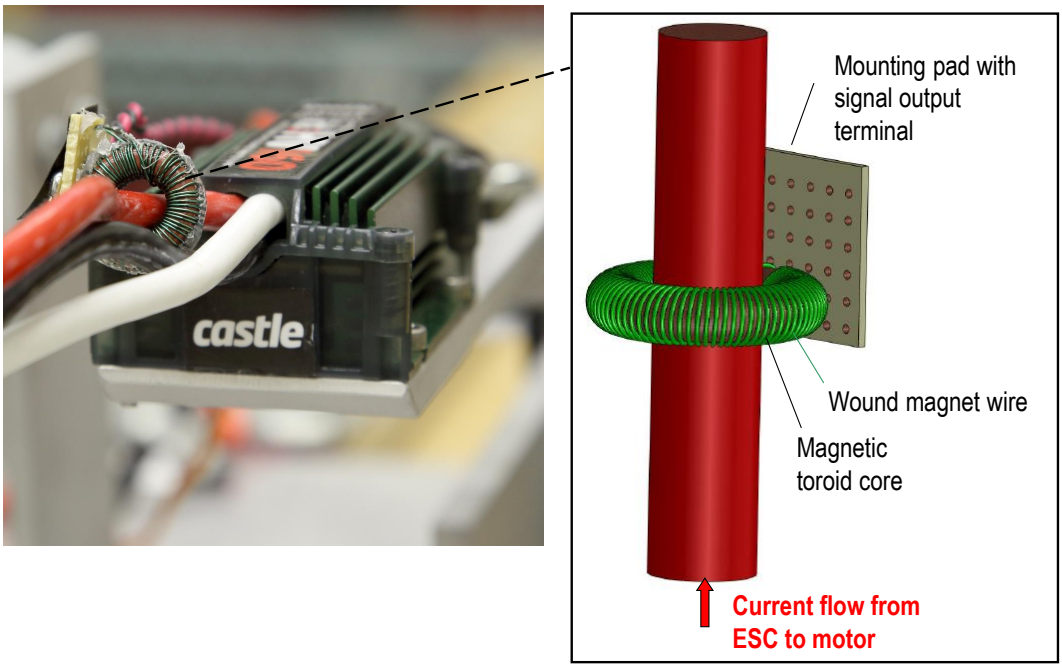

Figure B.4: Toroid current transformer sensor.

current transformer consists of a magnetic toroid core that has been wound with magnetic wire. When a fluctuating current is present due to running the motor, electromagnetic induction occurs inducing a signal in the sensor wire. This allows properties of the electric current in the conductor to be measured, without having to make physical contact with it. Previous attempts without using a noninvasive sensor caused the wire to heat and smoke. The current-carrying conductor is generally referred to as the primary and the core winding is called the secondary. The size of the induced voltage resulting from the induced current in the secondary coil depends on the number of turns in the secondary coil. The relationship between the current and the number of turns in each coil is given by the amp-turn equation:

$$\frac{\text{Current in Secondary Coil}}{\text{Current in Primary Coil}} = \frac{\text{Turn on Primary Coil}}{\text{Turn on Secondary Coil}} \tag{B.2}$$

By increasing the number of secondary windings, the secondary current can be made much smaller than the current in the primary circuit being measured. The ratio between the primary and secondary can be quite large. For example, assume that the current rating of

the primary winding is 160 A. The secondary winding has the rating of 1.6 A. Then the number of winding of the secondary coil is 100. Practically, it is impossible to wrap the magnetic wire around the toroid core above 40 turns and have the clearance required to slide the ESC cable through the center. However, DAQ current limitations are typically around 40.0 mA.

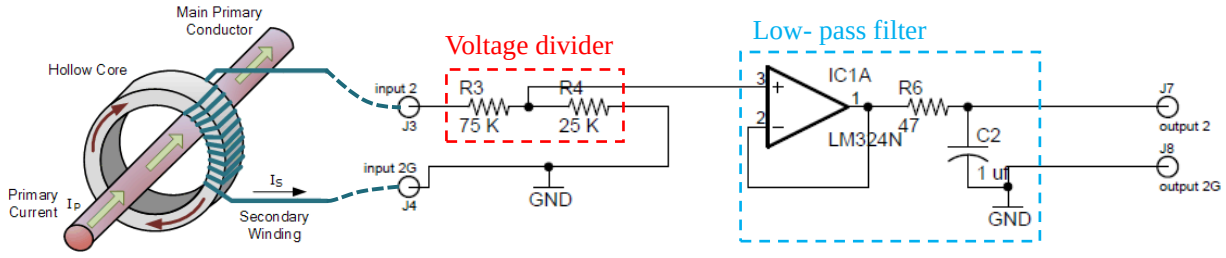

Figure B.5: Circuit diagram of RPM sensor.

Figure B.5 illustrates the circuit used make the high current data safe for DAQ boards. From the current transformer, the raw signal voltage was reduced to levels tolerated by the data acquisition systems. A buffer was then used to prevent the low-pass filter circuit from loading the voltage divider circuit unacceptability and interfere with the frequency response of the filter. Implementation of the low-pass filter attenuates the fast switching pulse-width modulation (PWM) component of the signal. PWM is a technique used to relay data in the form of a varying pulse width, and is used to control power to the motor. The electronic circuit outputs a periodic waveform at the commutation frequency. A MATLAB script was developed spectral analyze of the data. Fig. B.6 shows the steps in the processing of the rpm sensor signal. The highest peak of the spectrum of this signal is at the commutation frequency. Conversion from the commutation frequency fc (Hz) to RPM is given by the formula $RPM = fc\,60\,2/Np$, where Np is the number of magnetic poles in the motor. The Neu 1530 has four poles, for which RPM=$30fc$. The RPM inferred from the blade passing frequency measured by the microphones was within 0.5% of the RPM measured using the speed controller (ESC) data.

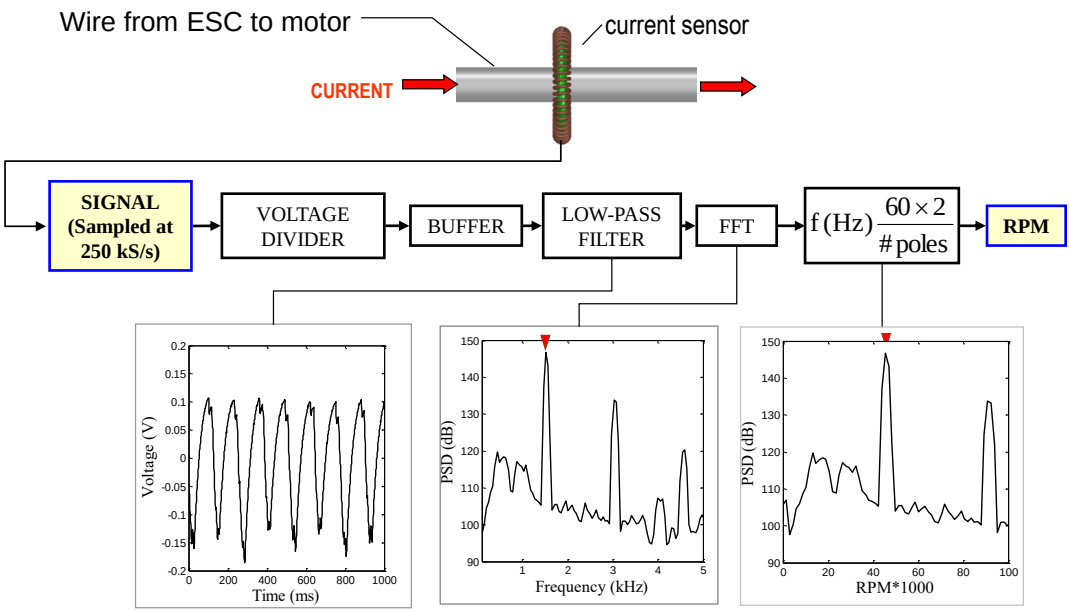

Figure B.6: RPM sensor processing Flowchart.

B.3 Processing of RPM data

quickgtf.m is used to determine the RPM of the rotor. The inputs to the code varies:

```
quickgtf

quickgtf('.m12')

quickgtf('DFAN0103','.m12')
```

`quickgtf` plot the acoustic spectra for the default microphone number (channel 8) for the newest experimental test run, along with the spectra for the rpm sensor (channel 20).

`quickgtf('.m12')` specifies the microphone number (channel 12) used in plotting of the acoustic spectra for the newest experimental test run, along with the spectra for the rpm sensor (channel 20).

`quickgtf('DFAN0103','.m12')` specifies the experimental number (DFAN0103) and microphone number (channel 12) used in the plotting of the acoustic spectra. The spectra for the

rpm sensor is plotted below the acoustic spectra.

The algorithm works as follows:

1. Using the RPM sensor data from channel 20, determine the highest peak from the FFT and corresponding frequency

2. Convert the frequency reading into a RPM value through the equation

$$RPM = Frequeny \times \frac{60\ 2}{N_p} \tag{B.3}$$

   where N_p is the number of magnetic pole in the motor and the two factor accounts for the winding pair. The Neu 1530 has four poles, for which $RPM = Frequency \times 30$.

3. Using the RPM value convert the number to the respective blade passage frequency that should be seen by the microphone. Translation from RPM sensor and microphone frequency is as follows:

$$BPF = \frac{RPM\ \times \#\,of Blades}{60} \tag{B.4}$$

   where the number of blades is 14 for the ducted fan experiments.

4. Using the microphone signal, look for the peak that relate to that frequency within a predefined tolerance.

5. Plot a line for the blade passage frequency of the fan as illustrated in figure B.7. Print out RPM value according to the equation:

$$RPM = \frac{BPF \times 60}{\#\,of Blades} \tag{B.5}$$

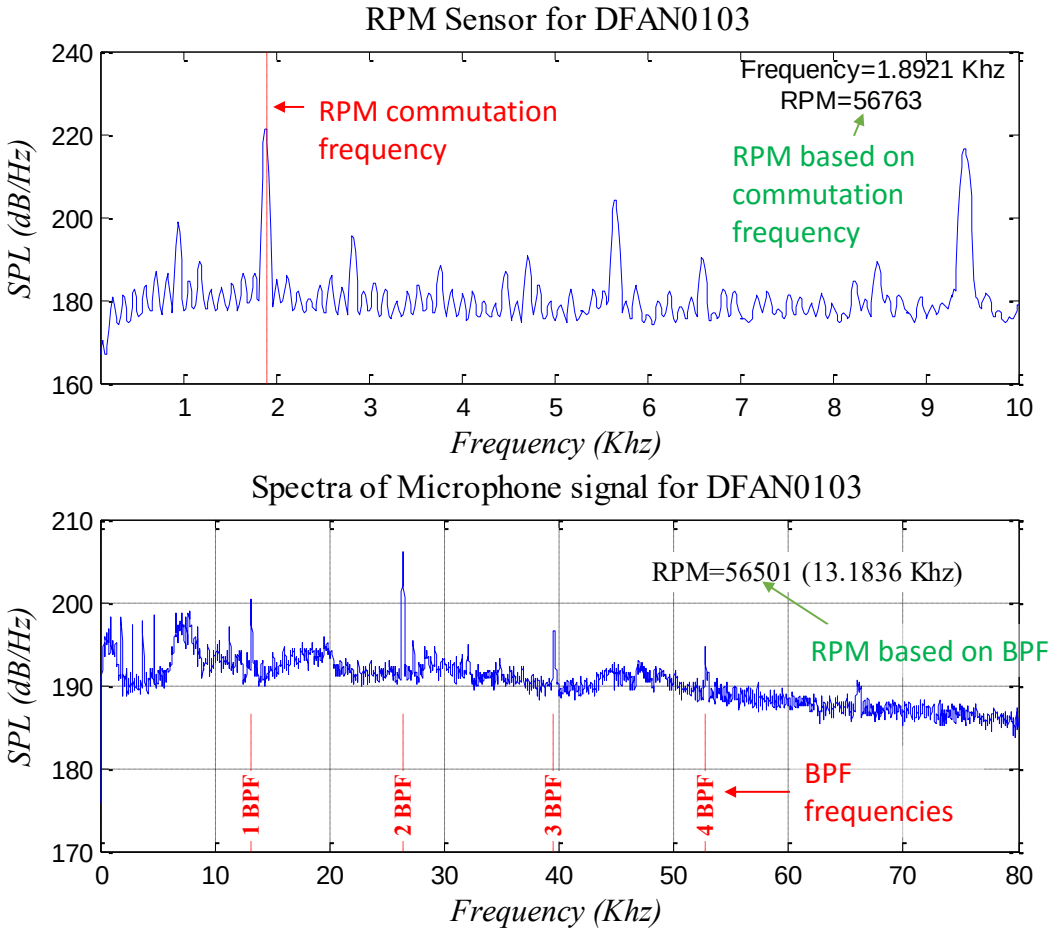

Figure B.7: RPM and microphone spectra plots from quickgtf MATLAB code.